Forecasting Indoor Environment using Ensemble-based Data Assimilation Algorithms

Cheng-Chun Lin

A Thesis

In the Department

of

Building, Civil and Environmental Engineering

Presented in Partial Fulfillment of the Requirements

for the Degree of Doctor of Philosophy at

Concordia University

Montreal, Quebec, Canada

December 2014

CONCORDIA UNIVERSITY
SCHOOL OF GRADUATE STUDIES

This is to certify that the thesis prepared

By: Cheng-Chun Lin

Entitled: Forecasting Indoor Environment using Ensemble-based Data Assimilation Algorithms

and submitted in partial fulfillment of the requirements for the degree of

PhD of Building Engineering

complies with the regulations of the University and meets the accepted standards with respect to originality and quality.

Signed by the final examining committee:

Dr. Fariborz Haghighat Chair

Dr. David Torvi External Examiner

Dr. Hoi Dick Ng External to Program

Dr. Samuel Li Examiner

Dr. Liangzhu (Leon) Wang Examiner

Dr. Liangzhu (Leon) Wang Thesis Supervisor

Approved by

Chair of Department or Graduate Program Director

Dean of Faculty

ABSTRACT

Forecasting Indoor Environment using Ensemble-based Data Assimilation Algorithms

Cheng-Chun, Lin, Ph.D.

Concordia University, 2014

Forecasting simulations of building environment have attracted growing interests since more and more applications have been explored. Occupant's thermal comfort, safety and energy efficiency are reported to directly benefit from accurate predicted building physical conditions. Among all available research regarding forecasting indoor environment, there are substantially fewer studies relating to occupant safety and emergency forecasting and response than that of comfort and energy savings. This may due to the nature that the forecasting simulations associated with life safety concerns demand higher accuracy. Although the tasks of forecasting potential threats in the indoor environment are especially challenging, the benefits can be significant. For example, toxic contaminants such as carbon monoxide from fire smoke can be monitored and removed before the concentration reaches a harmful level. The sudden release of hazardous gases or the smoke generated from an accidental fire can also be detected and analyzed. Then, based on the results of forecasting simulations, the building control system can provide an efficient evacuation plan for all occupants in the building. However, by using traditional simulation tools that utilize one set of initial inputs to forecast future physical states, the predicted physical conditions may depart from reality as the simulation progresses over time.

In this thesis, forecasting simulations of building safety management are improved by applying the theory of data assimilation where the simulation results are aided by the sensor measurements. Instead of studying methods that require high computational resources, this research focuses on affordable approaches, ensemble-based algorithms, to forecast indoor environment to solve various safety problems including forecasting indoor contaminant and smoke transport. The resulting models are able to provide predictions with noticeable accuracy by only using affordable computer resources such as a regular PC. Finally, a scaled compartment fire experiment is conducted to verify the real-time predictability of the model. The results indicate that the proposed method is able to forecast real-time fire smoke transport with significant lead time. Overall, the method of Ensemble Kalman Filter (EnKF) is efficient to apply to forecasting indoor contaminant and smoke transport problems. In the end of this thesis, suggestions are summarized to help those who would like to apply EnKF to solve other building simulation problems.

For the most important persons of my life,

my wife Feng-Hua and our children Yahsi and Janhsi.

Acknowledgements

First, I would like to express my great thanks to my supervisor, Dr. Liangzhu (Leon) Wang, for his patience and guidance. He is enthusiastic and dedicated in science research and even willing to spend his weekend to help me with programming and correcting my writings.

Besides, I would like to thank the rest of my thesis committee: Dr. Fariborz Haghighat, Dr. Samuel Li, Dr. Hoi Dick Ng and Dr. David Torvi. Their comments are a treasure to me not only for this thesis but also for my future research.

It would also like to thank Dr. Nils van Velzen for helping me program data assimilation models. Reading his PhD thesis is a pleasant and inspires me for building my own models.

I would also like to show my gratitude to my lab mates, Jeremy (Guanchao) Zhao and Dr. Wael Saleh, who are very knowledgeable in fire experiments and PIV. They helped me set up whole experiment from scratch and performing the experiments altogether. In addition, I would like to thank Dr. Hoi Dick Ng for providing experiment equipment and a large lab space for us.

I would like to thank my mother's understanding while I gave up my job in Taiwan in order to catch my dream. Without her financial support, this thesis would not have been possible.

Finally, I would like to thank my wife Feng-Hua and our children Yahsi and Janhsi. Their encouragement and support mean a lot to me. The honor is all yours!

Table of Contents

Chapter 1. Introduction ……..…… 1

1.1 General statement of the problem …….……..…… 1

1.2 Forecasting indoor environment using data assimilation …….. 2

1.2.1 Development of data assimilation ….…….…….…….……. 3

1.2.2 Categories of data assimilation algorithms ….…….…….……..... 6

1.3 General research objectives and thesis outline ……..… 9

References …… 11

Chapter 2. Literature Reviews …….. 13

2.1 Forecasting indoor environment……. 13

2.2 Forecasting indoor environment using data assimilation ……. 15

2.3 Ensemble based data assimilation algorithms …….…..……. 17

2.3.1 Ensemble square root filter (EnSRF) ….…….…….…….…… 18

2.3.2 Local ensemble transform Kalman filter (LETKF) ….…….…….….. 18

2.3.3 Deterministic ensemble Kalman filter (DEnKF) ….…….…….…….. 19

2.3.4 Ensemble Kalman filter (EnKF) ….…….…….…….…….. 20

References …… 20

Chapter 3. Methodologies …….…. 23

3.1 Research methodologies ….…….…….…….…….……... 24

3.1.1 Introduction of zone model ….…….…….…….…….…….. 26

3.1.2 Ensemble Kalman filter ….…….…….…….…….……... 41

References ……..…….. 44

Chapter 4. Forecasting Simulations of Indoor Environment using Data Assimilation via an Ensemble Kalman Filter ….…….…….…….…….…….. 45

4.1 Introduction ……..…… 46

4.1.1 Forecasting contaminant transport ….……..…… 46

4.1.2 Data assimilation ….……..……..……..……..…… 47

4.2 Methodology ……..……. 49

4.2.1 Multi-zone manufactured house ….……..……..……. 49

4.2.2 Tracer gas concentration model ….……..……..……. 51

4.2.3 Stochastic model of tracer gas concentration ….……..……. 52

4.2.4 Combining numerical prediction and measurement by EnKF ….……..…… 52

4.3 Results and discussions …….. 55

4.3.1 CONTAM airflow rate simulations ….……..……..…… 55

4.3.2 Tracer gas forecasting with and without EnKF ….……..…….. 56

4.3.3 Discussion of key EnKF parameters ….……..……. 57

4.4 Conclusions ….……..……..……..……..……. 63

References …… 64

Chapter 5. Forecasting Smoke Transport during Compartment Fires using Data Assimilation Model ……. 67

5.1 Introduction ……..……. 67

5.2 Methodology ……..…… 71

5.3 Forecasting smoke transport using ensemble Kalman filter……..... 75

5.3.1 Case A: Estimation of Heat Release Rate and Mechanical Ventilation Rate …. 76

5.3.2 Case B: Prediction of smoke layer height ….……..……..…. 80

5.3.3 Case C: Forecasting smoke spread in a multi-room compartment fire ….…… 83

5.4 Conclusions and future work……..…… 91

References …… 92

Chapter 6. Scaled Compartment Fire Experiment …..……..……..……. 96

6.1 Background information…….....……... 96

6.2 Experiment setups…….....……..… 97

6.3 Smoke temperature and smoke layer height…….....……. 99

6.4 Results and discussions…….....……..…… 101

6.4.1 Case A – change of HRR …..……..……..……..……... 101

6.4.2 Case B – change of opening …..……..……..……..…… 106

References …… 110

Chapter 7. Forecasting Smoke Transport in Real-Time…….....……..…… 111

7.1 Potential problems and important EnKF model parameters…….....……..…. 111

7.1.1 Localization and spurious correlation …..……..……..…… 111

7.1.2 Filter divergence …..……..……..……..……..…… 114

7.1.3 Determination of measurement uncertainties …..……..……. 117

7.1.4 Ensemble perturbation strategies …..……..……..……. 118

7.1.5 Number of ensemble members …..……..……..……..…. 125

7.2 Forecasting smoke transport in a compartment fire …….……..……. 127

7.2.1 Forecasting smoke transport with constant HRR source …..……..…… 127

7.2.2 Forecasting smoke transport with non-constant HRR source …..……..…… 133

References …… 137

Chapter 8. Conclusions and Future Work…….....……..……... 138

8.1 Conclusions ……..……..……..……..……..…….. 138

8.2 Future works ……..……..……..……..……..…… 140

8.2.1 Ensemble based DA algorithms for higher dimensional systems …… 140

8.2.2 Localization by modifying observation covariance ……..…… 140

8.2.3 Other ensemble based DA algorithms ……..……..…… 141

8.2.4 Full-scale fire experiment…… ……..…… 142

8.2.5 Reconstruction of a fire scene using available information ……..…… 142

References …… 143

Appendix……...……....……..…… 144

List of Figures

Fig 1.1 Concept of data assimilation…….. 4

Fig. 3.1 Screenshot of OpenDA graphical user interface……. 25

Fig. 3.2 Screenshot of CFAST graphical user interface……... 26

Fig. 3.3 (a) Single room fire at stage A…….. 28

Fig. 3.3 (b) Single room fire at stage B……. 28

Fig. 3.3 (c) Single room fire at stage C…… 29

Fig. 3.3 (d) Single room fire at stage D……. 29

Fig. 3.4 (a) Door flow pattern in multi-room fire (Hd_2<doorH) ……. 30

Fig. 3.4 (b) Door flow pattern in multi-room fire (Hd_2>doorH) ……. 31

Fig. 3.5 Heskestad's plume model……. 34

Fig. 3.6 Equivalent convective heat transfer coefficient of a zone……. 36

Fig. 3.7 Heat balance at wall surface……. 37

Fig. 3.8 View factor of a point to a rectangular surface……... 38

Fig. 3.9 Flowchart of zone model numerical operations…….. 41

Fig. 3.10 Flowchart of EnKF forecasting and analysis steps……. 43

Fig. 4.1 CONTAM model of the manufacture house……... 50

Fig. 4.2 Examples of transient airflow rates from CONTAM outputs……... 55

Fig. 4.3 Comparisons of deterministic sequential simulation and EnKF with the measured SF_6 in the living room …….. 56

Fig. 4.4 EnKF prediction of the living room concentration by 70 ensemble members…….. 58

Fig. 4.5 Comparisons of the RMSE of the November and February cases……. 59

Fig. 4.6 Comparisons of the SF_6 prediction in the living room by different numbers of observations ……. 60

Fig. 4.7 Posteriori estimations of the SF_6 concentration in master bedroom……. 60

Fig. 4.8 Comparisons of the EnKF predictions models with different observation time steps ……. 62

Fig. 4.9 Predictability of the model near the second injection of SF_6……. 63

Fig. 5.1 Overview of the two-room test building in CFAST……. 77

Fig. 5.2 (a) Atrium smoke layer height outputs of 100 Ensemble members…….. 78

Fig. 5.2 (b) Comparisons of atrium smoke layer height outputs…….. 79

Fig. 5.3 Prediction of HRR using EnKF model…….. 80

Fig. 5.4 Prediction of mechanic ventilation rate using EnKF model……. 80

Fig. 5.5 Comparisons of atrium smoke layer height outputs (Case B1) …….. 82

Fig. 5.6 Overview of the five-zone fire test building in FDS……. 84

Fig. 5.7 Comparisons of target room smoke layer height from experiment measurements and simulation results……... 85

Fig. 5.8 Comparisons of smoke layer height outputs from FDS and CFAST in the corridor ……..... 85

Fig. 5.9 Comparisons of smoke layer height outputs in the target room for a fire of 110 kW 86

Fig. 5.10 Comparisons of the mass flow rate through the entrance two……. 87

Fig. 5.11 Comparisons of target room smoke layer height outputs……. 88

Fig. 5.12 Comparisons of target room smoke temperature outputs……... 89

Fig 6.1 (a) Description of experimental setups……... 97

Fig 6.1 (b) Experimental setups - apparatus……. 98

Fig 6.2 Visualization of smoke layer using artificial smoke and laser light……... 99

Fig 6.3 Thermocouple measurements and smokelayer height ……. 100

Fig 6.4 Comparisons of ceiling thermocouple measurement in the fire room ……. 101

Fig 6.5 Comparisons of average smoke temperature rise in three rooms ……. 103

Fig 6.6 Comparisons of smoke layer height in three rooms ……. 104

Fig 6.7 Temperature rise of target room ceiling thermocouple measurement ……. 105

Fig 6.8 Target room temperature profiles at different time ……. 106

Fig 6.9 Comparisons of smoke temperature rise in three rooms for different door setups … 108

Fig 6.10 Comparisons of smoke layer height in three rooms for different door setups …..… 109

Fig 7.1 Comparison of EnKF results using localized and non-localized Kalman gain ……. 114

Fig 7.2 Illustrations of ensemble sampling strategies……. 115

Fig 7.3 Zonal temperature distribution of the fire room……. 118

Fig 7.4 Flow field visualization using artificial smoke……. 119

Fig 7.5 Flow field visualization using aluminum oxide powder (Al_2O_3) ……. 119

Fig 7.6 Flow velocity field at fire room door from PIV results …….. 121

Fig 7.7 Location for images taken for PIV analysis……. 121

Fig 7.8 Comparisons of flow velocity field at t = 20 seconds…….. 123

Fig 7.9 Comparisons of flow velocity field at t = 70 seconds……..… 124

Fig 7.10 Probability distribution of HRR perturbation based on the Gaussian distribution… 124

Fig 7.11 (a) Comparisons of temperature forecasting error using different numbers of q… 126

Fig 7.11 (b) Comparisons of smoke layer height forecasting error using different numbers of q ……. 126

Fig 7.12 (a) to (f) Predictability of the EnKF model during a 1.5 kW fire……..… 130

Fig 7.13 (a) to (f) Predictability of the EnKF model during a 2.78 kW fire……... 131

Fig 7.14 (a) to (f) Predictability of the EnKF model during a non-constant fire……. 135

List of Tables

Table 4.1 Summary description of the manufactured house and the tracer measurement ….. 51

Table 4.2 Average airflow rates in the house ……..……..……..……..…….. 56

Table 4.3 Comparisons of root mean squared errors of different models ……..……..…. 59

Table 5.1. EnKF model parameters for three case studies ……..……..……..……... 75

Table 5.2. FDS model inputs and EnKF parameter perturbation ranges of the two-room fire tests……..……..……..……..……..……..……..……..……..……..……..……..……. 81

Table 5.3. Root mean square errors of atrium smoke layer height prediction by different methods when compared to FDS simulation results……..……..……..…… 83

Table 5.4 Comparisons of model predictability and CPU time……..……..……..…… 91

Table 6.1 Geometries and material properties of the scaled building……..……..…… 98

Table 6.2 Door position for three case setups……..……..……..……..……..……. 107

Nomenclature

Symbol	Parameter	Units
H	observation operator	
K	Kalman gain	
P	simulation error covariance	
R	measurement error covariance	
y	measurements	
x	model state	
X	model states of one ensemble member	
Hd	smoke layer height	[m]
Hn	neutral layer height	[m]
P	pressure	[Pa]
R	gas constant	[J/m^{2}K]
T	temperature	[K]
V	volume	[m^3]
m	mass	[kg]
$\dot{m}$	mass change rate	[kg/s]
E	internal energy	[joule]
Q	total heat release rate of the fire source	[kW]
$\dot{Q}_c$	convective energy release rate	[kW]
$\dot{Q}_{g\,rad}$	radiant heat absorbed by upper layer gas	[kW]
$\dot{Q}_{cU}$	convective heat transfer through upper layer surface	[kW]

$\dot{m}_p$	fire plume mass flow rate	[kg/s]
$\dot{q}$	rate of energy gain	[kW]
C_p	specific heat capacity at constant pressure	[J/kgK]
C_v	specific heat capacity at constant volume	[kJ/kgK]
D	diameter of fire area	[m]
$\dot{m}_{vent}$	mass flow rate through opening	[kg/s]
h_c	convective heat transfer coefficient	[W/m^{2}K]
F	view factor	
q	number of ensemble members	
w_{k-1}	observation white noise	
v_k	forecasting white noise	
C	gas concentration	[ppb]

Greek Alphabet Symbols

Symbol	Parameter	Units
σ_f	expected error for forecasting	
σ_o	expected error for measurement	
α_{gas}	gas absorptance	[kg/m^3]
α_w	thermal diffusivity of wall	[m^2/s]
ρ	density	[kg/m^3]
γ	C_p/C_v	
σ	Stefan-Boltzmann constant	[kg/s^{3}K^4]

Φ	control vector of forecasting model

Subscripts

Symbol	Parameter
k	time step
i	location index
U	upper layer
L	lower layer
g	Hot gases
p	plume
eq	equivalent

Superscripts

a	analysis
f	forecasted
o	observation
i	distance index of wall thickness
t	true state

Chapter 1 Introduction

1.1 General statement of the problem

The goal of building design is to create a safe, healthy and comfortable environment for the occupants. In order to achieve this goal, the most common threats to be avoided are occupational injuries and illnesses, contact with hazardous materials, and indoor air quality problems, and accidental falls that may directly cause safety concerns. Most of these potential problems would be possibly mitigated or eliminated if the details of building environment are accurately predicted. For example, toxic contaminants such as volatile organic compounds (VOCs) can be monitored and removed before the concentration reaches a harmful level. The sudden release of hazardous gases or the smoke generated from an accidental fire can also be detected and analyzed. Then, based on the results of forecasting simulations, the building control system can provide an efficient evacuation plan for all occupants in the building. However, forecasting building indoor environment is always a difficult task because ambient conditions, such as temperature, air velocity and environmental heat gain, change rapidly over time. In addition, occupants' activities, such as opening doors and windows and using electrical appliances, create more uncertainties and make the task even more challenging.

By using traditional simulation tools that utilize one set of initial inputs to forecast future physical states, the predicted physical conditions may depart from reality as the simulation progresses over time. Many new studies have shown different approaches to improving model predictability in indoor environments, with many of them suggesting the use of sensor integrated simulations (Koo et al. 2010 and Gadgil et al. 2008). By using measurement data from various sensors, the forecasting simulations can maintain a reasonable accuracy range by rapidly

updating model states and parameters. Although using measurements to improve model predictability can be as simple as utilizing sensor observations as inputs for simulation models to forecast future states, there are still a lot of other variables that must be taken into consideration, including the estimation of the uncertainties of measurements and the limitations of simulation model assumptions. Among the efforts to overcome the problems in forecasting indoor environments, this research tries to apply the method of data assimilation, which was originally widely used to solve weather forecasting problems. A detailed formulation of applying data assimilation to forecast indoor environments will be included in this thesis.

1.2 Forecasting indoor environment using data assimilation

Before the invention of numerical weather prediction technology in the last century, weather forecasting was based solely on local observation, a system whose accuracy was not satisfactory. Since the implementation of country-wide automated weather stations, the accuracy of weather predictions has significantly improved. The concept of numerical weather prediction is rather straightforward, involving the use of all available information (i.e., measurements) to produce the most accurate prediction possible (Navon, 2009).

A similar scenario is currently occurring within the field of building environment. With the increasing use of indoor sensors, more and more sensor measurement applications are being explored to improve building environments. The most significant benefit may come from improving building control strategies by using more accurate building simulation results. For example, based on the theory of model predictive control (MPC), by using forecasted future states of room air as a reference for adjusting system control parameters, these advanced control methods are able to achieve a comfortable indoor environment at reduced energy costs (Morari et

al., 1999; Fux et al., 2014).

By using measurement data to assist simulations of indoor environment, it is necessary to consider the uncertainties of simulation models and sensor measurements. The theories of data assimilation (DA) were developed for this purpose, but some DA algorithms were originally designed for weather forecasting and, therefore, may not be directly applied to other types of problems. This is due to the number of model parameters and available measurements are very different. In this research, we selected ensemble-based algorithms, which are especially suitable for low-dimensional systems (models with low number of model parameters), to forecast indoor environment. The following section includes a brief introduction to data assimilation, and further details are provided in Chapters 2 and 3.

1.2.1 Development of data assimilation

The primary goal of forecasting simulations is to efficiently and accurately predict future physical conditions. In order to find optimal state variables, data assimilation provides various algorithms for parameter estimation while also taking into account uncertainties of both measurements and numerical predictions. In general, the analysis scheme of data assimilation requires three basic components: a discrete-time model for numerical prediction, a set of observations from direct or indirect measurements, and a data assimilation scheme (Robinson, 2000). As illustrated by Fig. 1.1, by performing an analysis cycle that combines current and sometimes previous observation data with numerical forecast data, the future state of the model is predicted.

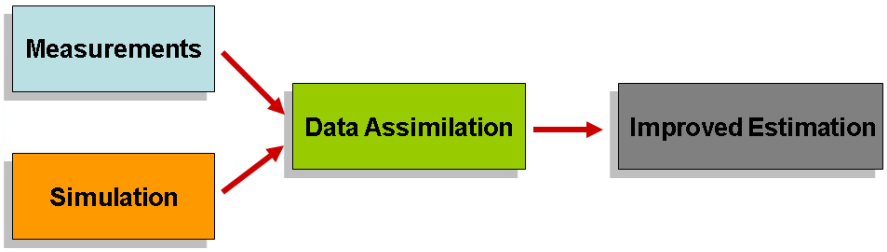

Fig. 1.1 Concept of data assimilation

For example, when the result of the numerical model and experimental measurement do not agree with each other, an optimum estimated value needs to be determined between the two by using linear analysis. Assume the measurement value is x^o and the predicted value from the numerical model is x^f. The respective variances from statistical analysis, or mean squared errors, are ${\sigma_f}^2$ and ${\sigma_o}^2$**.** Then, an optimum value can be estimated based on optimal interpolation (OI).

$$x^a = x^f + \alpha(x^o - x^f) \tag{1.1}$$

By assuming the errors from the measurements and numerical model are un-correlated, the weighted factor, α**,** can be presented as

$$\alpha = \frac{{\sigma_f}^2}{{\sigma_f}^2 + {\sigma_o}^2} \tag{1.2}$$

Although this method is efficient for simple problems, it cannot be applied to dynamic systems because it does not take time into account.

In 1960, a pioneering study of data assimilation theory was developed by R.E. Kalman. The Kalman Filter provides a recursive solution for finding the best possible estimation of the true state. Instead of finding an optimal estimation for one value, as did the previous example using OI, the Kalman Filter can be applied to a dynamic model that evolves over time. In general, the numerical operation of the Kalman Filter consists of two main steps 1) Forecasting Step: a forecasting step uses a discrete-time model to predict the future state of interest. In the Kalman Filter, a linear stochastic model is used to predict the future state

$$x_k^f = \mathbf{A}x_{k-1} + \mathbf{B}u_{k-1} + w_{k-1} \tag{1.3}$$

where the matrix **A** relates the model state from time step *k-1* to *k*, the matrix **B** is the control-input variable that relates the control vector *u* (e.g., it can be initial and boundary condition variables or other important physical parameters to the problem of interest) to the model state *x*, and *w* is a random white noise. The measurements corresponding to the model state can be expressed as

$$y_k = \mathbf{H}x_k + v_k \tag{1.4}$$

where the matrix **H** is an observation operator that relates the model states *x* to the measurement *y,* and *v* is the observation noise. For example, when measurement does not fall exactly on the grid point of a simulation model, **H** can be a linear weighted factor to find the forecasted measurement in the model space.

(2) Analysis Step: an analysis step uses direct and/or indirect measurements to correct the predicted value from the forecasting step. An optimum value,x_k^a can be estimated based on Best Linear Un-biased Estimation (BLUE) as

$$x_k^a = x_k^f + \mathbf{K}_k(y_k - \mathbf{H}x_k^f) \tag{1.5}$$

where

$$\mathbf{K}_k = \frac{\mathbf{P}_k\mathbf{H}^T}{\mathbf{H}\mathbf{P}_k\mathbf{H}^T + \mathbf{R}} \tag{1.6}$$

Eq. (1.5) is the original format of the Kalman Filter, which attempts to find a weighted factor, so-called Kalman gain, $\mathbf{K}_k$, which determines optimal states by considering both numerical model and measurements. $\mathbf{P}_k$ is the simulation error covariance, and **R** is the expected measurement error or the covariance of v_k from Eq. (1.4). The term $(y_k - \mathbf{H}x_k^f)$ is called the residual or innovation, which describes the differences between real measurement and forecasted

measurement.

To better understand the role of the Kalman gain, it may be helpful to observe two extreme cases. For highly accurate observation data, observation error variance, **R**, approaches zero. The Kalman gain or the weighted factor to the residual will increase. Then, the Kalman gain in Eq. (1.5) can be expressed as

$$\lim_{R\to 0} \mathbf{K}_k = \mathbf{H}^{-1} \tag{1.7}$$

By substituting Eq. (1.7) with Eq. (1.6)

$$\lim_{R\to 0} x_k^{ai} = \mathbf{H}^{-1} y_k^i \tag{1.8}$$

For highly accurate observations, the analysis weighs more on the measurements, ${y_k}^i$.

For the other instance, when a forecast model is very accurate, error covariance $\mathbf{P}_k^f$ approaches zero, so

$$\lim_{P_k\to 0} \mathbf{K}_k = 0 \tag{1.9}$$

Then,

$$x_k^a = x_k^f \tag{1.10}$$

This means that the residuals do not have an effect on the analysis result (Welch and Bishop, 2006), and the best estimated value depends solely on the numerical forecast from Eq. (1.3).

There are three major limitations in implementing the Kalman Filter in solving building environment problems: (1) the computational cost is relatively high, (2) the model dynamics are usually non-linear and (3) error sources are not easy to characterize (Thomas and Whitaker 2002).

1.2.2 Categories of data assimilation algorithms

In addition to the linear Kalman Filter model, many other variations of data assimilation methods

have been developed, most of which are for non-linear systems. These DA algorithms can be categorized into three major groups.

(1) Direct solving large matrices

Similar to the Kalman Filter, these data assimilation methods use the linear tangent model and its adjoint matrix to estimate simulation error variance (i.e., expected error for direct simulation). The process of problem solving is adopted from Taylor series expansions by linearizing the model. These DA methods are considered highly accurate but are usually very computationally expensive, especially when solving a high-dimensional system (i.e., model with large number of parameters). The most well-known example, the extended Kalman Filter (XKF), can significantly improve simulation model performance, but it requires a very large amount of computational resources (Ljung 1979).

In XKF, a discrete-time or continuous-time model can be applied to forecast model states. When measurements become available, XKF can perform an analysis cycle similar to traditional Kalman filter but using linearized estimation. Therefore, large amount of information needs to be saved. Although XKF is considered sub-optimal in comparison to the original Kalman Filter, it still yields reasonable predictions and is widely used in many applications, such as global positioning systems (GPS) and other types of navigation systems.

(2) Variational methods

Another popular type of DA theories is based on variational methods, which are widely used in weather forecasting (Courtier and Talagrand, 1987). Variational analysis minimizes a cost function by considering both measurement and simulation errors. First, the numerical model predicts the values of all of the measurements and searches for the best fit. In the three-dimensional-variational (3D-Var) method, the cost function is presented as

$$J(x) = \frac{1}{2}(x - x^f)^T \mathbf{P}^{f^{-1}}(x - x^f) + \frac{1}{2}(y - H(x))^T \mathbf{R}^{-1}(y - H(x)) \quad (1.11)$$

where $\mathbf{P}^f$ is the forecasting error covariance and $\mathbf{R}$ is the observation error covariance. By minimizing this function, the analysis model's states remain within a reasonable range of the measurements. However, the limitation is that when observation operators are non-linear, the analysis results sometimes may only present local minimums. This is a very commonly-found problem when solving a highly-non-linear problem using linearization methods.

Similar to 3D-Var, four-dimensional-variational (4D-Var) is another variational method, in which the simulation observation operator, *H*, updates in every time step, and the cost function can be written as

$$J(x) = \frac{1}{2}[(x - x^f)^T \mathbf{P}^{f^{-1}}(x - x^f) + \sum_{k=1}^{n}(\mathrm{y}_k - H_k(x_k))^T \mathbf{R}_k{}^{-1}(y_k - H_k(x_k))] \quad (1.12)$$

In order to calculate the gradient of the cost function for minimization at all time steps, it is necessary to manipulate large matrices, which makes 4D-Var computationally intensive. Nevertheless, the capability of 4D-Var to maintain long-term forecasting accuracy in numerical weather prediction has been proven to be superior to that of 3D-Var.

(3) Ensemble-based algorithms

Evensen (1994) proposed a new affordable DA approach. The Ensemble Kalman Filter (EnKF) uses the Monte Carlo method to estimate analysis error covariance and determine Kalman gain without using a tangent linear operator. Unlike the aforementioned methods, EnKF does not require the calculation of adjoint matrices, which makes it relatively affordable and easy to implement.

In this thesis, an ensemble-based data assimilation method is applied to solve indoor environment forecasting problems. Detailed discussions about ensemble-based algorithms will be presented in the following chapters.

1.3 General research objectives and thesis outline

Among available studies of forecasting indoor environment, there is a substantial minority of researches relating to occupant safety and emergency response. This may be because forecasting simulations associated with life safety concerns demand higher accuracy than those concerned with comfort and energy savings. Thus, the forecasting simulations are not generally employed to solve building safety problems. Therefore, this study focuses first on simulations of building safety problems since they are more challenging than other types of forecasting due to higher accuracy expectations. By thoroughly studying the modeling parameters of ensemble-based data assimilation algorithms, the method can generally be applied to solve various indoor environmental problems.

This thesis is organized as follows:

▪Chapter 2 provides literature reviews of different methods for forecasting indoor environment and the potential problems with these existing methods. The scope of review is extended to finding possible improvements and/or solutions to these problems. Because the solution proposed in this thesis is based on data assimilation, the review also covers different types of data assimilation algorithms with more details than the foregoing general introductions.

▪Chapter 3 outlines the research objectives and methodologies of applying the Ensemble Kalman Filter (EnKF) to forecast indoor environment and solve different types of problems. This thesis focuses on solving building safety problems, which demands short processing time and high accuracy. In addition to EnKF equations, this chapter also includes the formulations of the compartment smoke transport model, which will be applied to real-time forecasting of building fire accidents in Chapter 7. Please note that, to avoid repetition, the detailed methodologies

presented in Chapters 4 and 5 are not included in Chapter 3.

▪ Chapter 4 is the first case study, which shows that indoor contaminant transport can be predicted by integrating measurements from multiple sensors. Important parameters are investigated, and a possible application to assist in the emergency response to toxic gas releases for buildings with high-level security requirements is discussed. The predicted information can be used to assist in the automated control of mechanical ventilation systems to remove hazardous contaminants, while assisting in occupant evacuation when toxic gases are detected.

▪Chapter 5 is the second case study, which demonstrates another application to predict fire and smoke dispersion to improve building fire safety. To apply the model to an operating building, the source strength of an unknown fire accident can first be estimated by the fuel load and ventilation conditions of a given space. When a fire accident occurs and the fire alarm is activated, the fire source is assumed to be located in the closest room to the triggered smoke detector and measurements are taken from the sensors. After calibrating the simulation model with sensor measurements using DA, the simulation can generate a more accurate prediction of fire growth and smoke dispersion, which can be used in automated smoke management, evacuation assistance and decision making in firefighting.

▪Chapter 6 conducts a scaled compartment fire experiment to study the effects of changing fire source strength and window/door openings on the spread of smoke. These events are very common in a real compartment fire scenario but are usually hard to predict. The measurements obtained from the experiments are then used in Chapter 7 to verify the predictability of the DA-

assisted smoke spread prediction.

▪Chapter 7 develops a DA-assisted zone model to predict real-time smoke spread in a multi-room building fire. The model only uses an initial guess range of fire source strength to predict unknown fire events. By applying EnKF, the model can statistically update zone model parameters and predict smoke transport with reasonable accuracy during a fire. In the early stages of a fire, the predicted smoke spread can be very valuable to automated smoke management, evacuation assistance and decision making in firefighting.

▪Chapter 8 summarizes the results of all of the case studies and concludes the current stage of the research. Recommendations for applying DA to solve other building environment problems and other future works are also included in this chapter.

References

Gadgil, Ashok, Michael Sohn, and Priya Sreedharan. "Rapid Data Assimilation in the Indoor Environment: Theory and Examples from Real-Time Interpretation of Indoor Plumes of Airborne Chemical." In *Air Pollution Modeling and Its Application XIX*, pp. 263-277. Springer Netherlands, 2008.

Ljung, Lennart. "Asymptotic behavior of the extended Kalman filter as a parameter estimator for linear systems." *Automatic Control, IEEE Transactions on* 24, no. 1 (1979): 36-50.

Courtier, Philippe, and Olivier Talagrand. "Variational assimilation of meteorological observations with the adjoint vorticity equation. II: Numerical results." *Quarterly Journal of the Royal Meteorological Society* 113, no. 478 (1987): 1329-1347..

Evensen, Geir. "Sequential data assimilation with a nonlinear quasi‐geostrophic model using Monte Carlo methods to forecast error statistics." *Journal of Geophysical Research: Oceans (1978–2012)* 99, no. C5 (1994): 10143-10162.

Kalman, Rudolph Emil. "A new approach to linear filtering and prediction problems." *Journal of Fluids Engineering* 82, no. 1 (1960): 35-45.

Navon, Ionel M. "Data assimilation for numerical weather prediction: a review." In *Data Assimilation for Atmospheric, Oceanic and Hydrologic Applications*, pp. 21-65. Springer Berlin Heidelberg, 2009.

Morari, Manfred, and Jay H Lee. "Model predictive control: past, present and future." *Computers & Chemical Engineering* 23, no. 4 (1999): 667-682.

Fux, Samuel F., Araz Ashouri, Michael J. Benz, and Lino Guzzella. "EKF based self-adaptive thermal model for a passive house." *Energy and Buildings*68 (2014): 811-817.

Robinson, Allan R., and Pierre FJ Lermusiaux. "Overview of data assimilation." *Harvard reports in physical/interdisciplinary ocean science* 62 (2000): 1-13.

Koo, Sung-Han, Jeremy Fraser-Mitchell, and Stephen Welch. "Sensor-steered fire simulation." *Fire Safety Journal* 45, no. 3 (2010): 193-205.

Welch, Greg, and Gary Bishop. "An introduction to the Kalman filter." (1995).

Chapter 2 Literature Review

The literature review focuses on the methods used to forecast building and indoor environment. In addition, potential problems presented by these methods are discussed, as well as possible improvements and solutions to these problems. Finally, general methodologies based on the review are outlined.

2.1 Forecasting indoor environment

Due to the general public's growing awareness of energy conservation and carbon emissions reduction, environmental responsibility and resource efficiency are important factors in a successful building design. In order to satisfy these new design criteria, new building design features, such as hybrid ventilation systems (utilizing both natural and mechanic ventilation), building integrated photovoltaic enclosure and performance-based fire safety design, have been introduced, and indoor environment forecasting plays an important role in improving the performance of these new building control systems. Various forecasting methods have been employed with this in mind. For a photovoltaic system, the energy generation and consumption can directly affect system performance. Heinemann (2006) conducted an overview of different methods of forecasting solar radiation, and the report indicates that the long-term (one- to- two-day) forecasts are highly inaccurate and require improvement. For building energy performance, Zhao (2012) reviewed different models for predicting building energy consumption, including statistical models, transparent-box models (engineering methods), black-box models (neural networks) and grey-box models (hybrid methods using incomplete or uncertain data). The results indicate that without a comparison under the same circumstances, it is difficult to determine the

best method for forecasting building energy consumption. For example, the engineering method is accurate, but the process of preparing appropriate inputs can be complex and difficult. In contrast, the statistical method is easy to implement, but overly simplified correlations make it less accurate. Black-box models, such as artificial neural networks (ANNs), perform well on non-linear problems but are sometimes out-performed by support vector machines (SVMs). The major drawback of these two black-box methods is the large amount of historical data that is usually required to make the model efficient. Overall, the existing studies still lack a comparison basis and a clear indication of which method is better at forecasting building energy consumption.

Many recent studies have reported using AI techniques, including ANNs, and genetic algorithms (GA) to improve the design of building envelope. Caldas and Norford (2003) employed genetic algorithms to optimize building envelope design and control of HVAC systems. The reported model successfully optimizes building envelope design and HVAC systems, including duct sizing, while minimizing the system costs and satisfying design criteria. Magnier and Haghighat (2010) proposed an optimization method using a combination of an ANN and a Multi-objective Evolutionary Algorithm for building envelope design. The reported model is able to give a large number of potential design alternatives, which is a significant benefit in preliminary building design.

Foucquier et al. (2013) recently introduced state-of-the-art modeling for forecasting building thermal behaviors, including building ventilation. The physical models are categorized into three major groups: computational fluid dynamic (CFD), zonal, and nodal (multi-zone) approaches. Although each of these three approaches has its own advantages and disadvantages, they all share a common major problem, which is the difficulty of preparing input data. The input

parameters for these models usually require meteorological data, geometrical data, thermo-physical properties, occupancy and equipment loads. These parameters are highly dynamic in a real building environment and usually cannot be directly determined by sensor measurements.

Another type of review is based on a specific method that can be applied to solve various forecasting problems related to building and indoor environment. Kalogirou (2001) conducted a review of ANNs in renewable energy systems. The review covers a large variety of applications, including solar heating, PV, wind speed and different types of building load predictions. Similar to other approximation methods, the results indicate that ANNs also have relative advantages and disadvantages, but there are no rules for determining the suitability for ANNs for specific types of application. However, in general, compared to other artificial intelligence techniques, ANNs perform well in short-term load and in system modeling and control (Krati 2003).

To summarize, most building and indoor environment models show promising predictability in solving certain types of problems, but the limitations fall into two major areas. The first is that the inputs prepared for the models are always expressed under certain uncertainties and further affect forecasting accuracy. The second is that the uncertainties associated with model assumptions reduce model predictability. These uncertainties are unavoidable no matter how reliable the predictions generated by the model.

2.2 Forecasting indoor environment using data assimilation

In order to reasonably predict physical states of the indoor environment, the input parameters for the simulation models should also dynamically change with the current ambient environment. Although using measurement data to directly update input parameters may improve model predictability, the uncertainties of the measurements will still affect the forecasting accuracy. In

addition, sensor resolutions are another factor that may hinder the process of obtaining measurement data. For example, increasing the number of sensors or shorten the measurement time interval will also demand higher computer resource to perform prediction for building environment while also increases total system cost. In order to solve this problem, it is essential to find an affordable method that can utilize measurement data to its maximum potential to forecast indoor environment. The reviews are categorized into three groups by their applications:

(1) Building ventilation and indoor air quality - Platt et al. (2010) introduced a simple real-time HVAC zone model that is based on only a few parameters. By implementing a feedback-delayed Kalman Filter, the model is able to deal with short-term random changes and long-term accumulated errors and perform promising forecasting of indoor temperature. But, the experiments are mainly based on a constant air supply set-point. The case studies for more dynamic environments are yet to be explored. Brabec and Jilek (2007) develop a model to predict radon concentration in a house based on an Extended Kalman Filter. The model recognizes change in source strength and air exchange rate and performs noticeable predictability. The disadvantage of this model, as with most Extended Kalman Filter models, is the long length of time required for numerical calculations.

(2) Fire and smoke predictions - Ma et al. (2010) proposed an approach to detecting fire smoke in an open area based on the Kalman Filter and Gaussian mixture color model. The experiments are conducted outdoors, but the methodology is generally applicable to indoor environment. The results show that the fires smoke can be detected using the proposed method, but for a fire safety system, it may require large amounts of video cameras in order to capture the images of the fire smoke regions. Progri et al. (2000) introduced a GPS-like model to assist firefighters in navigating inside burning buildings. The model is based on a Kalman filter to provide real-time

location and emergency exit guidance. The measurements are based on visible pseudolites to capture the relative positions of the firefighters. The model is validated by numerical data and shows reasonable accuracy. The model still requires further validation because the visibility in fire smoke can be very poor, so the accuracy requirement may be higher in a real building fire.

(3) Building control - Yang (2003) introduced a condition-based failure prediction and processing scheme for building preventive maintenance. The system is based on a Kalman filter and indicates where and when the system failure will occur. However, Arunraj and Maiti (2010) point out that condition-based maintenance is not cost efficient if the diagnostic is not done properly. Luan et al. (2012) proposed an unscented Kalman filter (UKF) model to solve the state estimation problem of greenhouse climate control systems. The analysis method is similar to an extended Kalman filter but performs much better at highly non-linear problems since the analysis is based on a small set of sample points using non-linear functions. The model can satisfy the conditions for plant growth even with missing measurements, but when accurate measurements are available, the UKF does not contribute much to system performance.

2.3 Ensemble based data assimilation algorithms

Since Evensen (1994) introduced EnKF, many variations of EnKF have been proposed based on the same concept of statistics modeling used to transform forecast ensemble into analysis ensemble. The main differences between these methods are the analysis scheme and the use of perturbed or unperturbed observations. In order to select an appropriate method to forecast and improve building environment, the following reviews summarize four ensemble-based DA algorithms.

2.3.1 Ensemble square root filter (EnSRF)

The concept of square root filtering of a Kalman Filter was first proposed by Andrews (1968) and later developed into an ensemble-based DA method by Anderson (2001). Unlike EnKF, which sequentially updates all ensemble members using Kalman Gain, the observations of EnSRF are only assimilated to update ensemble mean in the analysis step.

$$\overline{x_k^a} = \overline{x_k^f} + \mathbf{K}_k(y_k - \mathbf{H}\overline{x_k^f}) \tag{19}$$

By assuming the forecast ensemble perturbation can be estimated by a transform matrix $\mathbf{T}_{k,}$

$$\mathbf{X}_k^a = \mathbf{T}_k \mathbf{X}_k^f \tag{20}$$

and the best estimated model states after analysis can be presented as

$$x_k^a = \overline{x_k^a} + \mathbf{X}^a \tag{21}$$

It can be observed that the update of the model states is performed deterministically and no perturbations of observation are needed. Because the extra source of error from observation is eliminated, EnSRF can out-perform EnKF in some cases (Tippett et al. 2003).

2.3.2 Local ensemble transform Kalman filter (LETKF)

Local ensemble transform Kalman Filter is another type of ensemble-based algorithm similar to EnSRF. As its name indicates, the LETKF performs data assimilation within a local space. Each model state is updated with its own local observations (i.e., measurements within a predefined distance) simultaneously and can be written as,

$$x_k^a = x_k^f + \mathbf{P}_{k,loc}^f \cdot \mathbf{K}_{k,loc} \cdot \mathbf{y}^o \tag{22}$$

where the subscript, *loc,* means local, and y^o is the global observation increment, including the observations outside of the "local" range.

The advantage of using local observations in model state analysis is that the uncorrelated

observation covariance can be excluded since they are outside the range being considered. But, a possible problem with LETKF is caused by the use of local observations simultaneously (Tsyrulnikov 2010), which leads to the assumption that each group of observations used in the analysis have zero correlations. However, for some apparatuses, multiple measurements are performed together in one area, so the correlations do exist. For example, photographs taken by infrared cameras are commonly found in building environment observation. Systematic measurement errors from the camera may significantly reduce model efficiency due to the error covariances are not correctly estimated, so special care must be taken when applying this algorithm. Increasing the distance of local space to include more measurements may reduce this effect, but it also increases computational costs and reduces the benefits of localization. Overall, LETKF can be beneficial due to its built-in localization analysis, but on the other hand, flexibility in analyzing measurement uncertainties is lost.

2.3.3 Deterministic ensemble Kalman filter (DEnKF)

Deterministic ensemble Kalman Filter (DEnKF) is another variation of EnKF using unperturbed observations. The analysis scheme of DEnKF can be considered a linear approximation of EnSRF, and the analyzed error covariance can be expressed as

$$\mathbf{P}^a = \mathbf{P}^f - 2\mathbf{KHP}^f + \mathbf{KHP}^f\mathbf{H}^T\mathbf{K}^T \tag{23}$$

Since the quadratic term, $\mathbf{KHP}^f\mathbf{H}^T\mathbf{K}^T$, is relatively small and negligible, the residuals in the analysis can be presented as,

$$\mathbf{A}^a = \mathbf{A}^f - \frac{1}{2}\mathbf{KHA}^f \tag{24}$$

and the best estimated model states for ensemble members can be determined by

$$\mathbf{X}_k^a = \mathbf{A}^a + [x^a, \dots, x^a] \quad (25)$$

This process is similar to applying half of Kalman Gain to ensemble updating to approximate the error covariance in Eq. (24). As long as there is no perturbation of observations, it is considered as a deterministic EnKF (Sakov and Oke 2007). The DEnKF has been proven to be superior to EnSRF in some cases and it allows for the application of Schur-product-based localization methods. But, the reported models are more robust and may encounter filter divergence problems more frequently compared to other ensemble-based algorithms.

2.3.4 Ensemble Kalman filter (EnKF)

The models presented in this thesis are based on the ensemble Kalman filter method. The EnKF uses perturbed observation to maintain a reasonable range of ensemble spread in order to avoid filter divergence (Burgers et al. 1998). The EnKF is relatively more stable compared to other methods but is sometimes considered suboptimal due to the additional observation noises (Sakov and Oke 2008). However, when EnKF is applied to high dimensional systems, its stability becomes significant due to the lower number of ensemble members required (Oke et al. 2007). A detailed formulation of the EnKF is presented in Chapters 3, 4, 5 and 7.

References

Heinemann, Detlev, Elke Lorenz, and Marco Girodo. "Forecasting of solar radiation." *Solar Energy Resource Management for Electricity Generation from Local Level to Global Scale* (2006): 223-233.

Zhao, Hai-xiang, and Frédéric Magoulès. "A review on the prediction of building energy consumption." *Renewable and Sustainable Energy Reviews* 16, no. 6 (2012): 3586-3592.

Magnier, Laurent, and Fariborz Haghighat. "Multiobjective optimization of building design using TRNSYS simulations, genetic algorithm, and Artificial Neural Network." *Building and Environment* 45, no. 3 (2010): 739-746.

Caldas, Luisa Gama, and Leslie K. Norford. "A design optimization tool based on a genetic algorithm." *Automation in construction* 11, no. 2 (2002): 173-184.

Huchuk, Brent, Cynthia A. Cruickshank, William O'Brien, and H. Burak Gunay. "Recursive thermal building model training using Ensemble Kalman Filters."

Yang, S. K. "A condition-based failure-prediction and processing-scheme for preventive maintenance." *Reliability, IEEE Transactions on* 52, no. 3 (2003): 373-383.

Oldewurtel, Frauke, Dimitrios Gyalistras, Markus Gwerder, Colin Jones, Alessandra Parisio, Vanessa Stauch, Beat Lehmann, and Manfred Morari. "Increasing energy efficiency in building climate control using weather forecasts and model predictive control." In *Clima-RHEVA World Congress*, no. EPFL-CONF-169735. 2010.

Radecki, Peter, and Brandon Hencey. "Online building thermal parameter estimation via unscented Kalman filtering." In *American Control Conference (ACC), 2012*, pp. 3056-3062. IEEE, 2012.

Rodrigues, Giovani Guimaraes, U. S. Freitas, D. Bounoiare, Luis Antonio Aguirre, and Christophe Letellier. "Leakage estimation using Kalman filtering in noninvasive mechanical ventilation." *Biomedical Engineering, IEEE Transactions on* 60, no. 5 (2013): 1234-1240.

Platt, Glenn, Jiaming Li, Ronxin Li, Geoff Poulton, Geoff James, and Josh Wall. "Adaptive HVAC zone modeling for sustainable buildings." *Energy and Buildings* 42, no. 4 (2010): 412-421.

Foucquier, Aurélie, Sylvain Robert, Frédéric Suard, Louis Stéphan, and Arnaud Jay. "State of the art in building modelling and energy performances prediction: A review." *Renewable and Sustainable Energy Reviews* 23 (2013): 272-288.

Kalogirou, Soteris A. "Artificial neural networks in renewable energy systems applications: a review." *Renewable and sustainable energy reviews* 5, no. 4 (2001): 373-401.

Progri, Ilir F., William R. Michalson, John Orr, and David Cyganski. "A system for tracking and locating emergency personnel inside buildings." In *Proc. ION-GPS*, pp. 560-568. 2000.

Ma, Li, Kaihua Wu, and L. Zhu. "Fire smoke detection in video images using Kalman filter and Gaussian mixture color model." In *Artificial Intelligence and Computational Intelligence (AICI), 2010 International Conference on*, vol. 1, pp. 484-487. IEEE, 2010.

Lin, Yung Chin, Kuo Lan Su, and Cheng Yun Chung. "Development of Intelligent Fire Detection Module Using Optic-Sensors." *Applied Mechanics and Materials* 300 (2013): 440-443.

Luan, Xiaoli, Yan Shi, and Fei Liu. "Unscented Kalman filtering for greenhouse climate control systems with missing measurement." *International Journal of Innovative Computing,*

Information and Control 8, no. 3 (2012): 2173-2180.

Arunraj, N. S., and J. Maiti. "Risk-based maintenance policy selection using AHP and goal programming." *Safety science* 48, no. 2 (2010): 238-247.

Brabec, Marek, and Karel Jílek. "State-space dynamic model for estimation of radon entry rate, based on Kalman filtering." *Journal of environmental radioactivity* 98, no. 3 (2007): 285-297.

Burgers, Gerrit, Peter Jan van Leeuwen, and Geir Evensen. "Analysis scheme in the ensemble Kalman filter." *Monthly weather review* 126, no. 6 (1998): 1719-1724.

Sakov, Pavel, and Peter R. Oke. "A deterministic formulation of the ensemble Kalman filter: an alternative to ensemble square root filters." *Tellus A* 60, no. 2 (2008): 361-371.

Hamill, Thomas M., Jeffrey S. Whitaker, and Chris Snyder. "Distance-dependent filtering of background error covariance estimates in an ensemble Kalman filter." *Monthly Weather Review* 129, no. 11 (2001): 2776-2790.

Oke, Peter R., Pavel Sakov, and Stuart P. Corney. "Impacts of localisation in the EnKF and EnOI: experiments with a small model." *Ocean Dynamics* 57, no. 1 (2007): 32-45.

Andrews, Angus. "A square root formulation of the Kalman covariance equations." *AIAA Journal* 6, no. 6 (1968): 1165-1166.

Anderson, Jeffrey L. "An ensemble adjustment Kalman filter for data assimilation." *Monthly weather review* 129, no. 12 (2001): 2884-2903.

Tippett, Michael K., Mathew Barlow, and Bradfield Lyon. "Statistical correction of central southwest Asia winter precipitation simulations." *International journal of climatology* 23, no. 12 (2003): 1421-1433.

Tsyrulnikov, Mikhail. "Is the Local Ensemble Transform Kalman Filter suitable for operational data assimilation?." *COSMO Newsletter* 10 (2010): 22-36.

Whitaker, Jeffrey S., and Thomas M. Hamill. "Ensemble data assimilation without perturbed observations." *Monthly Weather Review* 130, no. 7 (2002): 1913-1924.

Krarti, Moncef. "An overview of artificial intelligence-based methods for building energy systems." *Journal of Solar Energy Engineering* 125, no. 3 (2003): 331-342.

Evensen, Geir. "Sequential data assimilation with a nonlinear quasi-geostrophic model using Monte Carlo methods to forecast error statistics." *Journal of Geophysical Research: Oceans (1978–2012)* 99, no. C5 (1994): 10143-10162.

Chapter 3 Methodologies

The theories of data assimilation provide various methods to integrate sensor data to improve model predictability. Among all data assimilation methods, ensemble-based algorithms are especially suitable for real-time prediction of indoor environment due to its low computational requirements and easily implementation. The main objective of this research is to thoroughly study the modeling parameters of ensemble-based data assimilation algorithms and apply the model to solve indoor environment problems.

In order to achieve this objective, the research work includes:

- Develop a simple model to study the theory of data assimilation and to verify the algorithms in a building environment problem.
- Apply EnKF to solve an indoor environment problem by integrating experimental measurements, identify and quantify important parameters.
- Integrate existing indoor environment simulation models with ensemble-based DA algorithms; compare the results with validated cases.
- Based on previous models, compare different ensemble-based DA algorithms to develop a general methodology and thoroughly study all relating model parameters.
- Develop a model using low dimensional system to solve large scale non-linear problems in building environment.
- Conduct an experiment to gather observations for data assimilation.
- Posteriori estimation of important model parameters and quantifying the simulation and observation uncertainties.
- Develop a model to forecast building environment by using real-time sensor data.

3.1 Research methodologies

In order to achieve the research objectives, simulation models with different levels of complexity need to be built. Instead of making a fresh start, the research begins with using a DA toolbox, OpenDA (Verlaan et al., 2010) developed by Delft University of Technology, Netherland. The software (Fig. 3.1) is designed as an open-source platform in which all users can quickly develop and share their own model or implement new data assimilation methods. OpenDA also provides an option to work with external programs by using a black-box wrapper which links a simulation tool to data assimilation toolbox. Overall, it allows users to optimize their existing model by using customized or default data assimilation algorithms without the need of complex programming.

In the early stage, several models are studied by applying different algorithms including conventional computer models without using DA methods. From the test model, EnKF is chosen as DA algorithm since it is more flexible and easy to implement than other algorithms. For example, noise models and different localization methods can be directly implemented. By comparing the results with DA implementation, important parameters such as quantifying uncertainties, ensemble numbers and the effects of observation time step can be studied to outline an EnKF model.

After the fundamental model setups are studied, a model to forecast indoor environment is conducted by calibrating simulation models with experimental measurements. This case study includes different sets of measurement data to verify the model predictability in different environmental conditions. At this stage, the capability of EnKF model to forecast indoor environment is confirmed and the next step is applying EnKF to more complex models to solve other forecasting problems.

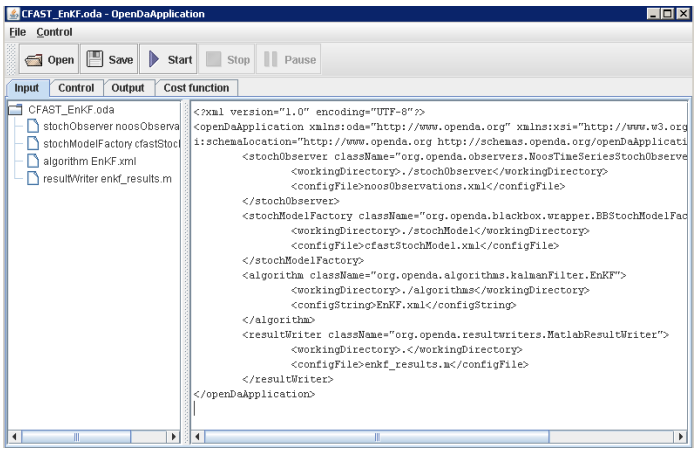

Fig. 3.1 Screenshot of OpenDA graphical user interface

After verifying the predictability of EnKF models in previous case studies, the goal of the next stage focuses more on solving more practical problems such as the limitations of existing indoor simulation model. From the reviews, CFAST (Peacock et al., 2005) and CONTAM (Walton and Dols, 2012) are chosen since they are both node-based and are very suitable for the ensemble-based DA algorithms. After the CONTAM model is completed, this research starts doing comparisons of different algorithms using different models. The comparisons include using pure numerical experiments, CFD simulation outputs and experimental measurements as model observations. Model parameters of each algorithm are reviewed independently with both CFAST and CONTAM models while detailed setups of using ensemble-based algorithms to forecast indoor environment are generally illustrated. Based on the setups, a new building simulation model using ensemble-based DA algorithms can be conducted including localization.

Finally, based on the experience gained from this model, a stand-alone DA-integrated building simulation model is built. The new model is able to take real-time sensor measurements, process them and used to improve forecasting of building environment. Following sections in this chapter present the background theories of this model.

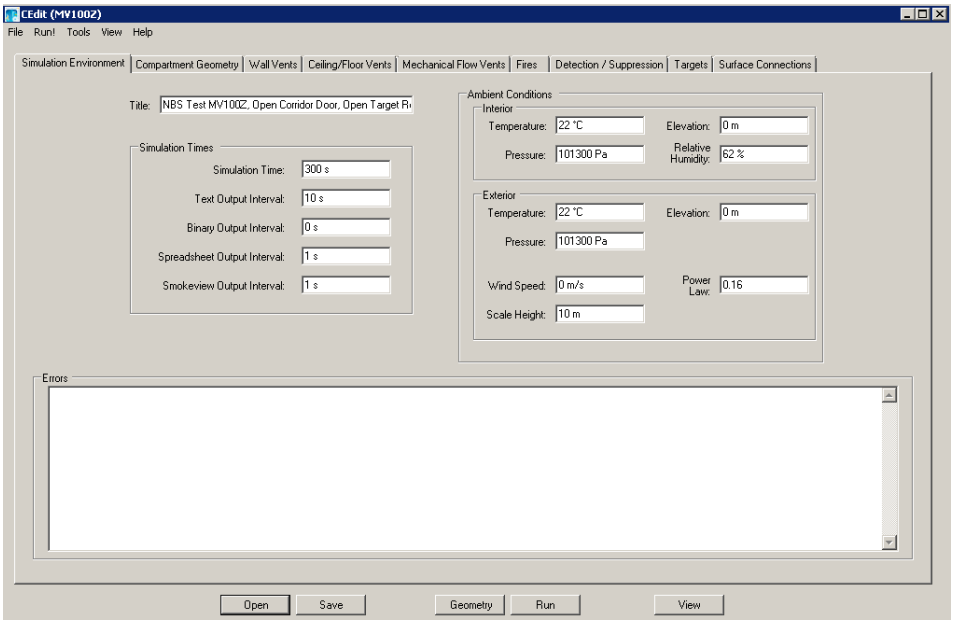

Fig. 3.2 Screenshot of CFAST graphical user interface

3.1.1 Introduction of zone model

The concept of zone fire model appears to be first introduced by Fowkes (1973) and is later developed into several different computer-based models. Different from network model saving one set of model states at each node, the zone model divides the air inside a compartment into two zones (control volumes) where the upper layer is a higher-temperature zone and the bottom layer is a lower-temperature zone. The gas properties within a zone are assumed evenly distributed without zonal deviations. According to the reviews conducted by Jones and Forney (1993), the first multi-room model that simulates the horizontal gases flow through openings is formulated by Tanaka (1983). In the model, the gas flow rate through a door or window is determined by the physical properties of the linked zones.

Single-room fire

The major assumption of a zone model is that each compartment is separated into two control volumes, upper layer and lower layer, in which the important physical states, such as

temperature, gas concentration and gas density are considered uniformly-distributed. The upper layer is filled with gases coming from the plume above the fire source so the air within the upper layer has higher temperature and lower density. For the lower layer, the air temperature is lower and the density is higher. By applying conservation of mass and energy to each layer, the gradient of important physical properties such as pressure, density, temperature and volume can be estimated. So the smoke transport problem is simplified to determining two source terms of enthalpy and mass flux: the flow rate of the fire plume and the flow rate through the openings.

First, the determination of plume flow rate in zone models is based on several plume models deriving from experiment results. For example, the Heskestad plume, the McCaffrey plume and the Zukoski plume (Heskestad 1984; McCaffrey 1983 and Zukoski 1994) are widely used since the equations cover a large range of fire heat release rate and vertical travel distance.

Second, the flow rates through vertical vents (door/windows) are determined by the pressure difference along the height using orifice equation and can be categorized into four major stages. Fig. 3.3 (a) to (d) demonstrates the four types of flow pattern and the pressure profile for one-room compartment fire from ignition to fully developed fire. As shown in Fig. 3.3 (a), when the hot gases start to accumulate in the fire room and establish an interface between hot gases and cold air at height H_d, the total pressure in the room rises and pushes the lower layer air outside the opening.

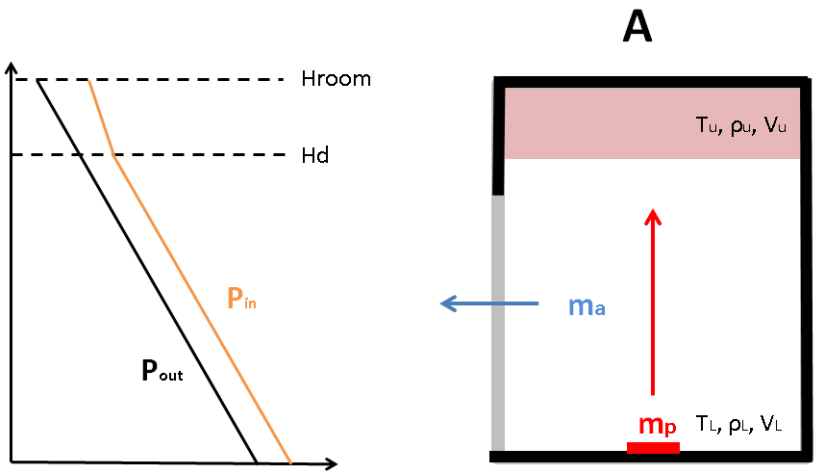

Fig. 3.3 (a) Single room fire at stage A

After the smoke layer is well-developed and the smoke layer descents below the height of door soffit, hot air starts to flow out of the opening as illustrated by Fig. 3.3 (b). At this stage, the pressure rise due to expansion of gases is higher than that of hydrostatic pressure drop. So the hot gases and cold gases both flow out of the opening. Comparing to other three stages, this stage has relatively short duration which can be only several seconds in most compartment fire cases.

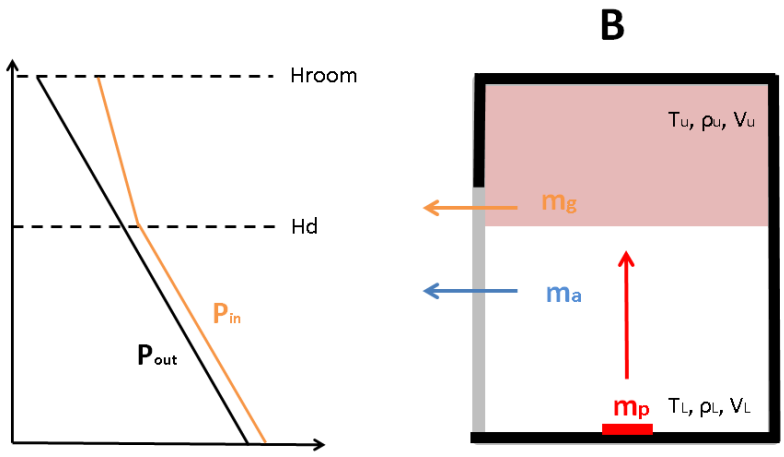

Fig. 3.3 (b) Single room fire at stage B

When the smoke layer is well-below the door soffit, the cold air starts to get into the fire room through the opening since the pressure difference at the bottom of the upper layer becomes negative. As shown in Fig. 3.3 (c), in this stage, a location where the flow pattern changes its

direction can be found and is called neutral layer, which is presented as H_n since the pressure difference of the fire room and the adjacent zone is zero at this specific height.

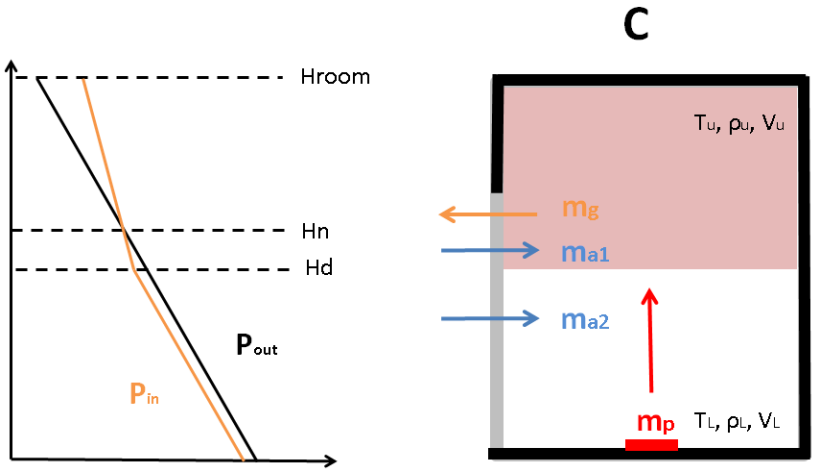

Fig. 3.3 (c) Single room fire at stage C

For a room located far-away from the fire source or for long-duration compartment fire cases especially for those are post-flashover fire (nearly all exposed combustible materials are ignited), the room air is considered well-mixed instead of stratified. As shown in Fig. 3.3 (d), the entire fire room is full of hot gases where the volume of lower layer is zero.

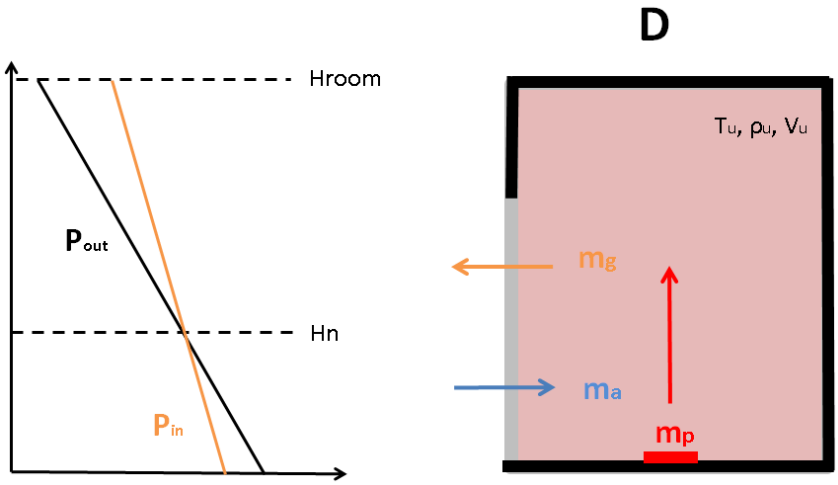

Fig. 3.3 (d) Single room fire at stage D

To summarize this section, these four stages describe the smoke filling process of a one-

compartment fire where there is one vent directly linked to the ambient air. The pressure profile is relatively simple since the ambient pressure is considered constant with only hydrostatic pressure drop. Following section will introduce the cases with multiple compartments.

Multi-compartment and virtual fire

Fig. 3.4 (a) is an example of a two-room fire model illustrating the hot and cold gases flow through vertical vents (i.e., doors and windows). Similar to a one-room case, each room is divided into two layers based on zone model assumptions. The smoke filling process of the fire room is a function of $\dot{m}_p$, $\dot{m}_g$ and $\dot{m}_a$ which is the same as the previous one-room case. For the connected non-fire room, the smoke filling process is estimated by converting the hot gases flow rate, $\dot{m}_g$, to an equivalent virtual fire $\dot{m}'_p$. So the entrained cold air in the non-fire rooms from the hot gas flow can also be determined using plume equations. Detailed formulations of the virtual plume are included in the following section with Eq. (3.26).

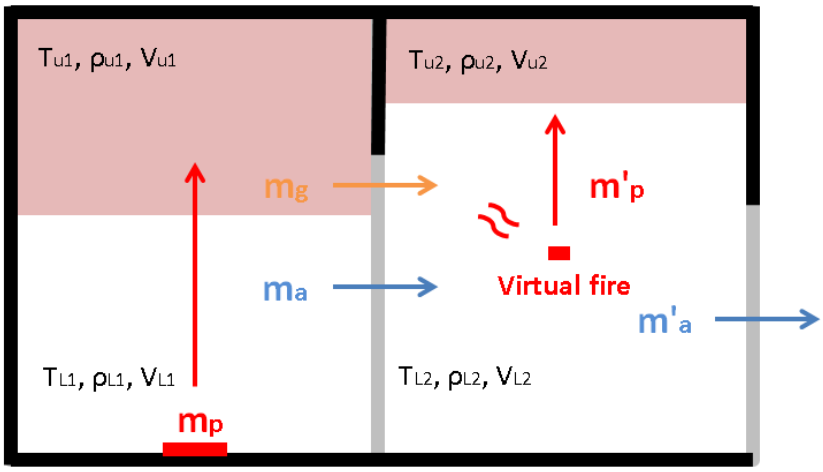

Fig. 3.4 (a) Door flow pattern in multi-room fire (Hd_2<doorH)

As the fire grows and more smoke gets into the smoke layer in the fire room, a neutral plane may exist similar to stage C in a one-room fire. The vent flow pattern can be more complicated than one-room case as show in Fig. 3.4 (b) but still follows the same rule.

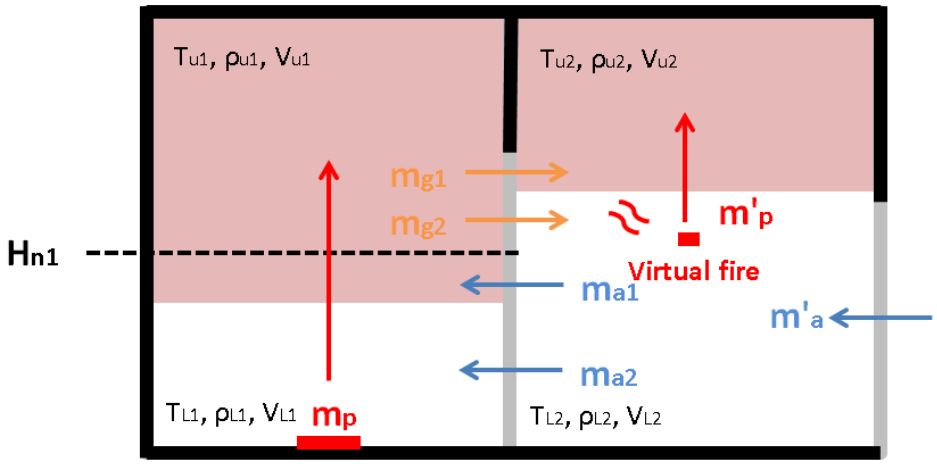

Fig. 3.4 (b) Door flow pattern in multi-room fire (Hd_2>doorH)

In order to determine the flow rate at door and estimate the model states of each room, it is formulated as following:

The pressure of a zone is determined by ideal gas law

$$P = \rho_i R T_i \tag{3.1}$$

where the background pressure of the upper layer and lower layer in the same compartment are assumed to be identical. And ρ is density of zone air, R is gas constant and T is zone air temperature. Subscription *i* represents the location of the layer.

Density

$$\rho_i = \frac{m_i}{V_i} \tag{3.2}$$

Internal energy

$$E_i = C_v m_i T_i \tag{3.3}$$

where the mass change over time of the upper layer, $\dot{m}_U$, is the sum of the total mass flow through the upper layer boundary which can be expressed as

$$\frac{dm_U}{dt} = \dot{m}_U = \dot{m}_p + \dot{m}_g \tag{3.4}$$

Since the control volume of each room is constant

$$\mathrm{V} = V_U + V_L \tag{3.5}$$

Next step is to apply energy conservation to a layer which is based on the thermodynamic first law.

$$\frac{dE_i}{dt} + P\frac{dV_i}{dt} = \dot{q}_i \tag{3.6}$$

where $\dot{q}_i$ is the rate of total energy gain of a layer including the rate of heat gain and enthalpy gain through the boundaries.

$$\dot{q}_U = \dot{Q}_c + C_p\dot{m}_p T_L + \dot{Q}_{g\,rad} - \dot{Q}_{cU} \tag{3.7}$$

and

$$\dot{q}_L = -C_p\dot{m}_p T_L - C_p\dot{m}_a T_L + \dot{Q}_{cL} \tag{3.8}$$

Summing up Eq. (3.6) for upper and lower layer

$$(\frac{dE_U}{dt} + \frac{dE_L}{dt}) + P(\frac{dV_U}{dt} + \frac{dV_L}{dt}) = \dot{q}_U + \dot{q}_L \tag{3.9}$$

where

$$\frac{dE_U}{dt} + \frac{dE_L}{dt} = \frac{d(c_v m_U T_U)}{dt} + \frac{d(c_v m_L T_L)}{dt} = \frac{c_v}{R}[\frac{d(PV_U)}{dt} + \frac{d(PV_L)}{dt}] \tag{3.10}$$

From Eq. (3.5), the total volume of upper and lower layer is constant so

$$\frac{dV_U}{dt} + \frac{dV_L}{dt} = 0 \tag{3.11}$$

by substituting Eq. (3.10) and (3.11) into Eq. (3.9).

Then, the differential equation for pressure is obtained

$$\frac{dP}{dt} = \frac{\gamma - 1}{V}(\dot{q}_U + \dot{q}_L) \tag{3.12}$$

At this point, it can be observed that the pressure change over time is a function of total energy flux entering and leaving the compartment where the mass flow rate from lower layer to upper

layer is irrelevant.

Differential equation for upper layer volume

$$\frac{dV_U}{dt} = \frac{1}{P\gamma}\left[(\gamma - 1)\dot{q}_U - V_U\frac{dP}{dt}\right] \tag{3.13}$$

where the room pressure P is the sum of ambient pressure P_{amb} and the pressure perturbation ΔP.

$$\mathrm{P} = P_{amb} + \Delta P = P_{amb} + \frac{dP}{dt}\Delta t \tag{3.14}$$

and the rate of temperature and density change for the upper zone can be determined by

$$\frac{dT_U}{dt} = \frac{1}{c_p\rho_U V_U}\left[(\dot{q}_U - c_p\dot{m}_U T_U) + V_U\frac{dP}{dt}\right] \tag{3.15}$$

and

$$\frac{d\rho_U}{dt} = -\frac{1}{c_p T_U V_U}\left[(\dot{q}_U - c_p\dot{m}_U T_U) - \frac{V_U}{\gamma - 1}\frac{dP}{dt}\right] \tag{3.16}$$

Sub-models

The Heskestad Plume

In order to determine the plume mass flow rate, $\dot{m}_p$, in Eq. (3.7) and (3.8), this model applies empirical correlations proposed by Heskestad (1984) which are a function of fire area, heat release rate, convective ratio and smoke travel distance. Comparing to other plume models, the Heskestad plume takes into account fire area and also assumes the fire as a virtual point source which makes it easier to calculate radiant heat transfer. As illustrated by Fig. 3.5, instead of directly using the fire area to calculate plume flow rate, Heskestad introduces a virtual origin point which can convert the plume to a cone shape as an ideal plume. The distance between actual fire source and the virtual origin, z_0, can be determined by

$$z_0 = 0.083\dot{Q}^{2/5} - 1.02D \tag{3.17}$$

where $\dot{Q}$ is the total heat release rate of the fire source (kW) and D is the diameter of the fire area (m).

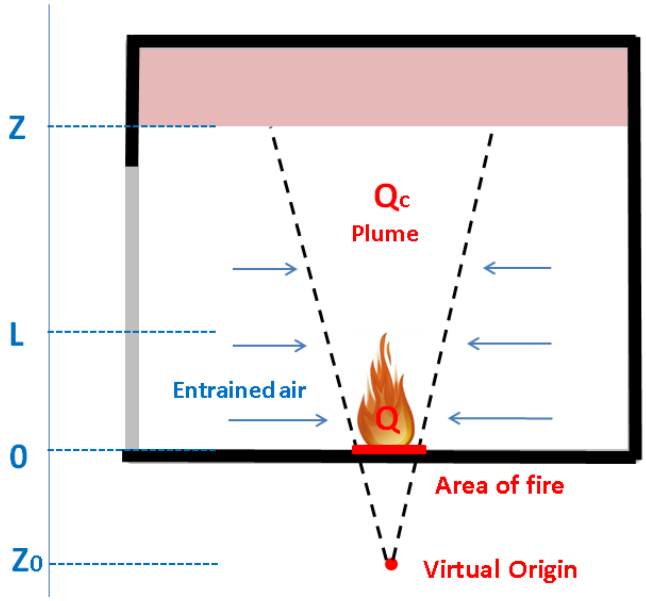

Fig. 3.5 Heskestad's plume model

Then, the average flame height is given by

$$\mathrm{L} = 0.235Q^{2/5} - 1.02D \tag{3.18}$$

And the plume mass flow rate at height z can be expressed as

$$\dot{m}_p = 0.071\dot{Q}_c^{1/3}(z - z_0)^{5/3} + 1.92 \cdot 10^{-3}\dot{Q}_c \quad for \quad z > L \tag{3.19}$$

and

$$\dot{m}_p = 0.0056\dot{Q}_c\frac{z}{L} \quad for \quad z < L \tag{3.20}$$

where $\dot{Q}_c$ is the convective proportion of the total heat release rate $\dot{Q}$ and it usually ranges between 60% to 80% for most fire models.

Orifice equation for vent flow rate

Another set of important variables in the differential equations are the flow rate through the vents

denoted $\dot{m}_g$ and $\dot{m}_a$, which are used to calculate the total energy flux through the boundary of a layer in Eq (3.7) and Eq (3.8). To obtain the flow rate, the orifice equation is applied where the velocity at a given height z at the opening can be presented as

$$\mathrm{v(z)} = C_d \sqrt{\frac{2\Delta P(z)}{\rho}} \tag{3.21}$$

where C_d is the flow coefficient and the mass flow rate is determined by

$$\dot{\mathrm{m}} = \rho v A = \rho v w z \tag{3.22}$$

where w is the width of the opening.

By substituting velocity v with Eq (3.21) and then integrate the equation along the height from bottom to top of an opening, Eq (3.22) becomes

$$\dot{m}_{vent} = \int_b^t \rho v(z) w dz \tag{3.23}$$

For a linear pressure profile over a given vertical distance, the equation can be rewritten as

$$\dot{m}_{vent} = \int_b^t C_d \sqrt{2\Delta P(z)\rho} w dz = \frac{2}{3} C_d A_{vent} \sqrt{2\rho} \left(\frac{P_t + \sqrt{P_t P_b} + P_b}{\sqrt{P_t} + \sqrt{P_b}} \right) \tag{3.24}$$

where P_t and P_b are the absolute pressure differences at the top and bottom of the opening respectively. But the pressure profile over an opening usually has more than one interception point, as shown in Fig. 3.4, where the calculations of the flow rates need to be divided into multiple sections.

Equivalent fire plume for non-fire room

The previous section mentioned the smoke filling process of a non-fire room is based on an equivalent fire plume where the heat release rate is determined by the hot gases flow from the fire room and can be given by

$$\dot{Q}_{eq} = c_p(T_{u1} - T_{u2})\dot{m}_g \tag{3.25}$$

and the height of the equivalent virtual plume can be expressed as

$$z_{p,eq} = \frac{(H_{d1} - H_{d2})}{\dot{Q}_{eq}^{2/5}} + v_p \tag{3.26}$$

where H_{d1} and H_{d2} are the smoke layer height of room one and room two respectively and the virtual point source, v_p, can be determined by the following equations:

$$v_p = \left(\frac{8.1\dot{m}_p}{\dot{Q}_{eq}}\right)^{0.528} \quad \text{for} \quad 0 < \left(\frac{\dot{m}_p}{\dot{Q}_{eq}}\right) < 0.0061 \tag{3.27}$$

$$v_p = \left(\frac{38.5\dot{m}_p}{\dot{Q}_{eq}}\right)^{1.1001} \quad \text{for} \quad 0.0061 < \left(\frac{\dot{m}_p}{\dot{Q}_{eq}}\right) < 0.026 \tag{3.28}$$

$$v_p = \left(\frac{90.9\dot{m}_p}{\dot{Q}_{eq}}\right)^{1.76} \quad \text{for} \quad 0.026 < \left(\frac{\dot{m}_p}{\dot{Q}_{eq}}\right) \tag{3.29}$$

Wall heat transfer mode

(1) Convection heat transfer:

The convection heat transfer coefficient of a zone is based on an equivalent value by combing convection heat transfer coefficients of the ceiling and wall as illustrated by Fig. 3.6.

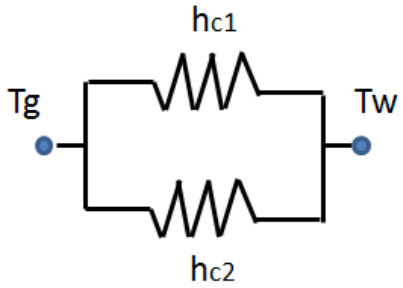

Fig. 3.6 Equivalent convective heat transfer coefficient of a zone

Based on the ratio of the area, the convective heat transfer coefficient can be determined

$$h_c = \frac{A_{ceiling}}{A_{total}} h_{c,c} + \frac{A_{wall}}{A_{total}} h_{c,w} \tag{3.30}$$

To calculate the heat transfer between the gas layer and the compartment surfaces including ceiling, walls and floor, three different types of heat transfer models need to be taken into account: convection, radiation and conduction. Fig. 3.7 shows an example of the heat transfer occurring at the wall surface where T_g is gas temperature, T_{wu} is wall temperature and T_{out} is exterior surface temperature.

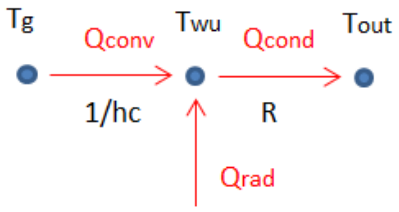

Fig. 3.7 Heat balance at wall surface

(2) Radiation heat transfer

Radiation heat accounts for 20% to 40% of the total fire source heat release rate. So the radiation model is also an important factor to the model accuracy especially for the fire room. In this model, the fire is assumed to be a point source located in the center of the total flame height which is L/2 where L can be obtained from Eq. (3.18). First consider the proportion of radiation heat entering the upper layer, $\dot{Q}_{total,rad}$.

$$\dot{Q}_{total,rad} = F_{OA}\varepsilon\sigma({T_g}^4 - {T_{wu}}^4)\mathrm{A} \tag{3.31}$$

where F_{OA} is the view factor of the point fire source to the destination compartment surface, ε is the emissivity of the surface material and σ is the Stefan-Boltzmann constant. T_g and T_{wu} are the temperature of upper layer gases and wall surfaces respectively. A is the cross section area at the smoke layer height which is usually the same as ceiling area.

To calculate view factor F_{OA} for relatively more complicated geometries than a rectangular plane, the surface can be divided into multiple smaller rectangles and the view factor is approximated by the sum of all small proportions similar to the example shown in Fig. 3.8.

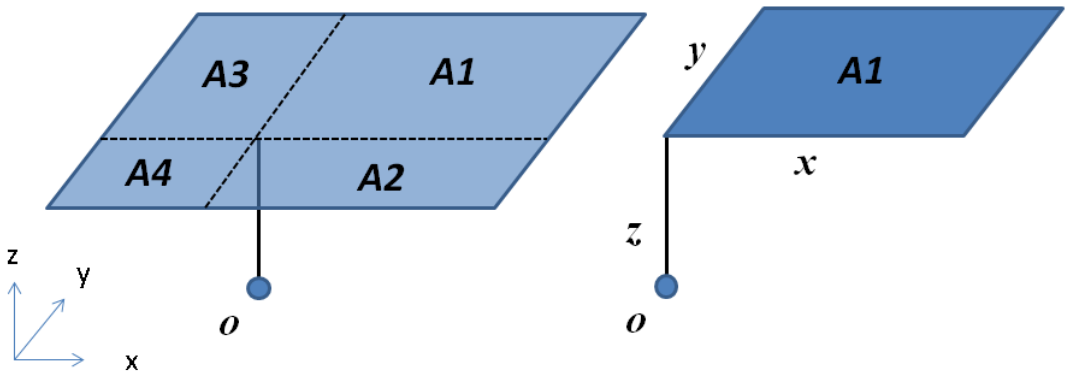

Fig. 3.8 View factor of a point to a rectangular surface

Consider a point O and a rectangular surface A, the view factor can be

$$\mathrm{F}_{OA} = F_{O1} + F_{O2} + F_{O3} + F_{O4} \tag{3.32}$$

By applying following equation, the view factor for each segment can be determined

$$\mathrm{F}_{O1} = \frac{1}{4\pi}\sin^{-1}\left[\frac{1}{\sqrt{(X^2+1)(Y^2+1)}}\right] \tag{3.33}$$

where $\mathrm{X} = \mathrm{z/x}$ and $\mathrm{Y} = \mathrm{z/y}$

The same method can also be applied to compute wall and floor view factors while the orientations of the surface should also be considered to get correct X and Y.

Before the radiation heat flux reaching the wall surface, a certain percentage of the radiation heat is absorbed by the upper layer gases, denoted $\dot{Q}_{g,rad}$, which is a part of total heat flux, $\dot{q}_U$, in Eq (3.7) and can be expressed as

$$\dot{Q}_{g,rad} = \dot{Q}_{total,rad} \cdot \alpha_{gas} \tag{3.34}$$

where α_{gas} is the absorptance of the upper layer gases.

In order to reduce the computation time, the compartment surfaces are assumed to be blackbody

where the reflectance is assumed zero.

(3) Transient heat conduction through walls

After obtaining the convection and radiation heat flux at the compartment surfaces, the heat conduction can also be computed by applying energy balance at the compartment surface as shown by Fig 3.7. For the material with small heat capacity, the thermal storage within the wall section can be neglected since it can be considered as thermal penetrated in early stage of fire. So the calculation can be very easy since the temperature inside the wall is assumed uniform. But for a thick wall where the temperature gradient inside the wall is significant, one must applies a transient heat conduction model by dividing the wall into small control volumes using Fourier's Law.

(4) Wall surface

The compartment surface temperature is determined by steady state one-dimensional heat transfer. But for the surfaces with high heat capacity, it is determined by transient heat transfer by dividing the entire wall section into *n* control volumes. So the temperature for each control volume is updated for each time step. For updating the surface temperature T_w from previous time I, it can be expressed by

$$T_w^{i+1} = \left(1 - 2\tau - 2\tau\frac{h\Delta L}{k}\right)T_w^i + 2\tau T_1^i + 2\tau\frac{h\Delta L}{k}T_{amb} + \tau\frac{\dot{q}_w^{-i}\Delta L}{k} \tag{3.35}$$

where

$$\tau = \frac{\alpha_w \Delta t}{\Delta L^2} \tag{3.36}$$

And L is the thickness of the wall (m), ΔL=L/n, k is thermal conductivity of the material (W/mK), $\dot{q}_w$ is the total heat flux to the wall surface including convective and radiant heat transfer and α_w is the thermal diffusivity (m^2/s)

After surface temperature is obtained, the temperature of each control volume inside the wall can be calculated by

$$T_{j-1}^{i} - 2T_{j+1}^{i} + T_{j+1}^{i} + \frac{\dot{q}_{j}^{-i}\Delta L^{2}}{k} = \frac{(T_{j}^{i+1} - T_{j}^{i})}{\tau} \tag{3.36}$$

where j is the index of the control volume and T_0 is the wall surface temperature T_w.

Solving smoke transport problem

The zone model presented in this thesis is based on an explicit method where the model states at a later time are calculated from the model states at the current time. As shown in Fig. 3.9, the model is initialized using ambient conditions except the upper layer require a small initial volume to avoid division-by-zero error. At t = 0, the air flow rate through the door is assumed zero. The pressure increment is first calculated by energy balance equation and used as initial value at t = 1. When the pressure is updated, the mass flow at the door can be obtained so the gradients of volume, temperature and density can be determined. At t = 2, when the temperature of the upper layer start increasing, the temperatures at the compartment surfaces start updating. The model is programmed using Java 1.7 and the detailed source codes are presented in Appendix.

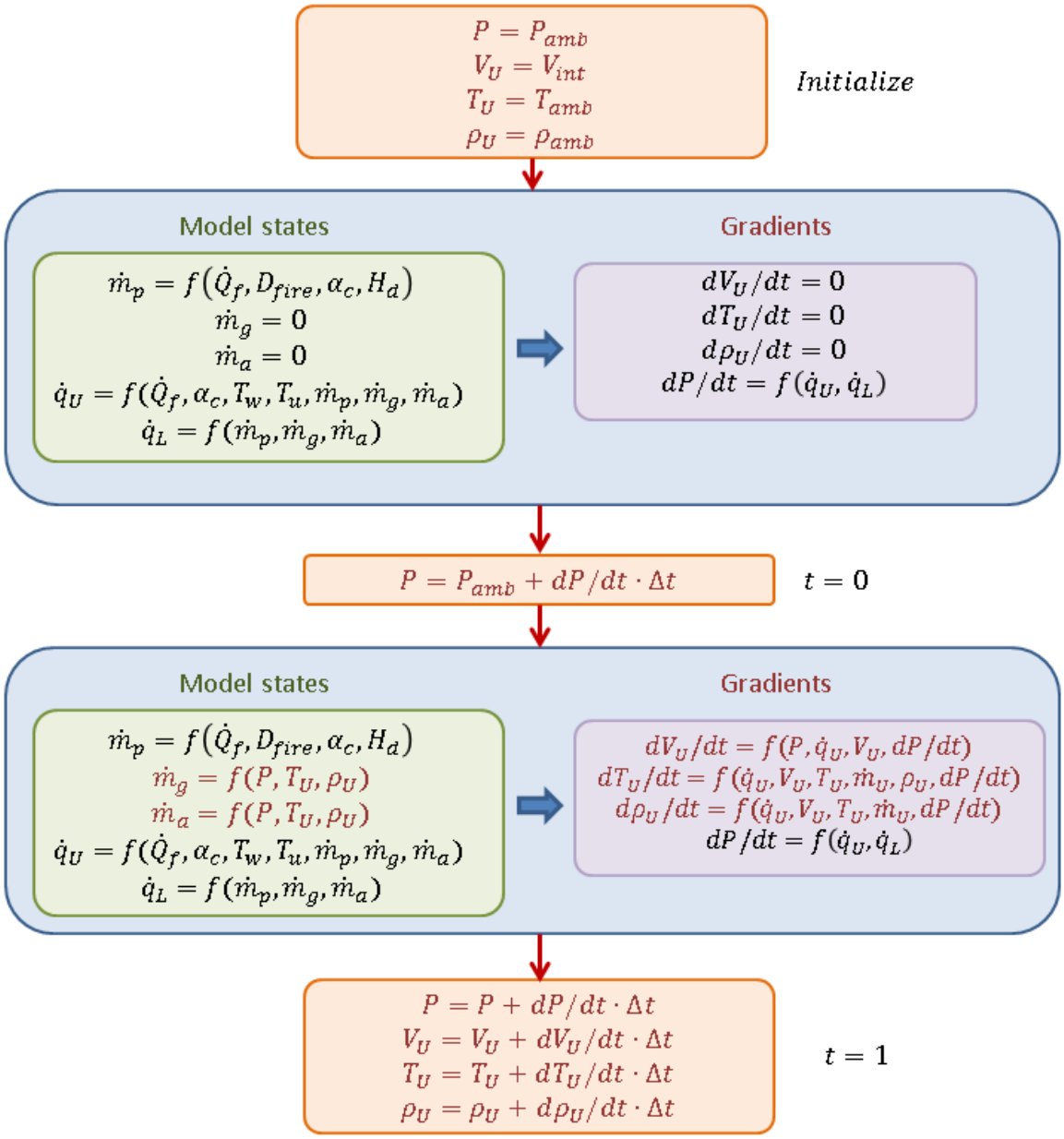

Fig. 3.9 Flowchart of zone model numerical operations

3.1.2 Ensemble Kalman filter (EnKF)

The previous chapter briefly introduced the background information about the EnKF. This chapter introduces the formulation of the EnKF in detail. In general, the numerical operations of the EnKF can be divided into two steps as shown in Fig. 3.1:

(1) Forecasting step: It is assumed at time step k, there are q numbers of parallel ensemble

members for the estimation of the model states, x_k^f, by using normally-distributed sampling errors. Consider a discrete nonlinear stochastic model

$$x_k^f = \mathrm{f}(x_{k-1}, \Phi_{k-1}) + w_{k-1} \tag{3.37}$$

where Φ_{k-1} is the control vector and w_{k-1} is a zero mean random white noise at time step *k-1*. The measurements corresponding to the model state can be expressed as

$$y_k = \mathbf{H}x_k + v_k \tag{3.38}$$

where the matrix **H** relates the model state *x* to the measurement *y* and *v* is the observation noise. If *x* and *y* are presenting the same quantity, **H** can be an identity matrix I.

Assume at time step *k*, there are *q* numbers of ensembles that predict models states.

$$\mathbf{X}_k^f = [x_k^{f1}, x_k^{f2} \ldots, x_k^{fq}] \tag{3.39}$$

(2) Analysis step: The error covariance, or the expected error of the predicted model states at analysis points and observation points, can be determined by the ensemble members from Eq. (3.39).

$$\mathbf{P}_k^f \mathbf{H}^T = \frac{1}{q}\sum_{i=1}^{q}(x_k^{fi} - x_k^t)(\mathbf{H}x_k^{fi} - \mathbf{H}x_k^t)^T \tag{3.40}$$

while true state, x_k^t, is unknown, we use the mean of the ensemble members to approximate the true state.

$$x_k^t \approx \overline{x_k^f} = \frac{1}{q}\sum_{i=1}^{q} x_k^{fi} \tag{3.41}$$

then Eq. (3.40) becomes

$$\mathbf{P}_k^f H^T = \frac{1}{q-1}\sum_{i=1}^{q}(x_k^{fi} - \overline{x_k^f})(\mathbf{H}x_k^{fi} - \mathbf{H}\overline{x_k^f})^T \tag{3.42}$$

Please note that in order to make the estimation unbiased, a factor of *1/(q-1)* is applied instead of

1/q. Then, the Kalman gain can be determined by using the traditional Kalman Filter equation where an optimum value, x_k^a can also be determined.

$\mathbf{P}_k\mathbf{H}^T$ in Eq. (3.42) can be directly obtained from ensemble members and the $\mathbf{HP}_k\mathbf{H}^T$ is a global matrix for all model states to calculate the covariance between forecast values at the observation points. It can be noted that for all the *q* ensemble members, the Kalman gain, *K*, is always the same value for all mirrored model states instead of an individual value for each ensemble member, which significantly reduces the computation cost. In addition, the error covariance matrix does not need to be saved for the next analysis cycle, which also improves the model efficiency by releasing memory space for later use.

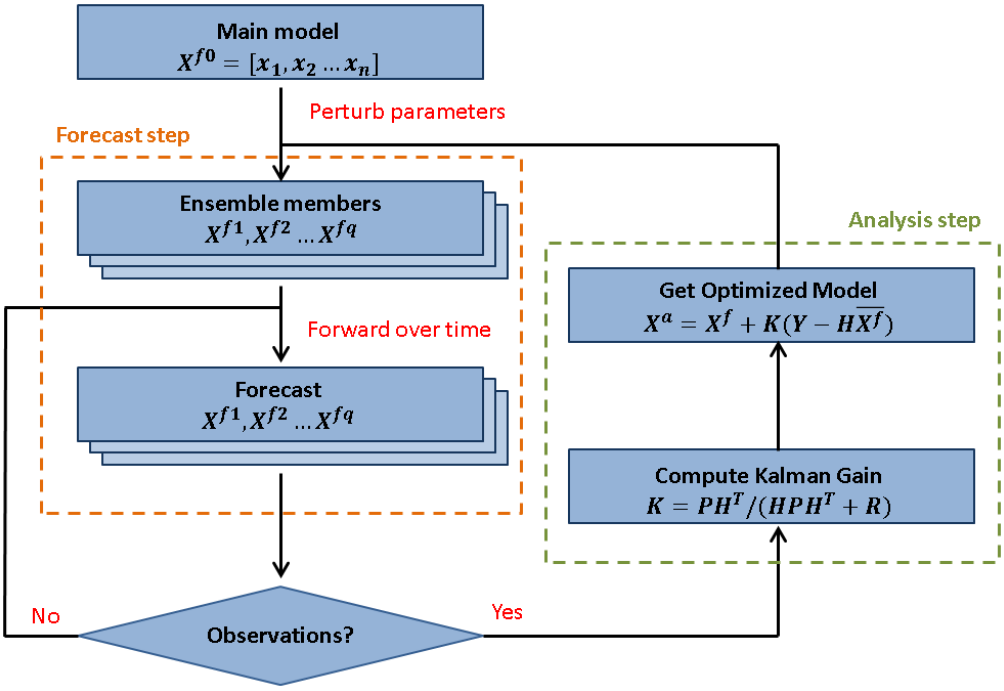

Fig. 3.10 Flowchart of EnKF forecasting and analysis steps

After Kalman gain is obtained for this time step, analysis can be done to update all model states even for the model states without direct measurements. For the simulation time step without any observation available, the prediction of model states is based on the average of all predicted ensemble members. Meanwhile, one of the common limitations of initial EnKF applications is

that in each analysis cycle, the Kalman gain is applied to all model nodes even for those less correlated so spurious correlations are caused as proven by Evensen (2009). For higher dimensional models (models with higher number of parameters), it is usually suggested to apply a distant-dependent Schur-product when using Kalman Gain to update model states (Hamill and Whitaker, 2001). Detailed discussions about formulating an EnKF model to forecast indoor environment is presented in Chapter 7.

References

Evensen, Geir. "Sequential data assimilation with a nonlinear quasi-geostrophic model using Monte Carlo methods to forecast error statistics." *Journal of Geophysical Research: Oceans (1978–2012)* 99, no. C5 (1994): 10143-10162.

Fowkes, N. D. "A mechanistic model of the 1973 and 1974 bedroom test fires." *A study of room fire development: The second full-scale bedroom fire test of the home fire project (July 24, 1974)* 2 (1975): 8-50.

Tanaka, Takeyoshi. "A model of multiroom fire spread." *Fire Science and Technology* 3, no. 2 (1983): 105-121.

Heskestad, Gunnar. "Engineering relations for fire plumes." *Fire Safety Journal*7, no. 1 (1984): 25-32.

McCaffrey, B. “. "Momentum implications for buoyant diffusion flames."Combustion and Flame 52 (1983): 149-167.

Zukoski, E. E. "Mass flux in fire plumes." In *Fire Safety Science-Proceedings of the Fourth International Symposium, IAFSS*, p. 13. 1994.

Hamill, Thomas M., Jeffrey S. Whitaker, and Chris Snyder. "Distance-dependent filtering of background error covariance estimates in an ensemble Kalman filter." *Monthly Weather Review* 129, no. 11 (2001): 2776-2790.

Evensen, Geir. "The ensemble Kalman filter for combined state and parameter estimation." *Control Systems, IEEE* 29, no. 3 (2009): 83-104.

Chapter 4 Forecasting Simulations of Indoor Environment using Data Assimilation via an Ensemble Kalman Filter[1]

ABSTRACT

Data assimilation is widely used in weather forecasting and other complex forecasting problems such as hydrology, meteorology, and fire dynamics. Among various data assimilation methods, the Ensemble Kalman Filter (EnKF) is one of the best solutions to large-scale nonlinear problems as the computational cost is relatively less intense than other forecasting methods. In this chapter, a new application of EnKF to forecast indoor contaminant concentrations is presented. The first part of the paper introduces the fundamental theories of data assimilation. The second part is a case study of forecasting the concentrations of a tracer gas in a multi-zone manufactured house by using a mass balance model with an EnKF. The benefits of EnKF and several important parameters for EnKF were discussed including numbers of ensemble members and observations, time step of observations, and forecasting lead time. The EnKF method presented is one of the first studies applied to the indoor environment field. It was shown that by using EnKF, the predictability of the simple indoor air model for the multi-zone space was improved significantly.

Highlights:

▪ The EnKF is applied to forecast indoor environment.

▪ The optimum number of ensemble members is approximately 70 to 80.

▪ Both number of observations and time step of observations affect the EnKF performance.

▪ Predictability of the indoor model is significantly improved with EnKF implementation.

1. The contents of this chapter are published in (Lin, Cheng-Chun, and Liangzhu Leon Wang“. "Forecasting simulations of indoor environment using data assimilation via an Ensemble Kalman Filter." *Building and Environment* 64 (2013): 169-176. The contents are slightly updated.

4.1 Introduction

4.1.1 Forecasting contaminant transport

The forecasting of indoor environment is of great interests due to its close relationship to occupant's safety (Koo et al. 2010), thermal comfort (Freire et al. 2008), and energy efficiency (Oldewurtel et al. 2012 and Tudoroiu et al. 2008), for which an accurate prediction of important parameters is often needed such as temperature, relative humidity and contaminant concentration. Forecasting these indoor air properties, especially solving contaminant transport problem in a dynamic environment, is a difficult task since the physical states of the building environment could change rapidly over time (Liu and Zhai 2009). Under such uncontrollable factors as ambient temperature, air velocity, humidity, and occupant loads, the contaminant estimation is hard to achieve by conventional methods using steady state analysis of constant model parameters. In addition, sudden release of contaminant, opening doors and windows, change of occupant behavior and the use of electric appliances are a few common examples that may further increase the difficulty of solving the forecasting problem. By using any numerical model to predict future indoor air contaminants, these uncertain events will cause the predicted physical states to depart from reality as the model evolves forward over time. Previous studies showed a few different ways of indoor environment forecasting. Federspiel (1997) utilized a method originating from the optimization theory, so-called the Kalman Filter, to estimate the strength of gas sources in buildings successfully. But the model has some restrictions when it applies to multi-zone problems since source strength and air flow rate must be known a priori. Kemajou (2012) presented that indoor air temperature and relative humidity could be quickly predicted by using artificial neural network (ANN). The potential problem of using a black-box type of methods like ANN is that the training of models still relies on trial and error to determine

an optimum model structure while the training parameters usually cannot be applied to other buildings. Another limitation is its inefficiency for each new case, in which huge amount of data is required for the training. Sreedharan (2006) introduced another model of forecasting simulation using Bayesian Monte Carlo method to quickly analyze measurements from multiple indoor air sensors. This system can monitor real-time indoor environment to help protect occupants by locating the release source of a high-risk pollutant. Follow-up studies (Gadgil et al. 2008 and Sreedharan 2011) focus more on using heterogeneous sensor systems such as monitoring door position and mechanic ventilation operating status. Extensive reviews of other methods for locating indoor air contaminants can be found in the article conducted by Liu and Zhai (2007). Most of these previous studies focus on locating contaminant source instead of predicting dynamic future evolvement of concentrations in a multi-zone building.

4.1.2 Data assimilation

The major task of forecasting simulations is to predict future states of physical phenomenon with a certain lead time and accuracy. In order to find optimal state variables, data assimilation provides different algorithms for parameter estimation while taking into account uncertainties of measurements and numerical predictions.

In 1960, a pioneer research of data assimilation theory has been established by R. E. Kalman, the Kalman Filter, which provides a recursive solution to find a best possible estimation of the true state. Instead of finding an optimal estimation for one value as best linear unbiased estimation (BLUE), the Kalman Filter can be applied to a dynamic model that evolves over time (Welch and Bishop 2006 and van Velzen 2010). In order to solve different types of nonlinear problems, a few Kalman Filter variants have been proposed. In the Extended Kalman Filter (XKF), the nonlinear models are linearized by using partial derivatives which is similar to a Taylor series expansion. It

has been proven that XKF is effective in many applications but its weakness is the error probability density is not fully considered in the linearization. Although the analysis scheme of XKF is similar to traditional Kalman Filter, the computational requirements of XKF are drastically increased by additional numerical operations, such as linearization. Another mainstream of the data assimilation theories for nonlinear problems is four-dimensional variational assimilation (4D-Var) and is widely used to weather forecasting (Courtier 2007). Like its counterpart, three-dimensional variational assimilation (3D-Var), 4D-Var is based on minimizing a cost function. In order to calculate the gradient of the cost function for minimization, it is required to manipulate large matrices, which makes 4D-Var computationally intensive. Evensen (1994) proposed a more affordable method, Ensemble Kalman Filter, to determine error statistics by using the Monte Carlo method. The method reduces computational requirement of XKF by using ensemble members, which are similar to the samplings in other Monte Carlo methods, to avoid direct calculation and storage of the evolution of the large error covariance matrices. Each ensemble member in EnKF can be calculated separately so it is especially suitable for parallel computing and solving large scale problems. This method has been widely used in weather forecasting, hydrology and fire dynamics predictions (van Velzen 2010 and Jahn 2010). No previous studies have been reported to use EnKF for indoor environment simulations. Different from existent studies, the indoor air forecasting model with the EnKF is performed without determining source strength and location but instead depending on the accurate estimation of error statistics including uncertainties from both experiment and numerical model. Therefore the EnKF can perform faster prediction than other methods but relies on rapidly obtaining measurement data.

The objective of this paper is to explore the applications of EnKF to forecasting indoor air

environment and discuss the key parameters involved in the accuracy of EnKF for indoor environment forecasting. This paper applied an EnKF to a case study of forecasting the concentrations of a tracer gas in a multi-zone manufactured house by using a mass balance model. The benefits of EnKF and several important parameters for EnKF were discussed including numbers of ensemble members and observations, time step of observations, and forecasting lead time. The EnKF method presented is one of the first studies applying a weather forecasting model to indoor environment field. In this paper, all numerical operations relating to data assimilation are based on a generic toolbox for data assimilation, OpenDA (Verlaan et al. 2010), developed by Delft University of Technology, Netherland.

4.2 Methodology

The detailed explanations on data assimilation and the fundamental theories of EnKF can be found in many references (Kálmán 1960, Welch et al. 2006, Evensen 1994 and Verlaan et al. 2010) so they are not covered in this paper to avoid repetition. Instead of copying down the math of EnKF, this paper will focus on how the fundamental methodology of EnKF is applied to the indoor air modeling of a multi-zone manufactured house.

4.2.1 Multi-zone manufactured house

The experimental data for data assimilation come from a series of tracer gas measurements in a manufactured house conducted by National Institute of Standards and Technology (NIST) in 2007 (Nabinger and Persily 2008, Wang and Emmerich 2010). The house includes living room, family room, kitchen and three bedrooms as shown in Fig. 4.1. An attached garage was added after the measured data were collected so it was not included in this study. During the experiment, tracer gas, sulfur hexafluoride (SF_6), was injected about every six hours in the living room and the concentration of SF_6 was measured at various indoor locations for every ten

minutes by gas chromatography. The system is capable of measuring SF_6 concentration over a range of 3 to 300 ppb, with an uncertainty of about 5 % of the reading. In this study, bedroom 3 was excluded because its sampling line was moved to the outside for another research project. Please note that the measurement of each room starts from different time step as shown in Table 1.1. For example, the tracer gas concentration in the master bedroom was measured at t = 0, 10 min and so on, and bedroom 2 is measured at t = 1, 11 min etc. The average air change between indoors and outdoors was calculated based on the tracer gas decay method, which was about 0.1 to 0.4 air changes per hour (ACH). In this study, twelve hours measurement data are obtained from four different locations as observation while two injections are included. The first one is at the beginning of the experiment and the other one is about six hours after the first injection. The injection rate is intended to achieve an average initial gas concentration of around 120 ppb but is assumed to be unknown in the simulations. The instruments were calibrated regularly and believed to be accurate enough. 5% error is thus assigned to the observation errors accounting for the mentioned uncertainties. The uncertainties associated with the mixing conditions are considered in the numerical model in the following sections.

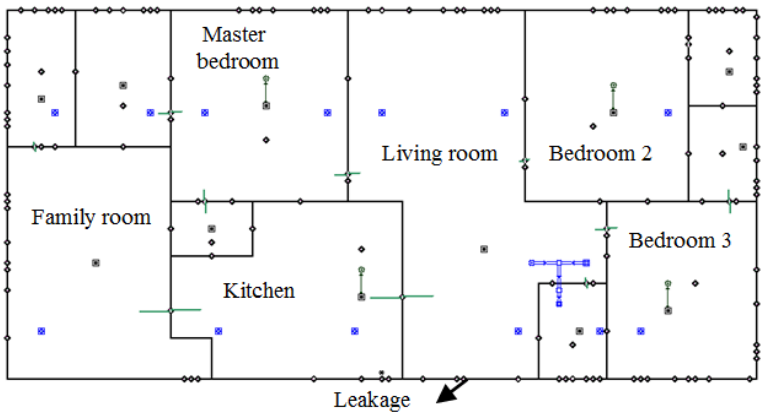

Fig. 4.1 CONTAM model of the manufacture house (Wang and Emmerich 2010).

Table 4.1 Summary description of the manufactured house and the tracer measurement.

Room	Master Bedroom	Bedroom 2	Living Room	Family Room	Kitchen
Volume (m^3)	35	28	80	50	40
Initial Concentration (ppb)	103	160	145	143	142
First Observation (min)	0	1	4	5	7

4.2.2 Tracer gas concentration model

The modeling of indoor environment here is to forecast the SF_6 concentrations in the different rooms of the house by a mass balance model of SF_6. The forecasting accuracy of the model is improved by combining with measured SF_6 concentrations following the algorithm of the EnKF. Based on the well-mixed assumption, which assumes the air property within a room/zone is well mixed without spatial variation, the mass balance for a contaminant in one room can be determined by

$$\frac{dC}{dt}(\rho_{in}V) = S_c - \sum \rho_{in} C Q_{outflow} + \sum \rho_{out} C_{out} Q_{inflow} \tag{4.1}$$

where V is the volume of the room, S_c is the contaminant source generation rate, ρ is the density of the room air and Q is the air volumetric flow rate. Subscripts in and out indicate the flow direction relative to each room. The contaminant concentration for each room at time k, C_k, can be discretized in time as

$$C_k = C_{k-1} + \frac{dC_{k-1}}{dt}\Delta t \tag{4.2}$$

where $\frac{dC_{k-1}}{dt}$ is evaluated by Eq. (4.1) and can be solved numerically by a method such as the Runge-Kutta method.

Eqs. (4.1) and (4.2) are applied to five zones including family room, master bedroom, kitchen, living room and bedroom 2. The airflow rates among the different rooms, Q, are calculated by using the multi-zone indoor air quality analysis software, CONTAM (Walton and Dols 2010), with hourly averaged weather conditions as inputs. The weather conditions were measured by a

local weather station at the house site. The detailed simulation results are shown in the results and discussions section.

4.2.3 Stochastic model of tracer gas concentration

Eq. (4.1) is a conventional deterministic model when the model parameters, either obtained numerically or experimentally, are without considering uncertainties. For complex problems and/or systems with high uncertainties, the analysis is commonly based on stochastic models to reflect the randomness or the probability distribution of the model variables. Therefore, Eq. (4.1) needs to be converted into a stochastic model by perturbing the model variables with an auto-regression model during the Monte Carlo sampling process of the EnkF (Thornber 1967). An example of setting up the uncertainties is that the calculated airflow rates in CONTAM are expected to have 10 % deviations from the hourly variations of the experiment day. The error from CONTAM simulation and the well-mixed assumption accounts for another 10 % deviation. The selection of these uncertainties should be evaluated under different conditions but currently is not the focus of this paper. Here we define these deviations as zero-mean, normally-distributed white noise. Based on the probability density of these deviations, the model parameters for each Monte Carlo sample, here so-called an ensemble member, are generated.

4.2.4 Combining numerical prediction and measurements by EnKF

By using the EnKF, the stochastic model is combined or so-called assimilated with the measurements in different rooms. In this study, the measurements from four rooms are used at current time step: the master bedroom, family room, kitchen and bedroom 2, in the data assimilation to forecast the concentrations in all rooms in the future, especially that of the living room, where no experimental data have been used. A data assimilation forecasting of a contaminant concentration at the time k for a room j, $C_{j,k}^{f}$, can be expressed by:

$$C_{j,k}^{f} = \mathrm{f}(C_{j,k-1}, \Phi_{j,k-1}) + w_{j,k-1} \tag{4.3}$$

where *f* means forecasting, *j* is the index of model nodes and *k* is the index of time; $\Phi_{j,k-1}$ is the control vector which represents perturbed airflow rates and $w_{j,k-1}$ is a zero mean random white noise accounts for simulation errors at time step *k-1*. The function *f* here refers to Eq. (4.2). When any observation is available, the true state of the living room concentration, $C_{L,k}^{t}$, is estimated by EnKF. For example, at $t = k$ min, the measurement is available in the master bedroom so the EnKF is able to work as follows. A vector of the predicted SF_6 concentration is generated by the ensemble members with a total number of q for each room, e.g. the concentration forecast of the master bedroom can be presented as

$$C_{MB,k}^{f} = [C_{MB,k}^{f1}, C_{MB.k}^{f2} \ldots, C_{MB,k}^{fq}] \tag{4.4}$$

The measurement in the master bedroom corresponding to the numerical forecast is expressed as

$$y_{MB,k} = \mathbf{H}C_{MB,k}^{f} + v_k \tag{4.5}$$

where the matrix **H** relates the model state $C_{MB,k}^{f}$ to the measurement $y_{MB,k}$ and v_k is the observation noise (accounts for 5 % measurement error in this case). If $C_{MB,k}$ and $y_{MB,k}$ represent the same physical quantity, *H* will be the identity matrix, *I*.

Then the forecast error covariance, or expected error of the model prediction, $P_{MB,k}^{f}$, can be approximated by the q ensemble members:

$$\mathbf{P}_{MB,k}^{f}\mathbf{H}^{T} = \frac{1}{q}\sum_{i=1}^{q}(C_{MB,k}^{fi} - C_{MB,k}^{t})(\mathbf{H}C_{MB,k}^{fi} - \mathbf{H}C_{MB,k}^{t})^{T} \tag{4.6}$$

since the true state, $C_{MB,k}^{t}$, is unknown, we use the mean of the ensemble members to approximate

$$C_{MB,k}^{t} \approx \overline{C_{MB,k}^{f}} = \frac{1}{q}\sum_{i=1}^{q} C_{MB,k}^{fi} \tag{4.7}$$

then Eq. (4.6) becomes

$$\mathbf{P}_{MB,k}^{f}\mathbf{H}^{T} = \frac{1}{q-1}\sum_{i=1}^{q}(C_{MB,k}^{fi} - \overline{C_{MB,k}^{f}})(\mathbf{H}C_{MB,k}^{fi} - \mathbf{H}\overline{C_{MB,k}^{f}})^{T} \tag{4.8}$$

Please note that in order to make the estimation unbiased, a factor of *1/(q-1)* is applied instead of *1/q* (Whitaker 2002). Then, the Kalman gain for the master bedroom, $K_{MB,K}$, can be determined by using the traditional Kalman Filter equation where an optimal master bedroom concentration,$C_{MB,k}^{a}$, is estimated as

$$C_{MB,k}^{a} = \overline{C_{MB,k}^{f}} + \mathbf{K}_{MB,k}(y_{MB,k} - \mathbf{H}\overline{C_{MB,k}^{f}}) \tag{4.9}$$

where the Kalman gain for each room at $t=k$, $\mathbf{K}_j$ can be estimated by

$$\mathbf{K}_{j,k} = \frac{\mathbf{P}_{j,k}\mathbf{H}^{T}}{\mathbf{H}\mathbf{P}_{MB,k}\mathbf{H}^{T} + \mathbf{R}} \tag{4.10}$$

where the denominator of Eq. (4.10) is a constant for all Kalman gains since the measurement is only available in master bedroom and R presents the expected measurement error (5% in this case). The numerator can be obtained without using any measurement by calculating the respective error covariance $P_{j,k}H^{T}$ for each room. $K_{MB,k} = K_{j,k}$ when $P_{j,k}$ is $P_{MB,k}$. After obtaining all five Kalman gains, the concentration can be updated for all five rooms even for those without measurements by Eq. (4.9). So the true state of the living room $C_{L,k}^{t}$ can be approximated by $C_{L,k}^{a}$ which combines results of numerical prediction and experimental measurements. For the simulation time step without any observation available, the prediction of model states is based on the average of all predicted ensemble members. Since the predicted model states are sequentially assimilated with the measurements, the error covariance matrix does not need to be saved for the

upcoming analysis cycle, which reduces the computational cost by releasing memory space for later use.

4.3 Results and discussions

4.3.1 CONTAM airflow rate simulations

Fig. 4.2 illustrates the transient airflow rates predicted from CONTAM simulations used in the forecasting simulation of SF_6 concentrations. The airflow rate between the indoor and exterior environment varies over time due to the change of weather condition while the interior airflow rate are relative constant. Table 4.2 shows the average airflow rate between two neighboring rooms. It can be observed that interior air exchange is generally much higher than the exterior. Therefore, the dynamic model (e.g. Eq. 4.2) is calculated with a one-minute time step ($\Delta t = 1$ minute) by assuming constant airflow rates for the interior air exchange and time-dependent airflows for the exterior exchange during the simulation. Like most existent indoor air forecasting model, the deterministic model use measurement data from the sensors directly as inputs where the uncertainties are not considered in this case.

Fig. 4.2 Examples of transient airflow rates from CONTAM outputs.

Table 4.2 Average airflow rates in the house (m^3/min).

From / To	Master Bedroom	Bedroom 2	Living Room	Family Room	Kitchen	Outdoor
Master Bedroom		N/A	9.70	N/A	0.0	0.0
Bedroom Two	N/A		7.70	N/A	N/A	0.0
Living Room	9.44	7.66		N/A	25.43	0.17
Family Room	0.0	N/A	N/A		26.36	0.14
Kitchen	0.01	N/A	24.79	26.59		0.09
Outdoor	0.04	0.02	0.04	0.0	0.0	

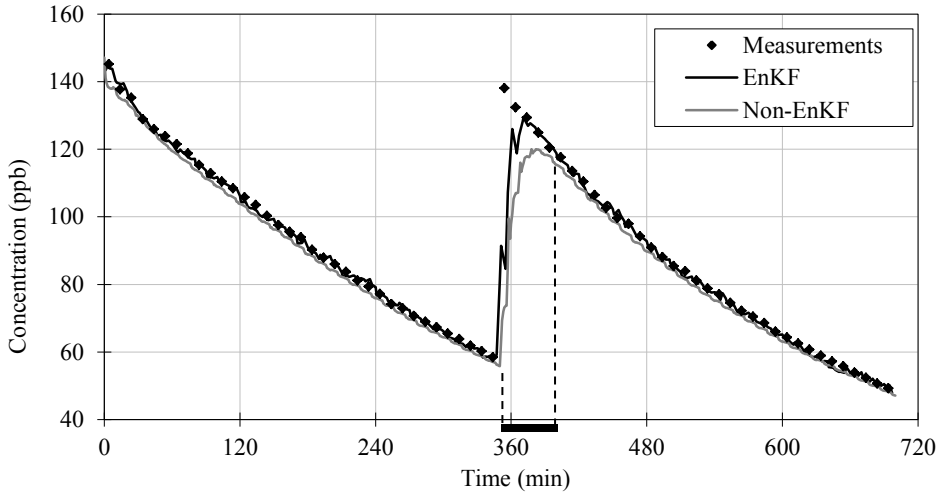

Fig. 4.3 Comparisons of deterministic sequential simulation and EnKF with the measured SF_6 in the living room.

4.3.2 Tracer gas forecasting with and without EnKF

To demonstrate the benefits of using EnKF, we first directly use the deterministic model of Eq. (4.2) to predict SF_6 concentration in the living room as a control group for comparison. In both cases, the measurements of all rooms except the living room at the previous time step are given as the inputs to predict the concentration at the current time by Eq. (4.2), and only the initial concentration is given in the living room. In Fig. 4.3, the deterministic (non-EnKF) model has shown good predictability when there is no sudden change in SF_6 concentration. But when the second SF_6 injection took place around the 350 minutes, the model will require about 30 minutes to correct the prediction in the living room as illustrated by the bold horizontal bar in Fig. 4.3, since there is no direct measurement available. The slow response of the non-EnKF model is due

to the reason that the measurement at one room is only used to update the model state for that room but its impact on other rooms is not taken into account since Kalman gain is not calculated. By implementing EnKF when one measurement is available, Kalman gains can be computed for all the modeled nodes. Therefore, one measurement can update the concentrations for all nodes even for those without measurements. The analyzed states are then used in the dynamic model as a new initial condition to compute new model states in the following time steps. When the next observation is available, the procedure is then repeated. As shown by the bold line in Fig. 4.3, the predictability improves significantly with the EnKF implementation near the time of the injection.

4.3.3 Discussion of key EnKF parameters

In this section, we will discuss how different key parameters affect the accuracy of the EnKF during the indoor environment modeling in the case study. These parameters include number of ensemble members, number of observations, observation time step, the effects of weather conditions, forecasting lead time and finally the predictability.

Number of ensemble members

During the forecasting, the model states are determined by the average of all ensemble members as shown by Eq. (4.7). Fig. 4.4 illustrates the predicted concentration of the living room from 70 ensemble members in grey lines and the black line is the average of all ensemble members when compared to the measurements (the black squares). Although a single ensemble member may vary significantly about the ensemble average, the average is very close to the experimental data, which indicates 70 ensemble members are appropriate to provide the accurate prediction in this case. From Eq. (4.8), the error statistics are estimated based on a finite size of ensemble members to approximate $q \rightarrow \infty$. For a simple model with low number of mesh grids or data points, q not

only affects the predictability but also determines the computational cost of the analysis. Table 4.3 shows that the simulation time increased with the number of ensemble numbers. Considering both accuracy and cost, 70 ensemble members seem to be the best choice for the modeled house. In general, it is recommended to have around 100 ensemble members in many EnKF applications since the results are not showing significant improvement by exceeding this number. In addition, the computational burden also increases drastically with the ensemble members (Evensen 2009). Thulin and Nævdal (2011) also suggested doing several EnKF runs in which each with less ensemble members. We also simulated the same house under different weather conditions, i.e. November and February in Fig. 4.5, and obtained consistent results. It shows the optimum numbers of ensemble members for both cases are very close (q = 70 and q = 80). Unfortunately, there is still no theoretical principles to determine an optimal ensemble number but it is recommended to start trial and error from q = 100. For all cases, the simulations only takes a few seconds, which shows the EnKF is very fast for this case.

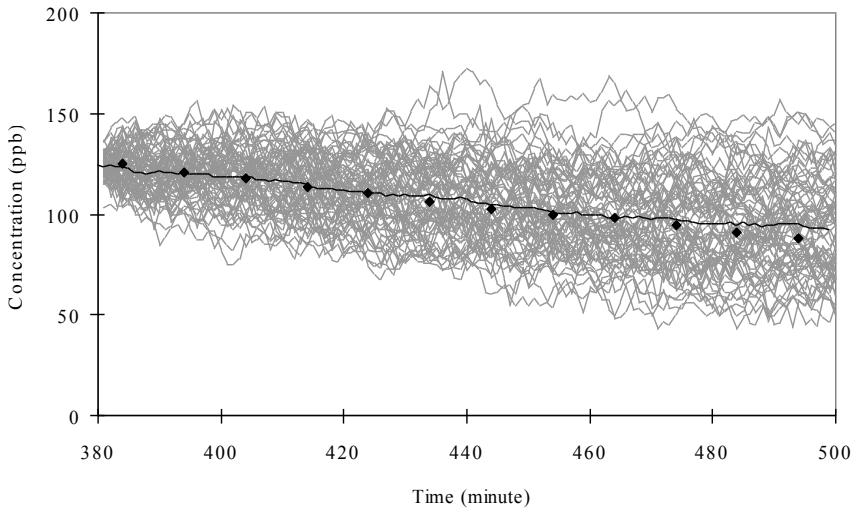

Fig. 4.4 EnKF prediction of the living room concentration by 70 ensemble members.

Table 4.3 Comparisons of root mean squared errors of different models

Case	1	2	3	4	5	6	7
Ensemble numbers	30	50	70	90	110	70	70
Observations nodes	4	4	4	4	4	3	2
CPU time (seconds)	4	7	10	14	18	11	7
RMSE living room SF_6 (ppb)	7.1	7.3	5.4	5.3	6.9	7.9	8.8

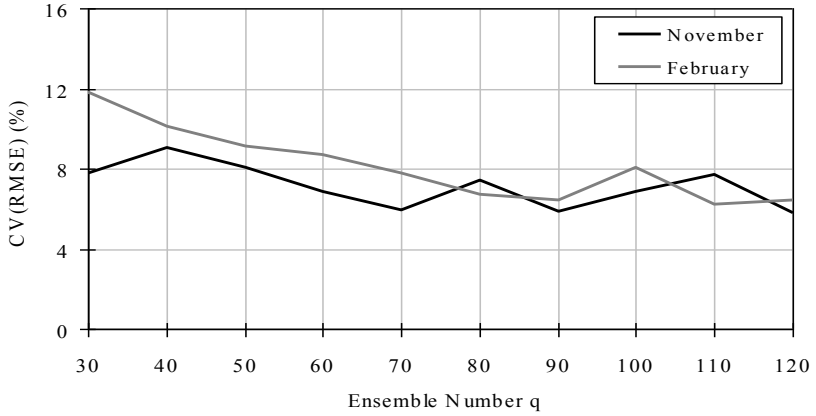

Fig. 4.5 Comparisons of the RMSE of the November and February cases (CV is the coefficient of variation. Defined as the RMSE divided by the mean).

Number of observations

The number of observations also plays a role in performance of EnKF. As shown by case 3, 6 and 7 in Table 4.3, the RMSE decreases when more observed nodes available for data assimilation for q = 70. It is not surprising because more data available for assimilation would improve the accuracy of the prediction. For a real-time indoor air monitor system, the problem is the optimal number of sensors and the best location to place in a multi-zone environment to achieve certain forecasting accuracy. Fig. 4.6 shows that when the observations were only provided for the kitchen and family room, the prediction in the living room seems still reasonable, of which the RMSE is 8.8 ppb as shown by case 7 in Table 4.3. More studies using other combinations of two observation nodes or even one node are beyond the scope of this paper but are indeed worth further investigations.

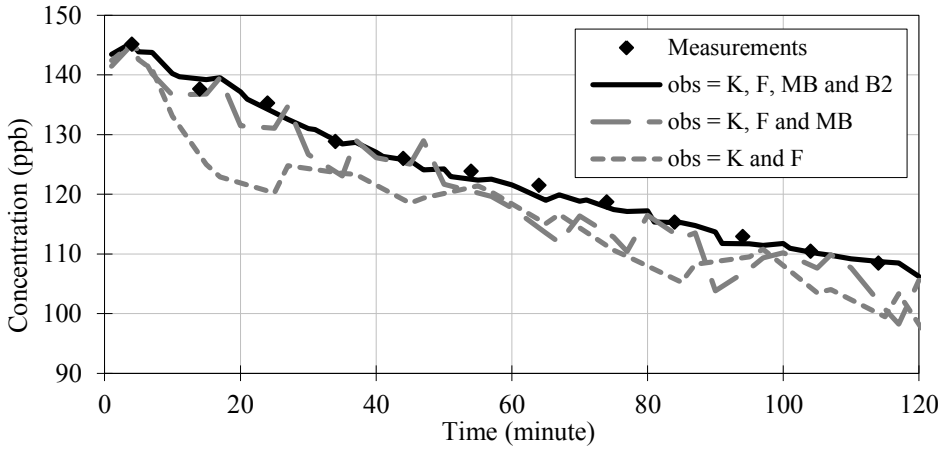

Fig. 4.6 Comparisons of the SF_6 prediction in the living room by different numbers of observations ("obs = K and F" means observation data are only provided for kitchen and family room).

To complete this section, Fig. 4.7 shows the posteriori estimations of SF_6 concentration in the master bedroom. Different from the forecasted data in Fig. 4.8, the posteriori estimations in Fig .4.7 are assimilated with local observation in the master bedroom so the results are very close to the measurements. The similar results are also found for kitchen, family room and bedroom 2.

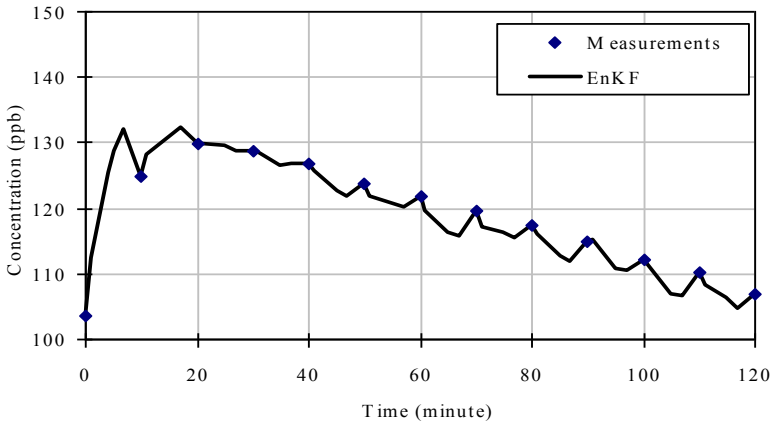

Fig. 4.7 Posteriori estimations of the SF_6 concentration in master bedroom.

Observation time step

Commercial off-the-shelf (COTS) sensors with desired resolution to analyze indoor air commonly have 10 to 30 minutes response time (Won and Schleibinger 2011), which is slow for an EnKF forecast for faster response. One of the remedies would be to arrange all sensors in a sequential order that successively and continuously acquires observed data from different nodes, instead of concurrent sampling that collects all sensor measurements simultaneously. With EnKF, the forecasting can be updated for all modeled nodes even with only one measurement, no matter which node the measurement comes from. As a result, as far as the EnKF is concerned, the sensor response time can be shortened when using the sequential sampling.

For the current study, four gas samplings were supplied sequentially to one gas chromatography (GC) so each room will have a measurement every 10 minutes, equivalent to a sensor response time of 10 minutes, whereas an observation for the EnKF is available approximately every 2.5 minutes due to the sequential sampling process, if every observation is used for data assimilation. To study the impact of the sensor response time on the forecast, Fig. 4.8 illustrates a comparison of the models with different observation time steps. When the sensor response time increases from 10 minutes to 20 or 30 minutes (observation time step equals to 2.5, 5.0 and 7.5 minutes respectively), the predicting errors also increase. Although instruments with shorter response time and higher resolution can increase forecasting accuracy, further studies are necessary to determine the tradeoffs among sensor resolution, quantities and response time to the system costs, which is beyond the scope of this paper. However, it is shown that the sensor response time and the sampling strategy are important for the accuracy of the EnKF.

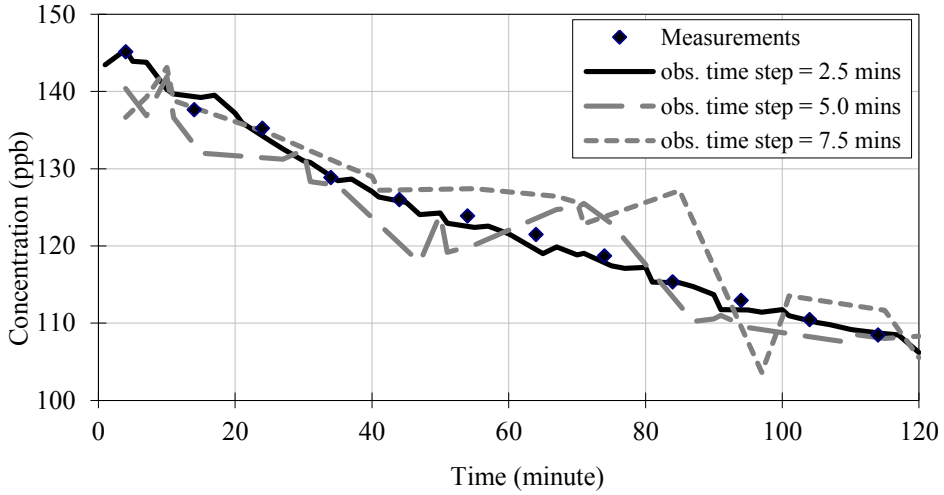

Fig. 4.8 Comparisons of the EnKF predictions models with different observation time steps.

Forecasting lead time and predictability

Another important character of a data assimilation simulation is the forecasting lead time. Fig. 4.9 shows the predictability of the model during the second injection when the observations were stopped being provided for data assimilation at different time step. For example, the grey line with squares starts, t_{stop} = 340 min, represents the observations are not provided after t = 340 min. Since the tracer gas was injected at around t = 350 min, new measurements are required to update the model states so the model fails to predict the injection. By feeding the new measurements from t = 350 to 360 min, the posteriori estimation switches to the bold solid line associated with an improvement of predictability. When the observation feeding then stops at t = 360 min, i.e. the grey line with crosses, the prediction is shown to be within five percent measurement error range only for about 10 mins after SF_6 injection. When more measurements were provided from t = 360 to t = 370 min, the forecasting improves as shown by the grey line with solid squares. This illustrates that in times of an unpredicted major change of indoor air properties, the forecast will require approximate 10 minutes to reach a stabilized model state and provide 60 minutes lead time in prediction. By comparing to the non-EnKF model illustrated by

the bold dotted line, it requires at least 25 minutes to allow posteriori estimation to get into five percent error range. It can be concluded that by providing four sensors with 10 minutes response time (average 2.5 minutes observation time step), the model can quickly respond to sudden concentration changes and provides high quality predictions after about 10 minutes following the injection. When the data is fed continuously without being stopped until t_{stop} = 440 min, the model provides the best accuracy as illustrated by the solid line in the figure.

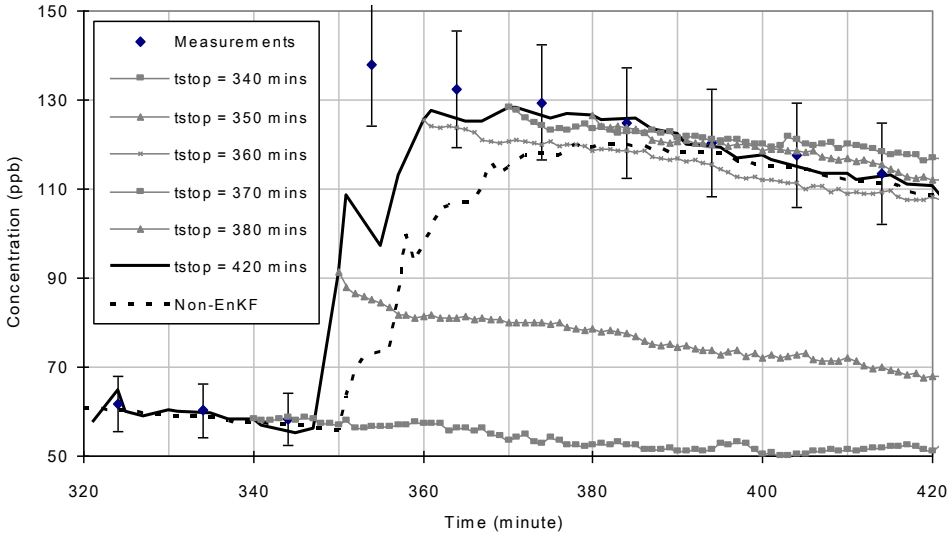

Fig. 4.9 Predictability of the model near the second injection of SF_6 (e.g. t_{stop} = 350 means the observation data feeding for data assimilation stops at t = 350 min).

4.4 Conclusions

This paper applied a new methodology of using an EnKF to forecast the dispersion of contaminant as simulated by a tracer gas in an indoor environment based on the assimilation of multiple sensor data with a mass balance stochastic model. A general setup and key parameters of the model were discussed. By sequentially implementing measurements from different sensors, data assimilation can be performed more frequently to improve model performance. Different from other existing research using the Monte-Carlo method, the reported model in this

paper avoids estimating source strength and location in order to reduce the sampling numbers and still provide noticeable predictability. Overall, this paper concludes that the benefits of using EnKF to forecast indoor air environment are significant. Future research is needed to apply the EnKF to other simulation problems, e.g. computational fluid dynamics, and confirm the results to longer time duration, e.g. a few days or weeks, and other practical cases. It is also necessary to study the tradeoffs among sensor resolution, quantities and response time to the system costs in the future research.

Acknowledgment

This research is supported by Concordia University New Faculty Startup Funds. The authors thank Dr. Nils van Velzen for assisting OpenDA programming and the indoor air quality and ventilation group at the U.S. National Institute of Standards and Technology for providing experimental data.

References

Koo, Sung-Han, Jeremy Fraser-Mitchell, and Stephen Welch. "Sensor-steered fire simulation." *Fire Safety Journal* 45, no. 3 (2010): 193-205.

Freire, Roberto Z., Gustavo HC Oliveira, and Nathan Mendes. "Predictive controllers for thermal comfort optimization and energy savings." *Energy and buildings* 40, no. 7 (2008): 1353-1365.

Oldewurtel, Frauke, Alessandra Parisio, Colin N. Jones, Dimitrios Gyalistras, Markus Gwerder, Vanessa Stauch, Beat Lehmann, and Manfred Morari. "Use of model predictive control and weather forecasts for energy efficient building climate control." *Energy and Buildings* 45 (2012): 15-27.

Tudoroiu, Nicolae, Mohamed Zaheeruddin, E-R. Tudoroiu, and Victor Jeflea. "Fault detection and diagnosis (FDD) in heating ventilation air conditioning systems (HVAC) using an interactive multiple model augmented unscented Kalman filter (IMMAUKF)." In *Human System Interactions, 2008 Conference on*, pp. 334-339. IEEE, 2008.

Liu, Xiang, and Zhiqiang John Zhai. "Prompt tracking of indoor airborne contaminant source location with probability-based inverse multi-zone modeling." *Building and Environment* 44, no. 6 (2009): 1135-1143.

Federspiel, Clifford C. "Estimating the inputs of gas transport processes in buildings." *Control Systems Technology, IEEE Transactions on* 5, no. 5 (1997): 480-489.

Kémajou, Alexis, Léopold Mba, and Pierre Meukam. "Application of Artificial Neural Network for Predicting the Indoor Air Temperature in Modern Building in Humid Region." *British Journal of Applied Science & Technology* 2, no. 1 (2012): 23-34.

Sreedharan, Priya, Michael D. Sohn, Ashok J. Gadgil, and William W. Nazaroff. "Systems approach to evaluating sensor characteristics for real-time monitoring of high-risk indoor contaminant releases." *Atmospheric Environment* 40, no. 19 (2006): 3490-3502.

Gadgil, Ashok, Michael Sohn, and Priya Sreedharan. "Rapid Data Assimilation in the Indoor Environment: Theory and Examples from Real-Time Interpretation of Indoor Plumes of Airborne Chemical." In *Air Pollution Modeling and Its Application XIX*, pp. 263-277. Springer Netherlands, 2008.

Sreedharan, Priya, Michael D. Sohn, William W. Nazaroff, and Ashok J. Gadgil. "Towards improved characterization of high-risk releases using heterogeneous indoor sensor systems." *Building and Environment* 46, no. 2 (2011): 438-447.

Liu, X., and Z. Zhai. "Inverse modeling methods for indoor airborne pollutant tracking: literature review and fundamentals." *Indoor air* 17, no. 6 (2007): 419-438.

Kalman, Rudolph Emil. "A new approach to linear filtering and prediction problems." *Journal of Fluids Engineering* 82, no. 1 (1960): 35-45.

Welch, Greg, and Gary Bishop. "An introduction to the Kalman filter." (1995).

Van Velzen, N. "A Generic Software Framework for Data Assimilation and Model Calibration." *Delft University of Technology, Delft* (2010).

Talagrand, Olivier, and Philippe Courtier. "Variational assimilation of meteorological observations with the adjoint vorticity equation. I: Theory. "*Quarterly Journal of the Royal Meteorological Society* 113, no. 478 (1987): 1311-1328.

Evensen, Geir. "Sequential data assimilation with a nonlinear quasi-geostrophic model using Monte Carlo methods to forecast error statistics." *Journal of Geophysical Research: Oceans (1978–2012)* 99, no. C5 (1994): 10143-10162.

Jahn, Wolfram. "Inverse modelling to forecast enclosure fire dynamics." (2010).

Verlaan, M., Velzen Nv, and S. Hummel. "A generic toolbox for data assimilation in numerical modeling." In *15th biennial conference of the joint numeric*. 2010.

Nabinger, S. J., and A. K. Persily. "Airtightness, Ventilation and Energy Consumption in a Manufactured House: Pre-Retrofit Results." *National Institute of Standards and*

Technology (2008).

Wang, Liangzhu Leon, and Steven J. Emmerich. "Modeling the effects of outdoor gasoline powered generator use on indoor carbon monoxide exposures." In *Building Simulation*, vol. 3, no. 1, pp. 39-50. Tsinghua Press, 2010.

Walton, G. N., and W. S. Dols. "Contam 3.0 user guide and program documentation." *National Institute of Standards and Technology Technical Report NISTIR* 7251 (2010).

Thornber, Hodson. "Finite sample Monte Carlo studies: An autoregressive illustration." *Journal of the American Statistical Association* 62, no. 319 (1967): 801-818.

Whitaker, Jeffrey S., and Thomas M. Hamill. "Ensemble data assimilation without perturbed observations." *Monthly Weather Review* 130, no. 7 (2002): 1913-1924.

Evensen, Geir. "The ensemble Kalman filter for combined state and parameter estimation." *Control Systems, IEEE* 29, no. 3 (2009): 83-104.

Nævdal, Geir, Kristian Thulin, Hans Julius Skaug, and Sigurd Ivar Aanonsen. "Quantifying Monte Carlo uncertainty in the ensemble Kalman filter." *SPE Journal* 16, no. 01 (2011): 172-182.

Won, D. Y., and H. Schleibinger. "Commercial IAQ Sensors and their Performance Requirements for Demand-Controlled Ventilation." (2011).

Chapter 5 Forecasting Smoke Transport during Compartment Fires using a Data Assimilation Model[1]

Abstract

Forecasting simulation of an unknown compartment fire is challenging and usually accompanied with large number of uncertainties. As the simulation progress over time, the forecasted physical conditions such as fire heat release rate, room temperature and vent airflow rate may sway from the reality in a highly dynamic environment. Conventional deterministic fire simulation tools using one set of initial inputs to predict fire smoke transport may not easily generate satisfactory results. In this paper, a new application of Ensemble Kalman Filter (EnKF) to forecast smoke dispersion during compartment fires is presented. The model utilizes measurement data from multiple sensors in multi-room compartments and is able to predict fire heat release rate and smoke dispersions within several minutes. In addition, detailed formulation of the EnKF model and three case studies are also discussed in the paper. The resulting model can be considered as a prototype forecast simulation system to assist occupant evacuation, fire-fighting and smoke extraction in a building fire accident.

5.1 Introduction

Forecast nowadays plays an important role in our daily lives. One of the widely-known examples is weather forecast that gives accurate predictions of atmospheric temperature, wind, and other climate information for hours and days. In the context of buildings, the technology of forecast is relatively new and mostly applied to advanced control strategies of heating, ventilation and air conditioning (HVAC) systems (Kaster et al. 2005). Based on the concept of model predictive

1. The contents of this chapter are published in Lin, Cheng-Chun, and Liangzhu Leon Wang“. "Forecasting smoke transport during compartment fires using a data assimilation model." *Journal of Fire Sciences* (2014): 0734904114548837. The contents are slightly updated.

control (MPC) using forecasted future states of room air as a reference to adjust system control parameters, these advanced control methods are applied to achieving a comfortable indoor environment at reduced energy costs (Morari and Lee 1999, Fux et al. 2014). While forecast aids HVAC controls, its applicability and potential benefits have not been well explored in other fields of building environment, one of which is building fire safety. There are many potential benefits of forecasting fire spread and smoke transport during a fire accident. Forecasting can provide critical information on fire spread and smoke movement to send early warnings for occupant evacuation, fire-fighting practice and to enable early response and control of smoke extraction. Unfortunately, there have been limited forecast studies for building fire safety. This may be due to the nature that fire protection is a life safety issue demanding higher accuracy from forecasted information than that of HVAC controls during non-fire occasions (Kastner et al. 2005 and Bushby 2001). Note that in this paper, the term "forecasting" is referring to predicting future events by computer simulations based on certain numerical methods, which are often stochastic ones due to uncertainties of future events. Therefore, forecasting simulations for building fire safety need to consider the uncertain nature of future events while achieving more accurate results than what are generally required for other forecast applications in buildings.

Many current computer models for building fire safety are deterministic ones, in which a set of user inputs produces one solution. Hence, a deterministic simulation can be considered as one sampling instance of stochastic simulation. According to previous surveys from 10 countries (Friedman 1992, Olenick and Carpenter 2003), the number of computer programs for building fire protection has been increased from 74 to 168 in the past decade. However, a well-known problem of computer fire modeling is that the accuracy of simulation highly relies on users' knowledge to determine appropriate input data. For example, heat release rate (HRR) is one of

the most important and difficult inputs (Babrauskas 1992), which depends on complex chemical reactions associated with fuel type, fuel composition, oxygen quantity and fire temperature. Inappropriate user inputs could cause significant difference between simulation results and measured data. Another potential source of errors is the underlying assumptions of computer models. For example, zone models often assume dividing a room into a hot upper layer and a cold lower layer, within which smoke/air properties are considered uniformly distributed, and ceiling jets (hot gases travel along the ceiling), if any, are neglected. Even the more sophisticated field models, such as computational fluid dynamics models, are based on many assumptions, especially about turbulence modeling, although they provide better spacious resolutions of smoke properties than zone models. Therefore, a computer fire model often needs to be validated by measured data. Experimental validations may provide a "good/poor" verdict about the model functionality, or better off help to improve user inputs and/or adjust model settings. However, they lack the capability of remedying model assumptions and calibrating the model automatically (Rein et al. 2009).

If measurement data are available, some recent studies suggest hybrid approaches combining numerical simulations with measured data from sensors so the measured data can be involved actively to improve computer fire modeling instead of simply giving a verdict. Lee et al. (2004) developed a hybrid neural network fire model to determine fire parameters and predict smoke layer height in single compartment fire. Among 55 predicted samples, only three cases are outside the range envelop of the experimental results. Richards et al. (1996) proposed an inverse model to estimate fire location and HRR by using transient temperature measurements from ceiling sensors. The model can be applied to locate and size the fire source while the results show the average location error is with 1/2 to 1/3 sensor spacing but average HRR error can be

over 100%. Overholt and Ezekoye (2012) used another inverse model based on predictor-corrected method to determine HRR inputs for a computer model, CFAST (Peacock 2005), by using smoke layer temperature measurements. The results indicate each case requires 10 to 30 runs to calculate an inverse HRR solution with a relative error between 0.04 and 0.24. These studies are successful but currently only applied to single compartment fire. For multi-zone compartment fire simulations, Koo et al. (2010) proposed a sensor-linked fire simulation model based on Monte-Carlo method. The model can forecast uncontrolled compartment fire using real-time measurement data. The system currently exploits high performance computing resources in order to forecast in real time and requires thermocouple trees to be located in the center of each room for measuring accurate smoke temperature profile. Hostikka and Keski-Rahkonen (2003) presented a probabilistic fire simulator by combining Monte Carlo simulation and CFAST for a five-room tunnel. The results show the system is able to give a warning of fire damage but the simulations took about one day to complete, which is not fast enough for real application since the CPU time is still greater than forecasted time. Neviackas (2007) developed an inverse fire model using genetic algorithms by minimizing a predefined cost function. The results show good agreement between model estimation and reference HRR but the computation may as well need several hours for multiple-room cases. Additionally, this model also requires some ideal conditions such as measuring mass flow rates through building openings as model inputs. A forecast simulation often needs to combine numerical simulations and measured data (so called data assimilation). Although these previous studies may share similar hybrid concept as data assimilation, the literature review shows that forecast simulations based on data assimilation of multi-room fires with desired accuracy are still at infancy and need to be explored further.

In this study, Ensemble Kalman Filter (EnKF) (Evensen 1994), which is a data assimilation

model often used for numerical weather prediction (NWP) (Navon 2009), is applied to multi-room compartment fires. The selected method, EnKF, is able to solve large-scale problems with low computational requirement and simple implementation so it is one of most popular NWP techniques but is relatively new to the field of building environment (Lin and Wang 2013). The algorithm of EnKF is based on stochastic modeling similar to a Monte Carlo method which makes it especially suitable for parallel computing. Similar to traditional Kalman Filter analysis (Kalman 1960), whenever any measurement datum becomes available during a simulation process, the EnKF will pause the simulation and adjust all model variables (e.g., HRR) then resume simulation using updated parameters. In the following sections, we first introduce the fundamentals of EnKF, and then demonstrate the predictability of the EnKF model by three case studies. The first case is a two-zone fire simulation to present the EnKF capability of model parameter estimation (i.e., correcting input parameters such as HRR). Then, the model is applied to the same two-zone case to demonstrate both model parameter estimation and model state estimation (i.e., forecasting). The third case is a five-zone building to apply the EnKF to multi-room fire forecast simulations. The fire simulations in this paper are based on CFAST 6.3.0 (Peacock 2005) and FDS (McGrattan et al. 2007) developed by the US National Institute of Standards and Technology (NIST), and the EnKF operations are programmed by using a generic data assimilation toolbox, OpenDA (Verlaan 2010), developed by Delft University of Technology, Netherlands.

5.2 Methodology

In this paper, EnKF is the technique to calibrate a numerical simulation of a multi-room compartment fire with measurement data. In order to solve large-scale non-linear forecasting problems, Evensen (1994) proposed a new affordable approach, Ensemble Kalman Filter, using

the Monte Carlo method, and later (2009) detailed the algorithms to combine parameter and state estimations. The following section introduces the fundamental theory in the context of building fire and smoke forecast. Here, consider a time-discrete model of fire simulation:

$$x_{t+1}^{f} = \mathrm{f}(x_t^f, \Phi_t) + w_t \tag{5.1}$$

where x_t^f is a j-dimensional vector representing the forecasted model states in different locations at time step t while superscript f means forecast. It can be noted that j is determined by the number of model states and model nodes. In other words, all model states including temperatures, smoke layer heights and pressures from various modeled locations are all included in x_t^f as one vector. Φ_t is a k-dimensional control vector which refers to model parameters such as HRR and ventilation flow rates through vents. w_t is a vector describing zero mean random white noises accounting for simulation errors. These random noises are sometimes not considered in the EnKF model. But for simulations with high uncertainties such as fire dynamics, it is important to implement a noise model to ensure the true states are always covered in the range of ensemble forecasts. Finally, regarding the function f, it is suggested to apply a low-dimensional system with accurate short-term forecasts (Schrader and Moore 1977). In this paper, the selected function f is the fire simulation tool, CFAST.

When an EnKF model is initiated, a total number of q ensemble members are generated by perturbing the control vector, Φ_t, and initial model states, x_t^f, similar to other Monte Carlo methods and can be presented as

$$\mathbf{X}_t^f = \left[x_t^{f1}, x_t^{f2} \ldots x_t^{fq}\right] \tag{5.2}$$

where the probability density function of the perturbation is assumed to be normally-distributed. The measurement of the model state corresponding to the numerical forecast is expressed as

$$y_t = \mathbf{H}x_t^f + v_t \tag{5.3}$$

where the Matrix **H** is an observation operator which can be an interpolation from model node to observed location. When y_t and $\boldsymbol{x}_t^f$ represent the same physical quantity, **H** can be an identity matrix, **I**. v_t is a vector accounting for random errors of each measurement and is assumed to be independent in all EnKF applications. This is an important feature of EnKF to avoid ensemble collapse caused by rapidly reducing ensemble spread range (Burgers et al. 1998).

Then, the expected error of model states and parameters prediction, as known as the forecasted error covariance, can be estimated by

$$\mathbf{P}_t^f \mathbf{H}^T = \frac{1}{q}\sum_{i=1}^{q}(x_t^{fi} - x_t^t)(\mathbf{H}x_t^{fi} - \mathbf{H}x_t^t)^T \tag{5.4}$$

It can be observed that EnKF is using a finite size of q ensemble members to estimate forecasted error covariance for $q \to \infty$. Since the true state of the model, x_t^t, is unknown, it is here approximated by the average of ensemble members.

$$x_t^t \approx \overline{x_t^f} = \frac{1}{q}\sum_{i=1}^{q} x_t^{fi} \tag{5.5}$$

Substitute the above $\overline{x_t^f}$ into Eq. (5.6), Eq. (5.4) becomes

$$\mathbf{P}_t^f \mathbf{H}^T = \frac{1}{q-1}\sum_{i=1}^{q}(x_t^{fi} - \overline{x_t^f})(\mathbf{H}x_t^{fi} - \mathbf{H}\overline{x_t^f})^T \tag{5.6}$$

where a factor of *1/(q-1)* is applied instead of *1/q* in order to make the estimation unbiased. Finally, a weighted factor K_t between simulation results and the observations, so-called Kalman gain, can be determined by using the traditional Kalman Filter equation where optimal model state parameters are estimated as

$$x_t^a = \overline{x_t^f} + \mathbf{K}_t(y_t - \mathbf{H}\overline{x_t^f}) \tag{5.7}$$

Where

$$\mathbf{K}_t = \frac{\mathbf{P}_t\mathbf{H}^T}{\mathbf{H}\mathbf{P}_t\mathbf{H}^T + \mathbf{R}} \tag{5.8}$$

It can be noted that if m number of measurements are available at time t, the dimension of $\mathbf{K}$ is $m \times k$, which is irrelevant to the number of ensemble member q since all ensemble members are updated with the same set of $\mathbf{K}$. $\mathbf{R}$ is the measurement error covariance of v_t with its dimension $m \times m$. Although some parameters of the control vector $\boldsymbol{\Phi}_t$ cannot be directly measured, they can still be updated using Eq. (5.7) by merging it into $\boldsymbol{x}_{t+1}^f$ so the vector dimension becomes $n = j + k$. For example, HRR can be statistically estimated in this way by using temperature and smoke layer height measurements.

After obtaining best estimated model states and model parameters, the forecast simulation can continue and preform prediction to the next time step.

$$\boldsymbol{x}_{t+1}^f = \mathrm{f}(\boldsymbol{x}_t^a, \boldsymbol{\Phi}_t) + \boldsymbol{w}_t \tag{5.9}$$

The benefit of EnKF in forecasting is that important model parameters and model states are all updated in its analysis, so the forecast simulation model can maintain desired accuracy in a long simulation time window.

The foregoing EnKF algorithms are implemented in OpenDA and CFAST is linked to OpenDA by using its "black box" functionality. The source codes of CFAST 6.3.0 are also modified to add a restart function to meet the pausing/resuming requirement of EnKF analysis. The modified source codes are validated with the outputs from the original version and the results are consistent with only rounding errors. In order to accelerate simulations and avoid convergence problems in some special cases, wall materials in all simulations are removed from CFAST input

data while the thermal boundary condition is assumed to be adiabatic. The removal of wall materials reduces simulation accuracy and in fact creates a more challenging situation for the EnKF analysis.

5.3 Forecasting smoke transport using ensemble Kalman filter

To evaluate the capability of EnKF in forecasting multi-zone compartment fire, three different case studies are conducted. We started with a simple two-zone case to demonstrate combining model parameter and model state estimation using EnKF and then moved to a more complex five-zone case to show the predictability of smoke transport improved by EnKF. All three case studies focus on early stage of fires, when it is relatively challenging to predict smoke layer height before reaching steady state. The forecast model here is based on CFAST, while the observations (i.e. "measurement" in an EnKF analysis) are either obtained from CFAST itself or Fire Dynamic Simulator (FDS) as shown in Table 5.1. Here, we choose FDS to produce the observations because FDS provides more detailed data than the experiments. All FDS outputs used in the case studies have been validated by experiment results (Tilley et al. 2011, Jones et al. 2009 and Peacock et al. 1988).

Table 5.1. EnKF model parameters for three case studies

Case	Model states (Forecasted by CFAST) x^f	Parameters (Unknowns) Φ	Observations y	Outputs (Estimated by EnKF) X^a
A (two zone)	T_{room}, T_{atrium}, h_{room}, h_{atrium}	Q, m_z	Perturbed CFAST outputs T_{room}, T_{atrium}, h_{room}, h_{atrium}	Q, m_z
B (two zone)	T_{room}, T_{atrium}, h_{room}, h_{atrium}	Q, m_z	FDS outputs T_{room}, T_{atrium}, h_{room}	Q, m_z, h_{atrium}
C (five zone)	T_{FR}, T_{E1}, T_{Cor}, T_{E2}, T_{TR} h_{FR}, h_{E1}, h_{Cor}, h_{E2}, h_{TR}	Q	FDS outputs T_{FR}, T_{Cor}, h_{FR}, h_{Cor}	T_{TR}, h_{TR}

*FR = Fire Room; E1 = Entrance One; E2 = Entrance Two; Cor = Corridor; TR = Target Room

5.3.1 Case A: Estimation of Heat Release Rate and Mechanical Ventilation Rate

The objective of the first case study is to evaluate the capability of EnKF in parameter estimation for a two-zone compartment fire. The case study is a two-room fire test based on a series of experiments and FDS simulations from Poreh et al.'s and Tilley et al.'s research. Regarding model geometries, the fire source is located in a small room adjacent to an atrium with a mechanical ventilation vent at the atrium ceiling as shown in Fig. 5.1. In addition to HRR, the ceiling mechanical ventilation rate is also considered important for the determination of the smoke layer height of the atrium. Case A is based on a series of experimental and numerical study in the literature, where the mechanical ventilation rates and HRRs are varied in different cases. The mechanical ventilation rate may be known for each specific case but this study tries to demonstrate a general approach for different ventilation flow rates. It also creates a more challenging case than that with known flow rate. In reality, the actual performance of a mechanical fan depends on its "fan-curve", in which the flow rate is a function of pressure difference across the fan. As a result, the fan may have a nominal design flow rate based on standard test condition but the actual fan flow rate is still unknown. In such cases, the analysis in Case A is practically relevant. Since HRR cannot be directly measured in compartment fire experiments, it is usually approximated by measuring fuel or oxygen consumption. In this case, it is difficult to justify if the HRR measurement can be considered as true state to verify the model predictability because measurement uncertainties cannot be excluded. To conduct parameter estimation analysis, previous studies often use numerical data as true state values (Overholt and Ezekoye 2012, Chang and Latif 2013) to avoid uncertainties from experiments. Here, the focus of this case is to show how EnKF is able to improve the CFAST simulation by assimilating with noisy measurements to correct inaccurate initial inputs. We use a similar method as the previous

study as follows.

First, a CFAST model is conducted by using a constant 7.67 kW fire and 0.14 m^3/s vent flow rate while the resultant smoke layer height (h) and smoke temperature (T) in the two rooms are considered as true states (i.e., correct results) with 10-second resolution. The correct results of smoke layer height and smoke temperature are then perturbed by adding noises and considered as measurements with respective uncertainty.

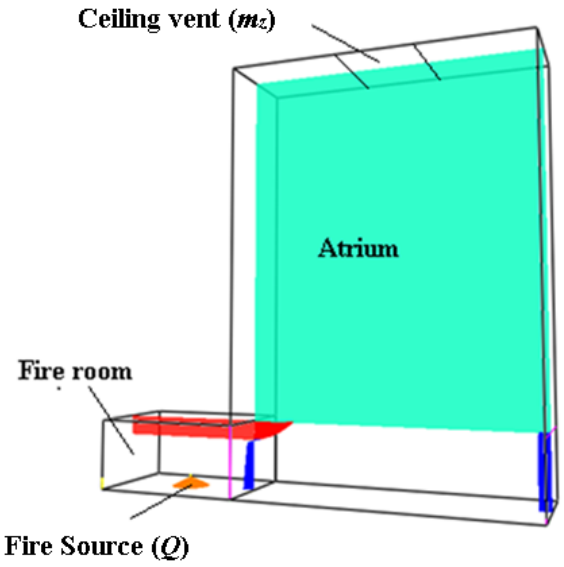

Fig. 5.1 Overview of the two-room test building in CFAST

Second, the specific settings of the CFAST simulation are defined as follows. The initial guess of the HRR and the mechanical ventilation rate is based on a normal distribution where 68.2% of the probabilities are within the range of 6.8 kW to 13 kW and 0.05 m^3/s to 0.25m^3/s respectively. The range is determined by multiple tests while model convergence problems are more likely to occur when widening this perturbation range. The perturbation range cannot be further widened due to the convergence problems possibly due to the limitations of the current model after consulting with the CFAST developers. For the perturbation range without the convergence problems, we have validated our modifications of the CFAST source codes by ensuring the

results are consistent with those from the original version with only rounding errors. For observation uncertainties, the expected error of each measurement is assumed to be independent, and 10%, 20% and 30% of the measurement error covariance for each sensor is assigned respectively in matrix **R** in Eq. (5.8). After applying the EnKF model, HRR and mechanical ventilation rate can be estimated whenever measurements are available.

Fig. 5.2 (a) shows the atrium smoke layer height predicted by 100 ensemble members which covers a very wide range. The bold line indicates ensemble average which is closer to the true state than most of the ensemble members. The region in the dotted rectangle is enlarged in Fig. 5.2 (b) for more detailed information. As shown in Fig 5.2 (b), the ensemble average is significantly improved by the EnKF analysis when being assimilated with measurement data. It can be observed that the update of EnKF is effective: all smoke layer height predictions at different times are updated closer to the true states as indicated by the arrow.

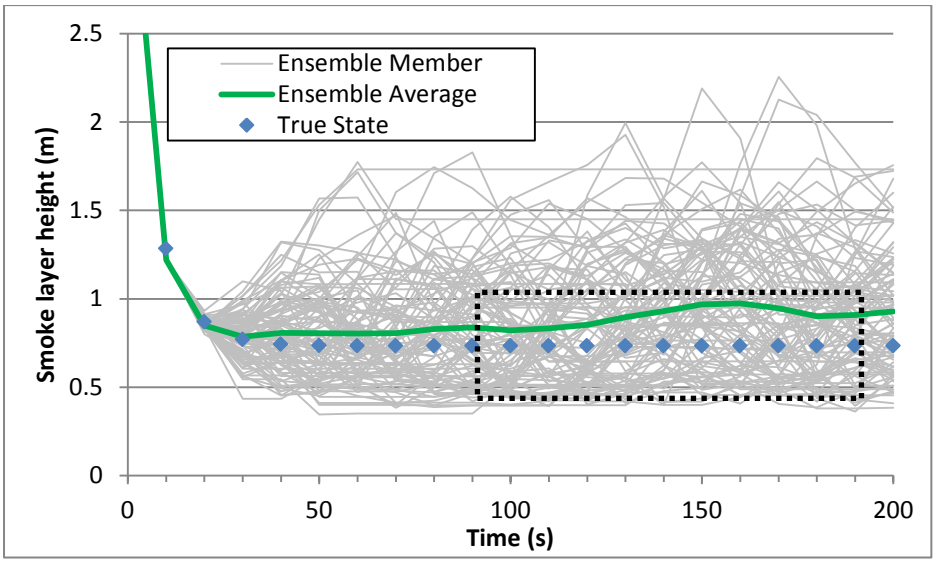

Fig. 5.2 (a) Atrium smoke layer height outputs of 100 Ensemble members

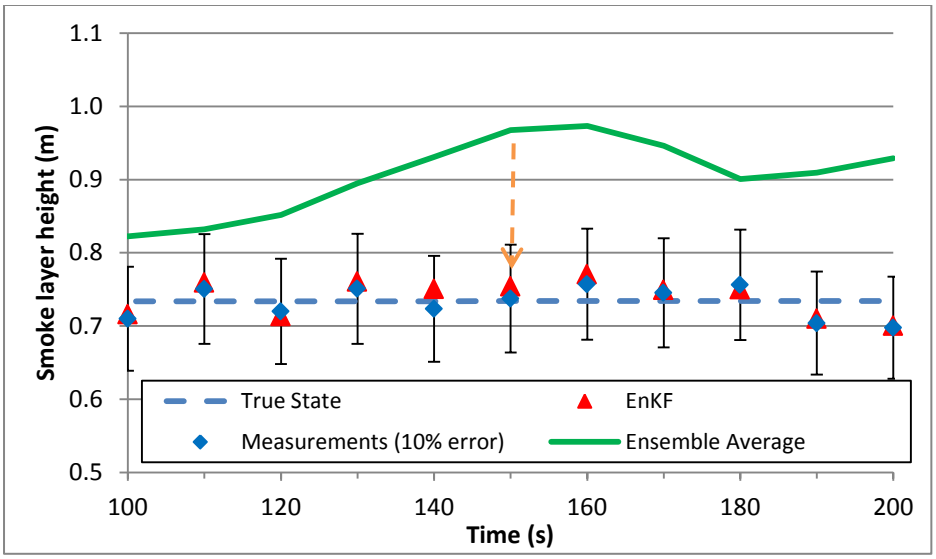

Fig. 5.2 (b) Comparisons of atrium smoke layer height outputs

At the same time, the model parameters, Q and m_z, are also updated. As shown in Fig. 5.3 and 5.4, the hatched areas are the initial guess ranges of Q and m_z and the dashed lines are the true states of the corresponding model parameter. The simulation starts from using initial guess value of Q and m_z as inputs. As simulation progress in time, the measurements become available from t=10 s and EnKF starts to update model parameters. It can be observed that EnKF successfully estimate HRR and mechanical ventilation rate but all three cases seem to overestimate HRR by about 15 to 20 percent. This is due to the probability density function of initial perturbation is normally distributed while more ensemble members are located near the center of the range envelop which is 10.1 kW in this case. So the estimated model parameters lie between the true state (7.67 kW) and the mean value (10.1 kW) while the magnitude of deviations are determined by the uncertainties of the measurements. It can be observed that the accuracy of measurements affects the results of parameter estimations, in which the cases with lower measurement errors (e.g. 10%) generally achieve better prediction. Other cases with the HRR of 12.56 kW and m_z of 0.136 to 0.214 m^3/s are also conducted and show similar predictability in parameter estimations (not included to avoid repetition).

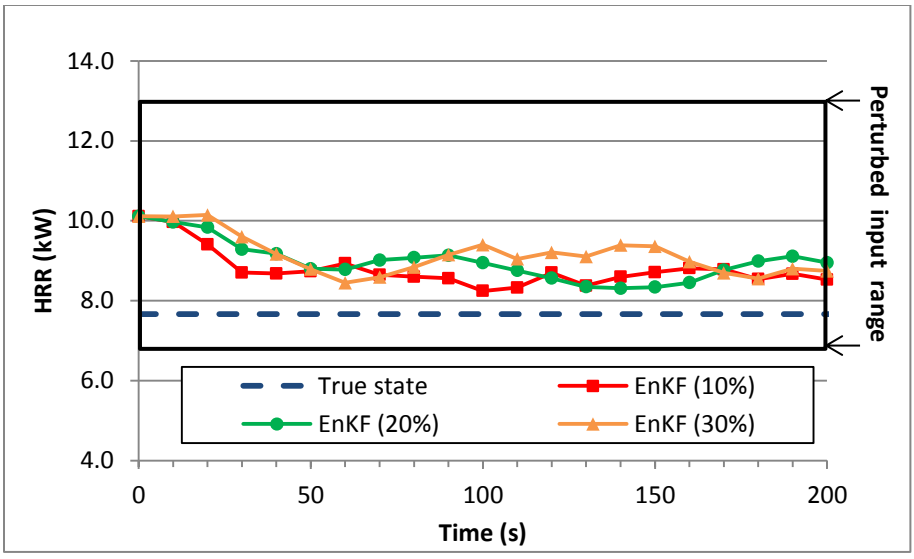

Fig. 5.3 Prediction of HRR using EnKF model

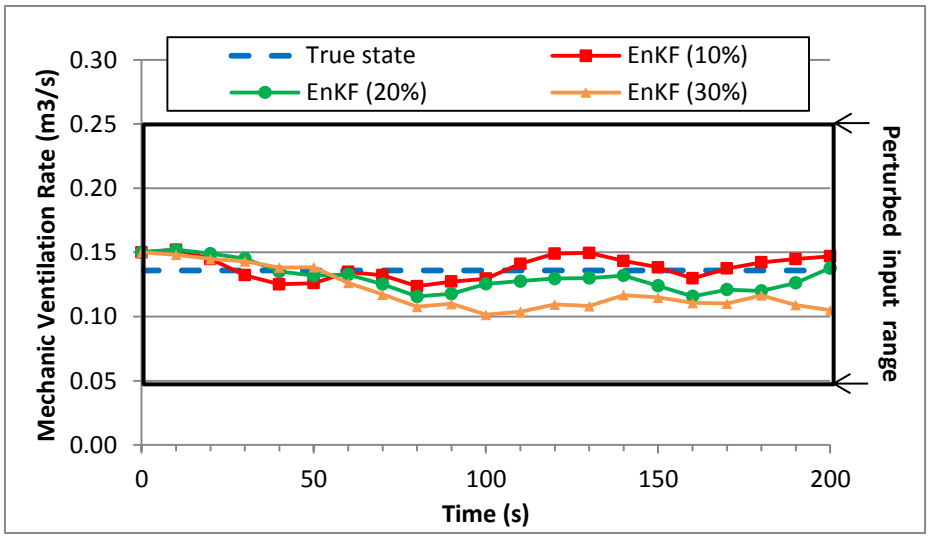

Fig. 5.4 Prediction of mechanic ventilation rate using EnKF model

5.3.2 Case B: Prediction of smoke layer height

In addition to model parameter estimation of HRR and mechanical ventilation rate, the second case study also includes forecast of model states including smoke temperature and smoke layer height. This case study is based on the same scenario as the first one but using validated FDS outputs as measurements (Tilley et al. 2011, Zhao and Wang 2013). In order to evaluate the

EnKF model to predict model states and parameters, the atrium smoke layer height measurements (h_{At}) are not given in this case. Instead, it is later used to verify the predictability of the EnKF model. Based on the FDS simulation results from the previous study Lee et al. 2004), four selected cases are conducted using different combinations of $\dot{Q}$ and $\dot{m}_z$ as shown in Table 5.2. Although mechanical ventilation rate $\dot{m}_z$ is a known input in FDS and can also be controlled by an operator in the experiment, the actual air mass flow rate through the duct is still very different from the set point in a compartment fire. It is therefore considered as an unknown model parameter in this case. The resulting smoke temperature and smoke layer height from FDS outputs are recorded with 10-second resolution and later used as measurements.

Following the same procedure as Case A, four EnKF simulations are conducted using exactly the same inputs while the only difference is that the measurement data are based on FDS simulations in this case. This is similar to forecast an unknown fire while HRR and ventilation rate can only be roughly estimated in the beginning. After the simulation progress in time, the measurements become available and are used to adjust the simulation parameters to improve predictability. The results of B1 case are presented with details in figures and the results of B2, B3 and B4 are summarized in Table 5.3.

Table 5.2 FDS model inputs and EnKF parameter perturbation ranges of the two-room fire tests

Case #	$\dot{Q}$ (kW)	$\dot{m}_z$(m^3/s)
B1	12.56	0.214
B2	12.56	0.126
B3	7.67	0.136
B4	7.67	0.117
EnKF range	7.1 to 13.1	0.6 to 0.24

Fig. 5.5 demonstrates a comparison of atrium smoke layer height predictions by using different simulation tools/inputs. Dashed line shows a-priori CFAST simulation by a central ensemble member using mean values of HRR and mechanical ventilation rate (center of the perturbed

range) as inputs while the results are very different from FDS outputs (approximated true state). It is not surprising that the a-priori CFAST simulation performs poorly because of inappropriate HRR input, which is used here as a base line for comparison. By using correct inputs (the same inputs as FDS), the posteriori CFAST results improve but still with some overestimations as shown by the dashed-dotted line. Finally, the solid line illustrates the results by using EnKF, in which the inputs of HRR and mechanical ventilation rate are the same as the a-priori simulation but measurement data are used for data assimilation at every simulation time step (10 seconds) during the whole simulation. It can be observed that EnKF results are closer to FDS outputs (solid squares) than the a-priori and a-posteriori CFAST models. Similar results can be found for other cases as shown in Table 5.3, where all EnKF cases perform better than a-priori CFAST models. This is due to the fact that EnKF not only estimates model parameters but also adjusts model states at the same time.

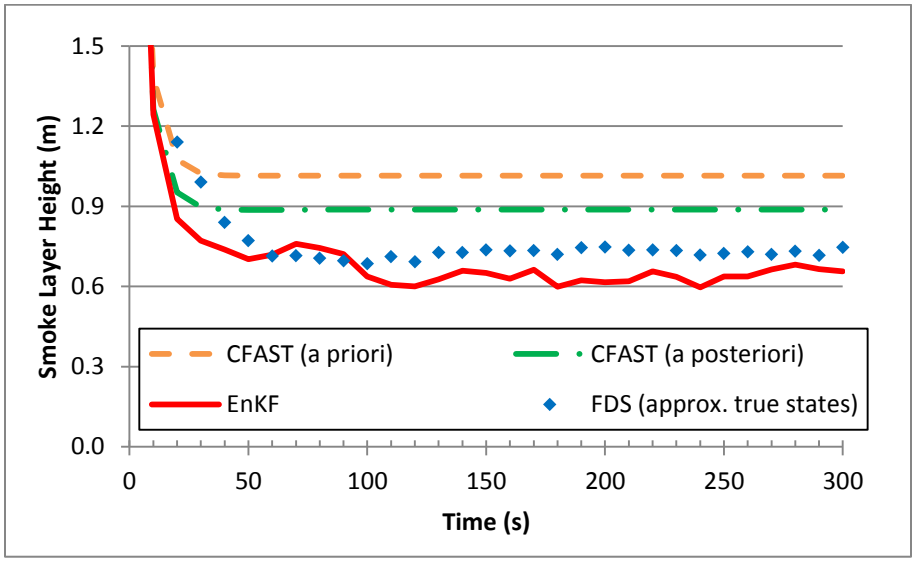

Fig. 5.5 Comparisons of atrium smoke layer height outputs (Case B1)

Table 5.3 Root mean square errors of atrium smoke layer height prediction by different methods when compared to FDS simulation results

Case #	CFAST A priori (m)	CFAST A posteriori (m)	EnKF (m)
B1	0.28	0.16	0.08
B2	0.58	0.19	0.23
B3	0.47	0.23	0.17
B4	0.19	0.10	0.13

It can be concluded in this case study that by using EnKF to forecast smoke layer height, the simulation only requires users to define a reasonable range of HRR and mechanical ventilation rate. The model is able to estimate model parameters and forecast smoke transport when measurements become available.

5.3.3 Case C: Forecast smoke spread in a multi-room compartment fire

To further demonstrate the capabilities of EnKF in a more complicated case, the third case study applies the EnKF model to a five-zone fire simulation. This case study is based on a series of experiments performed by NIST and has been used to validate FDS and CFAST (Jones et al. 2009, Peacock and Reneke 2007). The test building consists of five compartments including fire room, corridor, target room and two small spaces connecting mentioned rooms near entrances as shown in Fig. 5.6. The fire source is a 110 kW constant fire. The doorway connecting the corridor to the exterior is opened during the whole test.

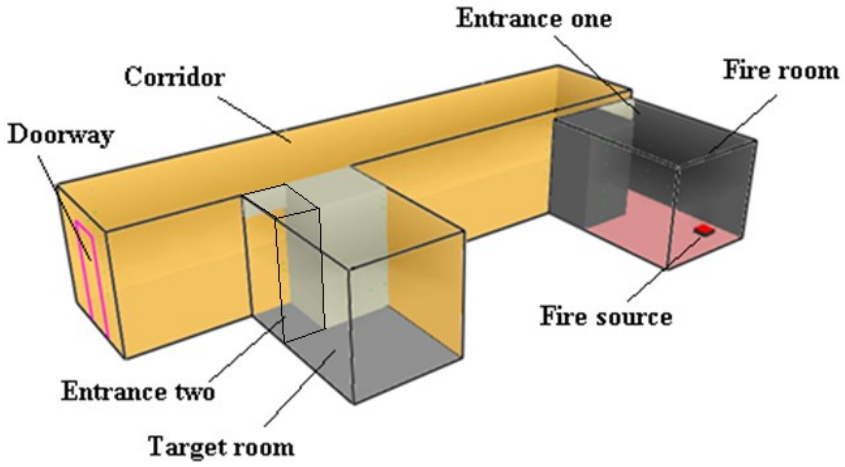

Fig. 5.6 Overview of the five-zone fire test building in FDS

From the validation study of FDS and CFAST, both tools perform well for the rooms close to fire source (not included here but can be found in McGrattan et al. 2007, Peacock and Reneke 2007). Fig. 5.7 shows the smoke filling process of the target room in the early stage of the fire by comparing outputs from different models and experiment measurements. The figure illustrates that before t = 70 s, it is difficult to measure smoke layer height in the experiment since the smoke layer is not well developed so the smoke layer height is hard to be determined (McGrattan et al. 2007). Before t = 70 s, it can be found that both FDS and CFAST outputs are reasonably close. During the same period, both programs also predict a similar smoke filling process in the corridor as shown by the SmokeView (Forney 2013) visualization in Fig. 5.8. SmokeView is a smoke visualization tool developed by the US NIST. At t = 20 s, the smoke starts to propagate into the corridor along the ceiling then reaches the far end and also gets into the entrance two at t = 30 s. In general, although the smoke layer of the corridor is formed at about t = 30 s, the quantity of smoke calculated by CFAST as indicated by the solid line is still reasonable in the early stage by comparing to that of FDS.

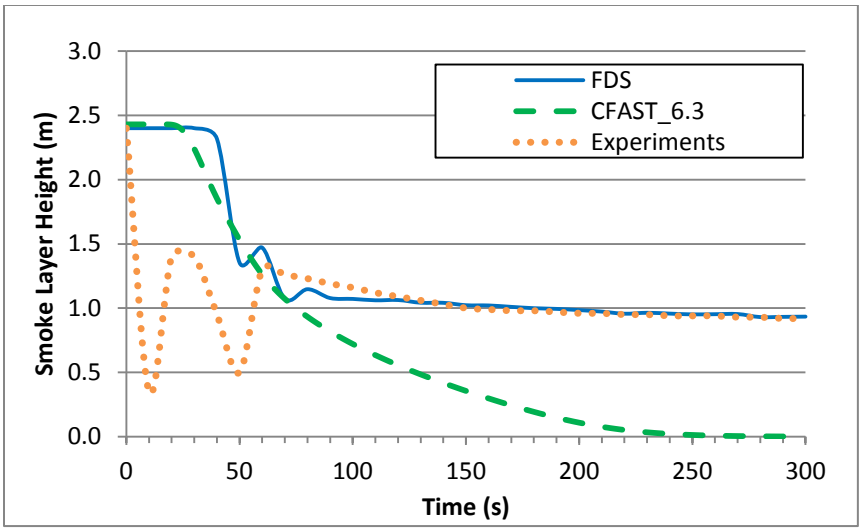

Fig. 5.7 Comparisons of target room smoke layer height from experiment measurements and simulation results

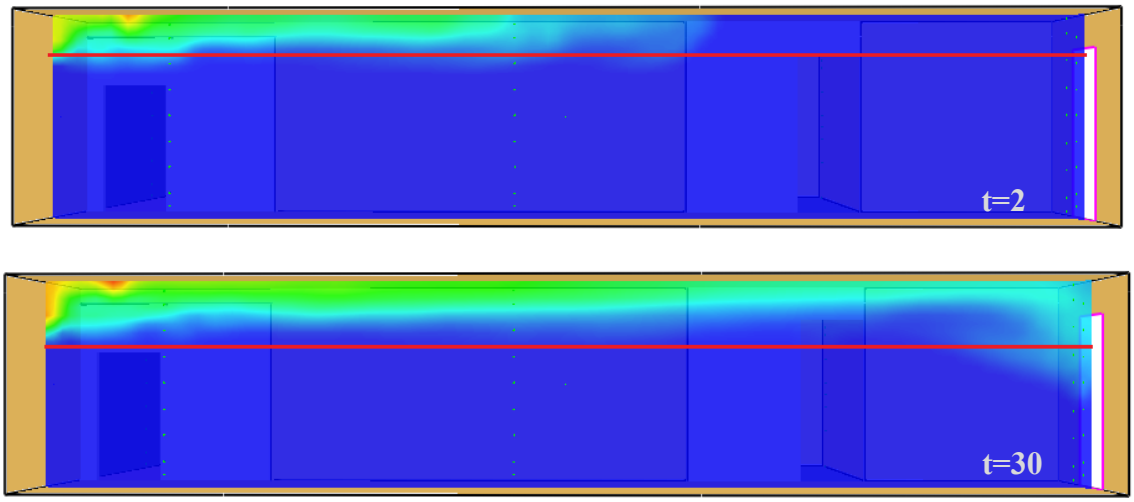

Fig. 5.8 Comparisons of smoke layer height outputs from FDS and CFAST in the corridor

After t = 70 s, more smoke gets into the target room and the smoke layer can be measured consistently in the experiment (Fig. 5.7). In the meantime, CFAST significantly underestimates the smoke layer height in the target room. A closer look at the smoke filling process is provided by Fig. 5.9 where the air temperature is illustrated by different colors as shown by the legends on the right side. After t = 70 s, the smoke enteris the target room and forms a smoke layer. The quantity of smoke in the room starts showing differences between CFAST and FDS at t = 70 s.

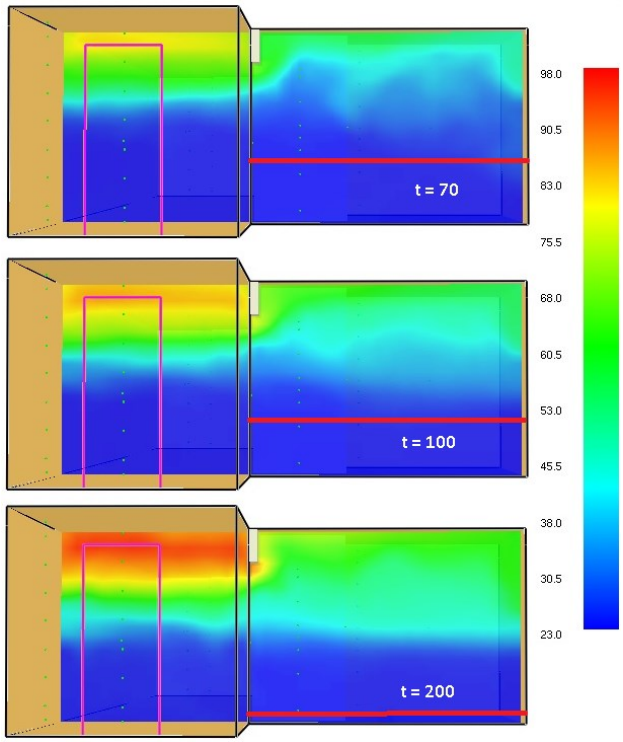

Fig. 5.9 Comparisons of smoke layer height outputs in the target room for a fire of 110 kW

At t = 100 s, CFAST starts to further underestimate the smoke layer height and shows significant difference from FDS outputs. Finally at t = 200 s, the smoke layer height is about 0.11 m from CFAST while FDS result is around 1 m.

The significant discrepancy of CFAST from FDS simulations of the target room comes from the CFAST assumptions. In CFAST, each compartment is divided into two layers in which air properties are assumed to be uniform, and a ceiling jet is not modeled. This method simplifies calculations but also creates problems in the corridor. Due to momentum effect, more smoke will exit the corridor through the doorway directly than entering the target room as illustrated in Fig. 5.8. CFAST thus overestimates the mass flow rate through the entrance two as shown in Fig. 5.10. After 70 s, the mass flow rate actually reaches a steady state as illustrated by the dashed line whereas the CFAST prediction continues to increase till it reaches a value of over two times more than that of FDS at about 200 s. This explains why the smoke layer height in CFAST is

much lower than that in FDS as shown by Fig. 5.9. Although CFAST implemented a delay function for the smoke spread in a long corridor (Bailey et al. 2002), we tried different delay functions for the smoke dispersion through the long corridor but the predictability cannot be improved.

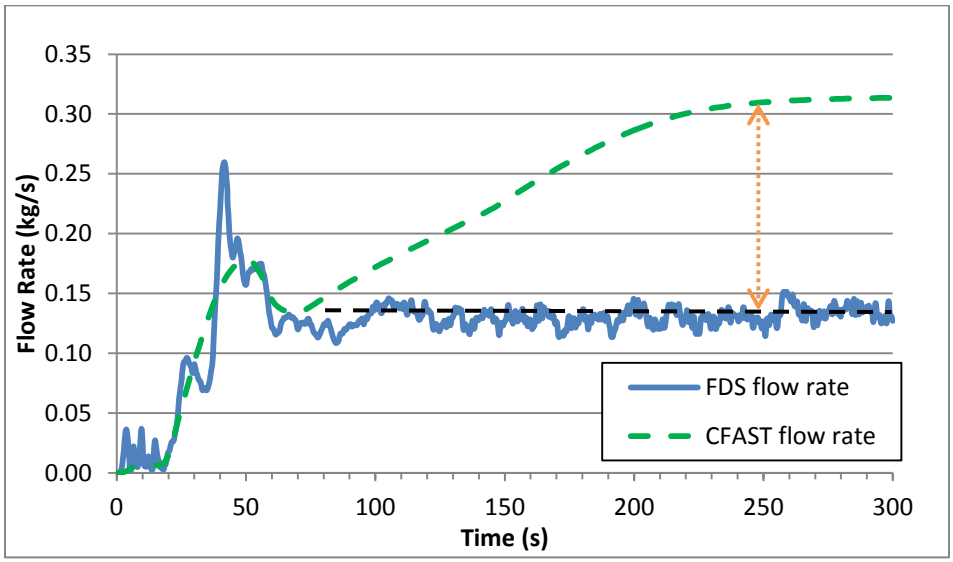

Fig. 5.10 Comparisons of the mass flow rate through the entrance two

This case shows an example how model assumptions affect simulation accuracy. Here we implement an EnKF-based solution to improving the CFAST simulation. In order to take into account the forecast uncertainties of the mass flow rate through the corridor doorway, a virtual sink of mass is added in the corridor to consider excessive mass loss through the door way for model state correction. The mass sink helps to leverage the mass flows distributed between the entrance two and the corridor doorway so that the smoke flow through the doorway can be correctly considered in CFAST. This sink is considered as an uncertainty of 0 to 0.2 m^3/s to the exterior. The range is determined by comparing the FDS and CFAST simulation results to make sure the perturbed flow rate can cover the true state as illustrated by dotted-arrows in Fig. 5.8. Regarding other parameter perturbations of the EnKF model, the uncertainty of the fire source

HRR is assumed to be 50% since the accurate HRR is not given. The uncertainties of measurements are assumed to be 10% for the spatial errors (Steckler et al. 1982 and Quintiere 1984) which are about 10°C for smoke temperature and 0.1 m for smoke layer height. Finally, the number of ensemble member q is set at 100 as suggested by the previous study (Lin and Wang 2013). The measurement data to be assimilated with the CFAST simulation during the EnKF analysis include the smoke temperatures and smoke layer heights in the fire room and the corridor. After applying these setups to the EnKF model, the resulting smoke temperature and smoke layer height in the target room are used to verify model predictability.

Fig. 5.11 shows the smoke layer height prediction of the target room by comparing outputs from different approaches. Originally, the smoke layer predicted by CFAST (dashed line) keeps descending after 70 seconds and finally reaches the floor level at 250 seconds. But the FDS results (solid squares) indicate the steady state of the smoke layer height should be at approximately 1.0 m height. After applying EnKF, the smoke layer height prediction shifts to a range between 1.0 m and 1.4 m after 80 seconds which shows significant improvement.

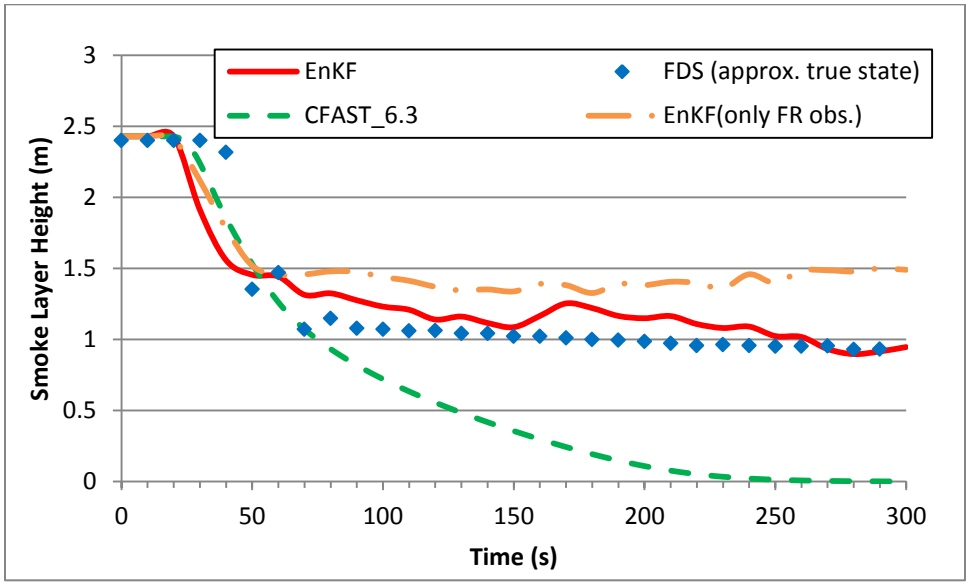

Fig. 5.11 Comparisons of target room smoke layer height outputs

Fig. 5.12 shows the results of smoke temperature prediction of the target room by using difference methods. The solid squares illustrate 10 seconds average of FDS outputs which is considered as an approximation of the true state and the dashed line is CFAST posteriori estimation. It can be observed that the smoke temperature is about 15 to 20°C lower than the true state even though the appropriate HRR is already given. After applying EnKF, the smoke temperature prediction shifts closer to the solid line after the model states and parameters are adjusted in the EnKF analysis.

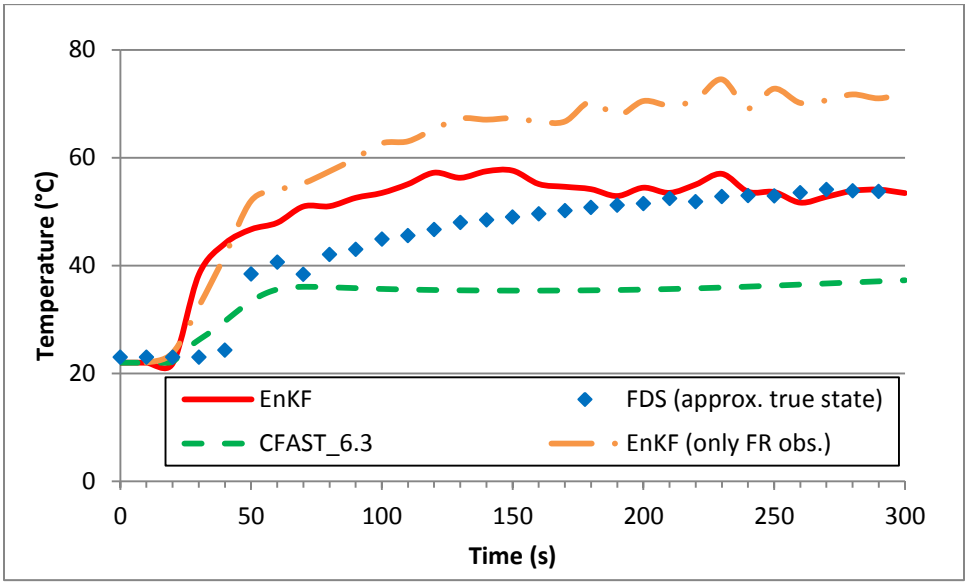

Fig. 5.12 Comparisons of target room smoke temperature outputs

The EnkF simulation in the previous discussion uses the measurements of smoke temperatures and smoke layer heights in both the fire room and the corridor. In order to demonstrate the importance of the number of measurements used in EnKF analysis, a case with only fire room smoke temperature and smoke layer height measurements is also conducted. The results are illustrated as dash-dotted lines (only FR observation) in Fig. 5.11 and 5.12. It can be observed that the smoke layer height prediction is worse than the previous case but is still within a reasonable range of 1.2 m to 1.5 m. But the temperature prediction error is about 20 °C which

accounts for about 28% relative error. This is due to the virtual sink is located in the corridor and no local measurements in the target room are used in this case so the EnKF model is less effective than the previous case.

Finally, a comparison of the simulation time and the predictability using three different methods is presented in Table 5.4. The predictions of smoke temperature and smoke layer height have significant improvement after applying EnKF. The total simulation time required by EnKF is 520 seconds without using any parallel computing on an Intel 2.8GHz processor while FDS may require almost an hour to complete with the same hardware. In addition, for the EnkF simulation, over 80% of computational time is associated with processing the ensemble members sequentially. Currently, the model requires 520 seconds to perform a simulation of 300 seconds. If parallel computing is applied to the model to process multiple ensemble members simultaneously, the model will be potentially able to run in real time for the five-zone compartment fire prediction.

From a practical perspective, to apply this model to predict fire and smoke dispersion to improve building fire safety, the HRR of an unknown fire accident can be first estimated by the fuel load and ventilation conditions of a given space with a reasonable range. When a fire accident occurs and the fire alarm is activated, the fire source is then assumed to be located in the closest room to the triggered smoke detector and start taking measurements from the sensors. After the EnKF analysis, the computer simulations are calibrated with the measurements and generate a more accurate prediction of fire growth and smoke dispersion which can be used in automated smoke management, evacuation assistance and decision making in firefighting. For example, the occupants can follow the signs and avoid going toward toxic smoke while fire fighters can have a general idea about firefighting strategies before entering the building.

Table 5.4 Comparisons of model predictability and CPU time

	Temperature prediction error	Smoke layer height prediction error	CPU time (seconds)
CFAST	28%	53.6%	0.8
EnKF	16.5%	16.5%	520
FDS	-	-	3330

*The error percentage is based on root mean squared error divided by the average

5.4 Conclusions and future work

A new method to forecast smoke dispersion in a compartment fire by combining state and parameter estimation is presented. To solve the problems associated with the inaccurate user inputs and model assumptions, the EnKF model assimilates different types of sensor data such as smoke temperature and smoke layer height measurements to improve model predictability. The resulting model is able to forecast long-distance smoke transport from the fire source in a compartment fire. Comparing to other parameter estimation techniques in compartment fire simulations that require solving large adjoint matrices, EnKF only needs to operate around 100 ensemble members within a few minutes and can sequentially calibrating the forecast model with measurement data. The results from three case studies are showing noticeable predictability while the computational requirement is relatively low.

For those who would apply EnKF to other simulation models, it is suggested to apply a low-dimensional model with highly accurate short-term forecasts. This is due to the fact that the EnKF will directly use the simulation model to perform predictions when measurements are not available. Therefore, simulation tools with lower accuracy with fewer measurements available will not benefit well from EnKF. In addition, modifications of the simulation tools are sometimes required. For example in Case C of this study, a virtual sink is added in the corridor to take into account model limitations due to assumptions. This modification makes the sampling of

ensemble members to focus more on most likely errors to improve the model efficiency.

Future studies would require looking into the parameter perturbations and simulation model convergence criteria. This is due to the fact that, in some cases, when the deviations of model parameters exceed about 60%, some ensemble members will have difficulty to converge in CFAST. In addition, spurious correlations should also be looked into since it is a common problem in all EnKF applications. The case studies presented in this paper are based on buildings with two to five rooms while all model states are highly-correlated. When the model is applied to a larger building, the EnKF model should implement a more detailed localization method to avoid model parameters and states updated with irrelevant measurements such as sensor data from a room far away from a fire source.

References

Kastner, Wolfgang, Georg Neugschwandtner, Stefan Soucek, and H. M. Newmann. "Communication systems for building automation and control." *Proceedings of the IEEE* 93, no. 6 (2005): 1178-1203.

Morari, Manfred, and Jay H Lee. "Model predictive control: past, present and future." *Computers & Chemical Engineering* 23, no. 4 (1999): 667-682.

Fux, Samuel F., Araz Ashouri, Michael J. Benz, and Lino Guzzella. "EKF based self-adaptive thermal model for a passive house." *Energy and Buildings*68 (2014): 811-817.

Bushby, S. T. "Integrating Fire Alarm Systems with Other Building Automation and Controls Systems." *Fire Protection Engineering* 11 (2001): 18-20.

Friedman, Raymond. "An international survey of computer models for fire and smoke." *Journal of Fire Protection Engineering* 4, no. 3 (1992): 81-92.

Olenick, Stephen M., and Douglas J. Carpenter. "An updated international survey of computer models for fire and smoke." *Journal of Fire Protection Engineering* 13, no. 2 (2003): 87-110.

Babrauskas, Vytenis, and Richard D. Peacock. "Heat release rate: the single most important variable in fire hazard." *Fire safety journal* 18, no. 3 (1992): 255-272.

Rein, G., C. Abecassis-Empis, A. Amundarain, H. Biteau, A. Cowlard, A. Chan, W. Jahn et al. "ROUND-ROBIN STUDY OF FIRE MODELLING BLIND-PREDICTIONS USING THE DALMARNOCK FIRE TEST." In *Proceedings of the 5th International Seminar on Fire and Explosion Hazards*, vol. 23, p. 27. 2007.

Lee, Eric WM, Richard KK Yuen, S. M. Lo, K. C. Lam, and G. H. Yeoh. "A novel artificial neural network fire model for prediction of thermal interface location in single compartment fire." *Fire Safety Journal* 39, no. 1 (2004): 67-87.

Richards, R. F., B. N. Munk, and O. A. Plumb. "Fire detection, location and heat release rate through inverse problem solution. Part I: Theory." *Fire safety journal* 28, no. 4 (1997): 323-350.

Overholt, Kristopher J., and Ofodike A. Ezekoye. "Characterizing heat release rates using an inverse fire modeling technique." *Fire technology* 48, no. 4 (2012): 893-909.

Peacock, R. D., W. W. Jones, P. A. Reneke, and G. P. Forney. "Consolidated Model of Fire Growth and Smoke Transport (Version 6), User's Guide." *NIST Special Publication* 1041.

Koo, Sung-Han, Jeremy Fraser-Mitchell, and Stephen Welch. "Sensor-steered fire simulation." *Fire Safety Journal* 45, no. 3 (2010): 193-205.

Hostikka, Simo, and Olavi Keski-Rahkonen. "Probabilistic simulation of fire scenarios." *Nuclear engineering and design* 224, no. 3 (2003): 301-311.

Neviackas, Andrew. *Inverse fire modeling to estimate the heat release rate of compartment fires*. ProQuest, 2007.

Robinson, Allan R., and Pierre FJ Lermusiaux. "Overview of data assimilation." *Harvard reports in physical/interdisciplinary ocean science* 62 (2000): 1-13.

Navon, Ionel M. "Data assimilation for numerical weather prediction: a review." In *Data Assimilation for Atmospheric, Oceanic and Hydrologic Applications*, pp. 21-65. Springer Berlin Heidelberg, 2009.

Evensen, Geir. "Sequential data assimilation with a nonlinear quasi-geostrophic model using Monte Carlo methods to forecast error statistics." *Journal of Geophysical Research: Oceans (1978–2012)* 99, no. C5 (1994): 10143-10162.

Lin, Cheng-Chun, and Liangzhu Leon Wang. "Forecasting simulations of indoor environment using data assimilation via an Ensemble Kalman Filter." *Building and Environment* 64 (2013): 169-176.

Kalman, Rudolph Emil. "A new approach to linear filtering and prediction problems." *Journal of Fluids Engineering* 82, no. 1 (1960): 35-45.

McGrattan, Kevin B., Bryan Klein, Simo Hostikka, and Jason Floyd. "Fire dynamics simulator

(version 5), user's guide." *NIST special publication* 1019, no. 5 (2008): 1-186.

Verlaan, M., Velzen Nv, and S. Hummel. "A generic toolbox for data assimilation in numerical modeling." In *15th biennial conference of the joint numeric*. 2010.

Evensen, Geir. "The ensemble Kalman filter for combined state and parameter estimation." *Control Systems, IEEE* 29, no. 3 (2009): 83-104.

Schrader, B. P., and S. F. Moore. "Kalman filtering in water quality modeling: Theory vs. practice." In *Proceedings of the 9th conference on Winter simulation-Volume 2*, pp. 504-510. Winter Simulation Conference, 1977.

Burgers, Gerrit, Peter Jan van Leeuwen, and Geir Evensen. "Analysis scheme in the ensemble Kalman filter." *Monthly weather review* 126, no. 6 (1998): 1719-1724.

Tilley, Nele, Pieter Rauwoens, and Bart Merci. "Verification of the accuracy of CFD simulations in small-scale tunnel and atrium fire configurations." *Fire Safety Journal* 46, no. 4 (2011): 186-193.

Jones, W. W., R. D. Peacock, G. P. Forney, and P. A. Reneke. "Consolidated Model of Fire Growth and Smoke Transport (Version 6): Technical Reference Guide." *NIST SP* 1026.

Peacock, Richard D., Sanford Davis, and Billy T. Lee. *An experimental data set for the accuracy assessment of room fire models*. Center for Fire Research, 1988.

Poreh, Michael, Norman R. Marshall, and Amir Regev. "Entrainment by adhered two-dimensional plumes." *Fire Safety Journal* 43, no. 5 (2008): 344-350.

Chang, Shoou-Yuh, and Sikdar MI Latif. "Use of kalman filter and particle filter in a one dimensional leachate transport model." In *Proceedings of the 2007 National Conference on Environmental Science and Technology*, pp. 157-163. Springer New York, 2009.

Wang, Liangzhu Leon, and Guanchao Zhao. "Numerical study on smoke movement driven by pure helium in atria." *Fire Safety Journal* 61 (2013): 45-53.

Peacock, R. D., and P. A. Reneke. "Verification and Validation of Selected Fire Models for Nuclear Power Plant Applications, Volume 5: Consolidated Fire Growth and Smoke Transport Model (CFAST)." *NUREG-1824, US Nuclear Regulatory Commission, Washington, DC* (2007).

Forney, Glenn P. *Smokeview (version 6) a Tool for Visualizing Fire Dynamics Simulation Data Volume II: Technical Reference Guide*. 2013.

Bailey, J. L., Glenn P. Forney, P. A. Tatem, and W. W. Jones. "Development and validation of corridor flow submodel for CFAST." *Journal of Fire Protection Engineering* 12, no. 3 (2002): 139-161.

Steckler, K. D., James G. Quintiere, and W. J. Rinkinen. "Flow induced by fire in a compartment." In *Symposium (international) on combustion*, vol. 19, no. 1, pp. 913-920. Elsevier, 1982.

Quintiere, James G., K. Steckler, and D. Corley. "An assessment of fire induced flows in compartments." *Fire Science and Technology* 4, no. 1 (1984): 1-14.

Chapter 6 Scaled Compartment Fire Experiment

6.1 Background information

Compartment fire experiments have had great success in broadening knowledge of building fires. However, the cost of a building fire experiment is usually high and the test is not easily replicated because the building being tested is often damaged by the fire and is not always fully recoverable. There is additional difficulty creating an identical ambient environment since most experiments are conducted outdoors in uncontrollable weather conditions. Numerical experiments (i.e., computer simulations) and scaled fire experiments are alternative ways to study building fires that are not susceptible to such problems. Although numerical experiments are widely used and noticeably accurate, the use of computer simulations alone to study a specific fire phenomenon is not recommended (Johansson 2014). In fact, the only affordable option for investigating certain types of compartment fire problems such as atrium fires and shaft smoke transport is scaled fire experimentation. Although the scaling laws that relate small-scale tests to full-scale results are only applicable to certain types of fuels, building materials, and compartment geometries (Jolly and Saito 1990; Babrauskas 1995 and 1997), the method can still give a general picture for predicting smoke temperature and smoke layer height (Moodie and Jagger 1992).

The goal of the experiment presented in this chapter is to study the effects of changing fire source HRR and the opening/closing of doors on the smoke filling process of a compartment fire. These are very common events of real compartment fire accidents. As previously mentioned, these events are unpredictable, which makes smoke and fire spread difficult to predict. According to the existing literature, most established fire experiments usually attempt to apply one

condition to the entire test to avoid undesirable changes, but this does not produce desirable results to test dynamical updating of data assimilation. The experiment is specially designed to study dynamic events during a compartment fire.

6.2 Experiment setups

The experiment setup is a 1:5 scaled building based on a series of experiments conducted by NIST (Peacock et al. 1988 and 2007). As shown in Fig. 6.1., the scaled building consists of three rooms. The fire room is built entirely with cement board, except for one wall, which is built with fire-proof glazing for smoke visualization. The other two rooms are constructed entirely of 0.8 cm-thick acrylic glass. These three rooms are connected by 0.4 m × 0.15 m doors. There are three doors of the same size in the corridor that lead out of the compartments. Doors 2 and 3 are closed for most of the tests, while Door 1 remains open.

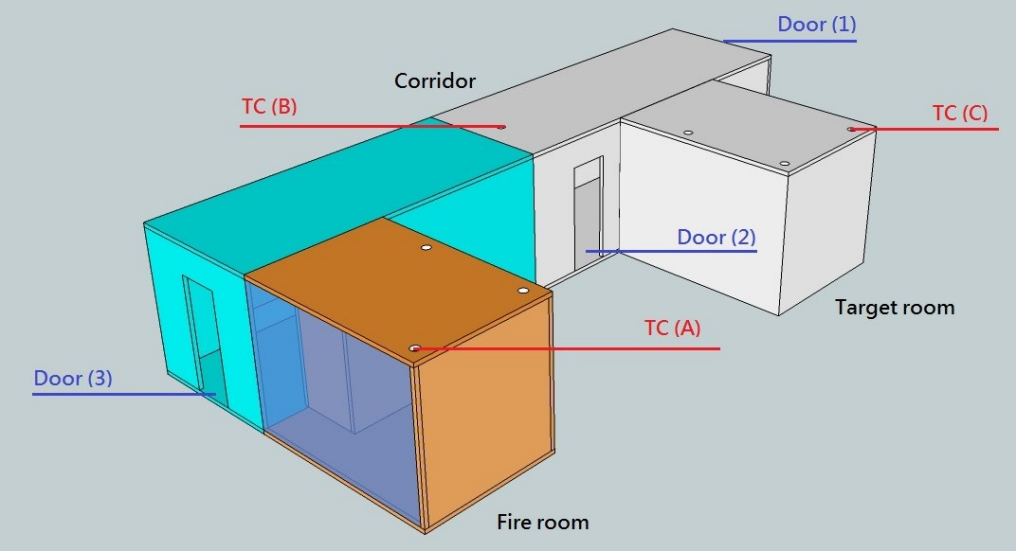

Fig 6.1 (a) Description of experimental setups

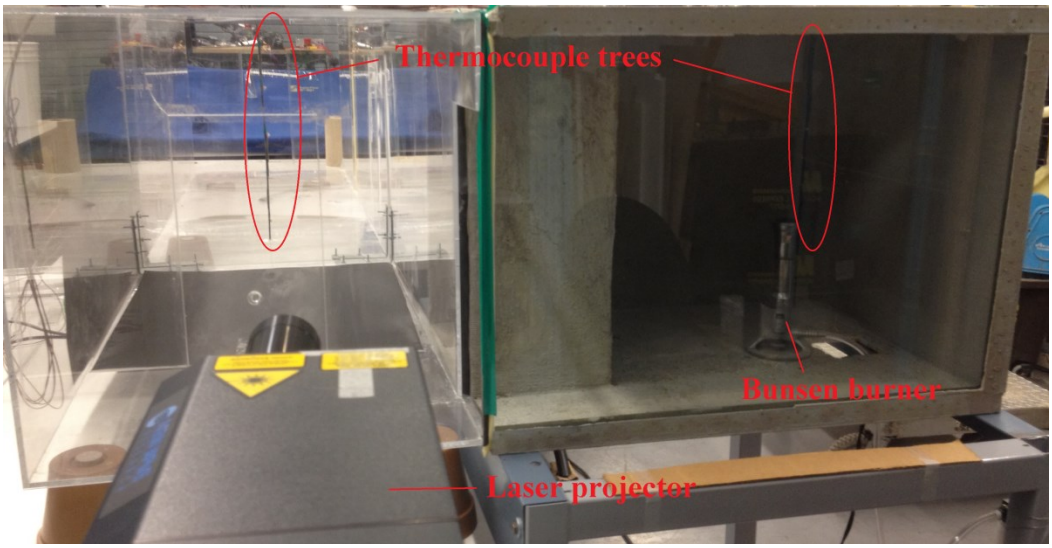

Fig 6.1 (b) Experimental setups - apparatus

Table 6.1 Geometries and material properties of the scaled building

	Length	Width	Height	Material
Fire room	70	50	50	Acrylic glass Cement board
Corridor	250	50	50	Acrylic glass
Target room	70	50	50	Acrylic glass
*unit: centimeter				
	Conductivity kW/(m K)	Specific Heat (kJ/kg K)	Density (kg/m^3)	Thickness (cm)
Acrylic glass	0.0019	1.47	1185	0.8
Cement board	0.29	0.84	1200	1.5

The fire source is a Bunsen burner connected to a propane cylinder whose flow rate is controlled by a flow meter and is located in the fire room. To prevent oxygen starvation and reduce experimental uncertainties, the tube to the propane gas supply is fed to the outside air through a small (0.1 m × 0.1 m) opening in the floor. To obtain the temperature measurement, three thermocouple trees, each consisting of five type K thermocouples, are installed in each room. The lowest one is located 5 cm above the floor and the highest one is 45 cm above the floor. The other three thermocouples are located in-between these two and spaced 10 cm apart, as show in Fig 6.1. An Agilent 34970A data acquisition unit is linked to all thermocouples and a PC that

records measurements every one second.

Since the hot gases in this experiment are generated with high efficiency from a Bunsen burner, the hot gases are transparent and therefore hard to capture visually. In order to visualize the flow pattern of the hot gases and observe the smoke layer height, artificial smoke is injected into the fire room right next to the burner. The injected smoke is generated by a smoke machine that uses fog fluid to make hot gases visible. To further enhance the effect, the smoke particles are illuminated by two sheets of green laser light, as shown in Fig 6.2. In addition, the images captured by digital camera are then analyzed with particle image velocimetry (PIV). Detailed discussions regarding experiment setups are included in Section 7.1.4.

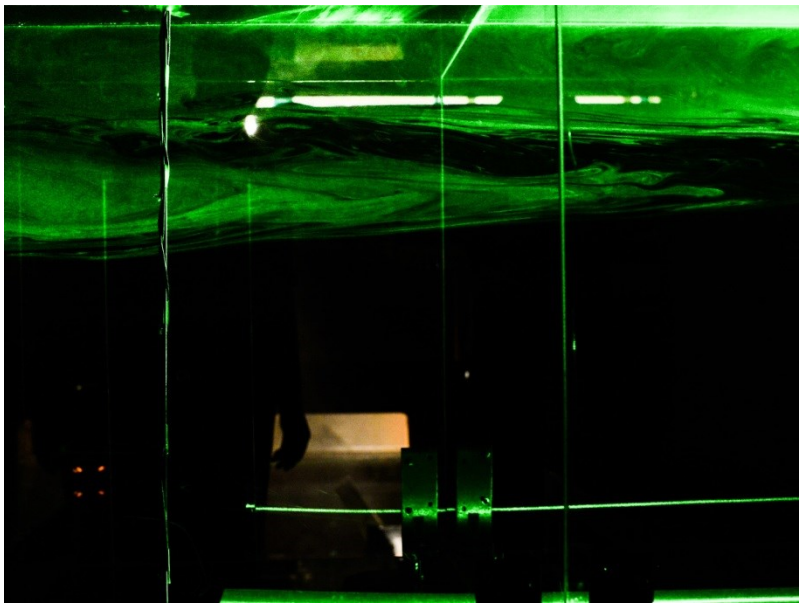

Fig 6.2 Visualization of smoke layer using artificial smoke and laser light

6.3 Smoke temperature and smoke layer height

The study of the smoke transport process of a compartment fire is based on comparisons of average smoke temperature and smoke layer height. In this experiment, the temperature measurements obtained from three thermocouple trees are converted into smoke layer height and average smoke temperature for easier comparison. The smoke temperature at the interface, T_{Hd},

is given by:

$$T_{Hd} = C_s(T_{max} - T_{floor}) + T_{floor} \tag{6.1}$$

where T_{max} is the maximum measured temperature and T_{floor} is the temperature measured near the floor level. C_s is an empirically determined factor equals to 0.2 (Peacock et. al 1988). The average smoke layer temperature is determined by the mean integrated temperature measurement over the layer:

$$T_U = \int_{H_d}^{H_{room}} \frac{T(z)}{H_{room}} dz \tag{6.2}$$

where H_d is the height at which the smoke temperature is T_{Hd} and can be determined by linear intepolation. H_{room} is the height of room. Fig. 6.3 shows an example of converting thermocouple tree measurements into smoke layer height and smoke temperature. The smoke layer height, or the interface height, is located where the temperature rise is 20% over the entire room, which is approximately 0.28 m. By applying Eq. (6.2), the smoke temperature, or the upper layer temperature, can be determined and is 99.5 °C in this case.

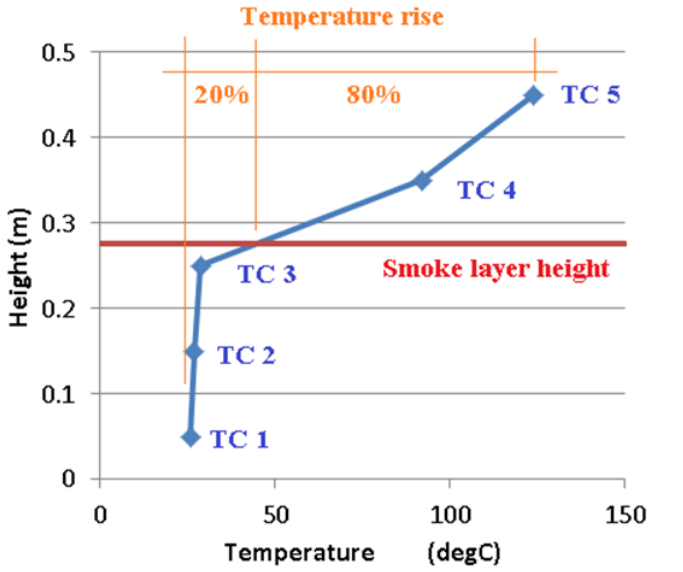

Fig 6.3 Thermocouple measurements and smokelayer height

Before testing the effects of dynamic events, a series of tests using the same HRR of 2.0 kW and door opening setups is conducted to calibrate all equipment. Fig 6.4 shows the temperature measurements of one thermocople compared to FDS simulation results. The deviations between the tests are negligible (less than 5%), and the results are also close to FDS outputs. Thus, it can be confirmed that the experiment is highly repeatable.

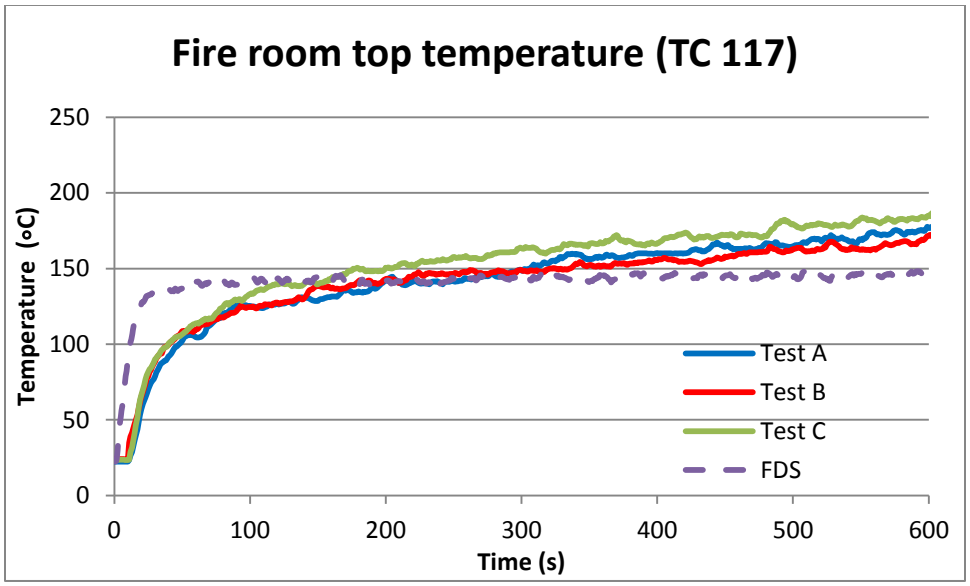

Fig 6.4 Comparisons of ceiling thermocouple measurement in the fire room

6.4 Results and discussions

6.4.1 Case A – change of HRR

The heat release rate (HRR) of the fire source is the dominant feature of any compartment fire (Babrauskas 1992). It is determined by complex chemical reactions that are usually not easily predictable. In this experiment, the fire source is a Bunsen burner, which makes it much easier to control. This setup enables comparisons of the effect of fire source HRR on smoke transport.

First, three experiments with constant HRRs are conducted, with values of 1.5, 2.0 and 2.8 kW based on the propane gas flow rate to the burner. Fig 6.5(a) shows the temperature rise in the fire room for all cases. The rate of temperature rise is very different for all three cases, even

immediately after ignition of the burner. As expected, the case with higher HRR has a higher rate of smoke temperature rise. The same phenomenon can be observed in the corridor and target room, but with approximate 20- and 40-second time delays, respectively, due to the time required for hot gases to transport to these two non-fire rooms and build up a smoke layer. A comparison of the temperature rise of the 2.0 kW and 2.8 kW cases in the fire room at t = 100 seconds reveals a significant temperature difference when the HRR increases by 40% (i.e., from 2.0 kW to 2.8 kW). A 40% increment may seem high for a well-controlled fire, but for a full-scale underdeveloped compartment fire in different ventilation conditions, the HRR uncertainties can be significant especially in the early growth stages (Makhviladze et al. 2006).

Another experiment using non-constant fire is conducted, in which the HRR begins at 1.5 kW and then changes to 2.8 kW at t = 180 seconds. In Fig 6.5(a), the purple contour shows a sudden temperature rise at around 180 seconds in the fire room due to the change of fire HRR. The sudden temperature rises of the other two rooms have similar time delays of 20 to 40 seconds.

While strong correlations were found between average smoke temperature and HRR, the correlations between smoke layer height and HRR are much weaker, as shown by Fig 6.6. The smoke layer height contours obtained from temperature measurements in the fire room are nearly identical. Similar results can be found from the corridor measurements. But, for the higher HRR case (2.8 kW), the smoke layer descends faster in the early stage due to the fire source's higher flow rate. After around 120 seconds, once the same layer is well-developed in the corridor, all three cases show nearly identical smoke layer height.

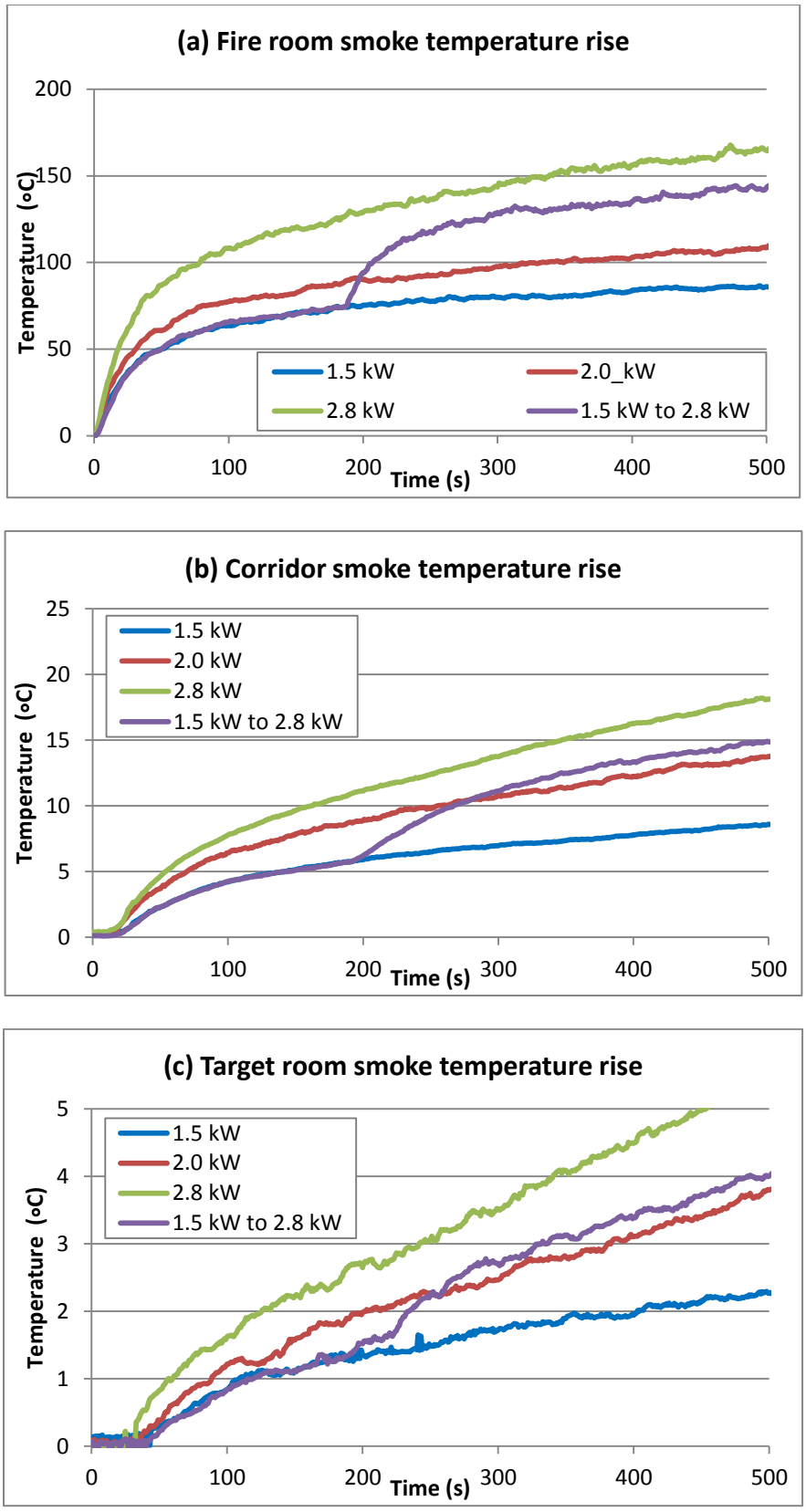

Fig 6.5 Comparisons of average smoke temperature rise in three rooms

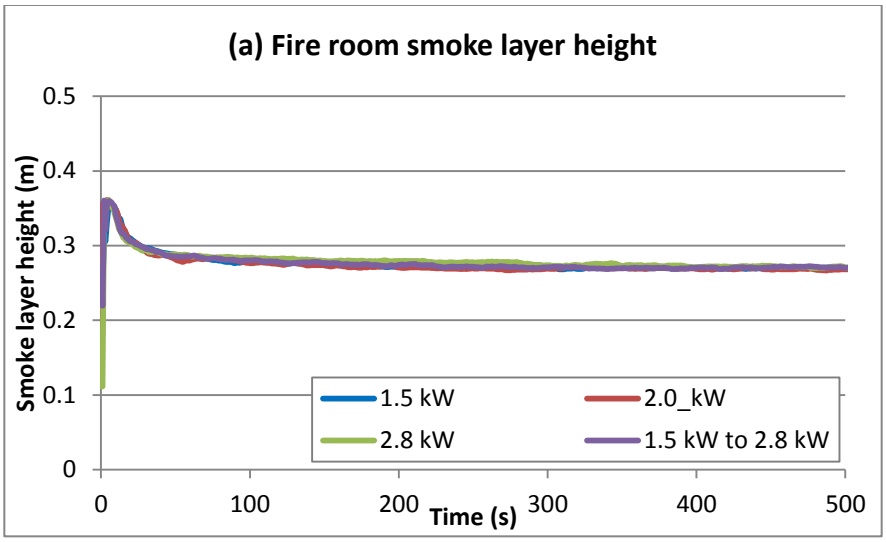

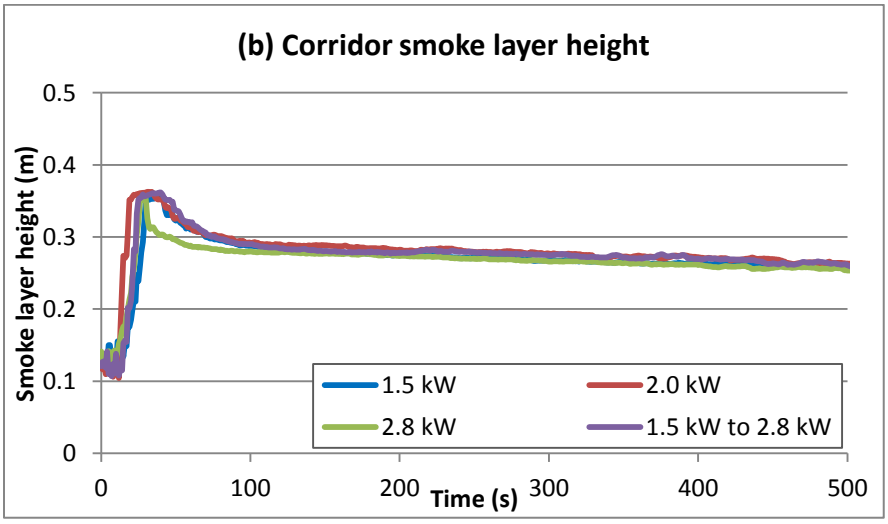

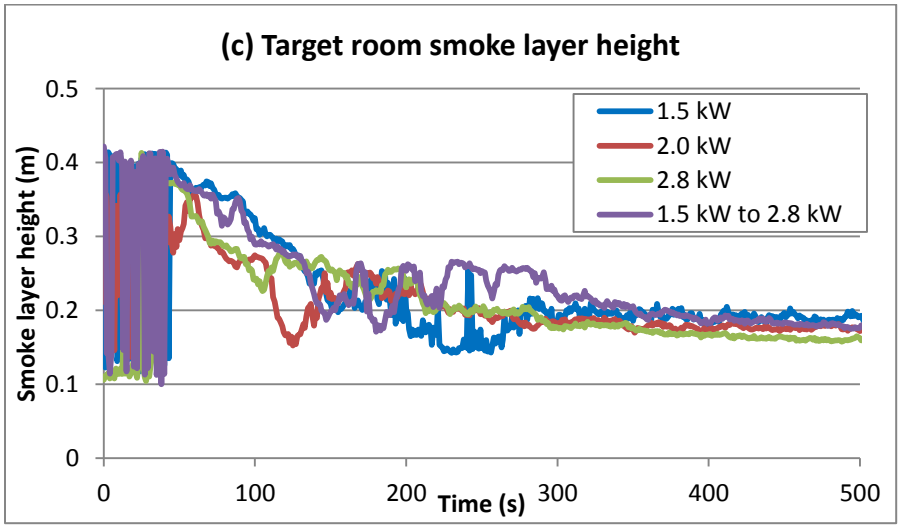

Fig 6.6 Comparisons of smoke layer height in three rooms

For the target room smoke layer height, it is necessary to check the near-ceiling thermocouple measurements to determine the time at which the hot gases enter the room. Fig 6.7 indicates that the air temperature rise near the ceiling is first detected at 30 seconds after ignition of the burner in the 2.8 kW HRR case. For the 2.0 kW and 1.5 kW HRR cases, hot gases reach the target room at 36 and 42 seconds, respectively. This is due to the higher HRR fire sources also generate more mass/volume of hot gases. In other words, the flow speed is higher and the time required to reach the target room is shorter for high HRR cases. By obtaining the average travel time of smoke reaching the target room, the observations at the time when no smoke enters the target room can be excluded.

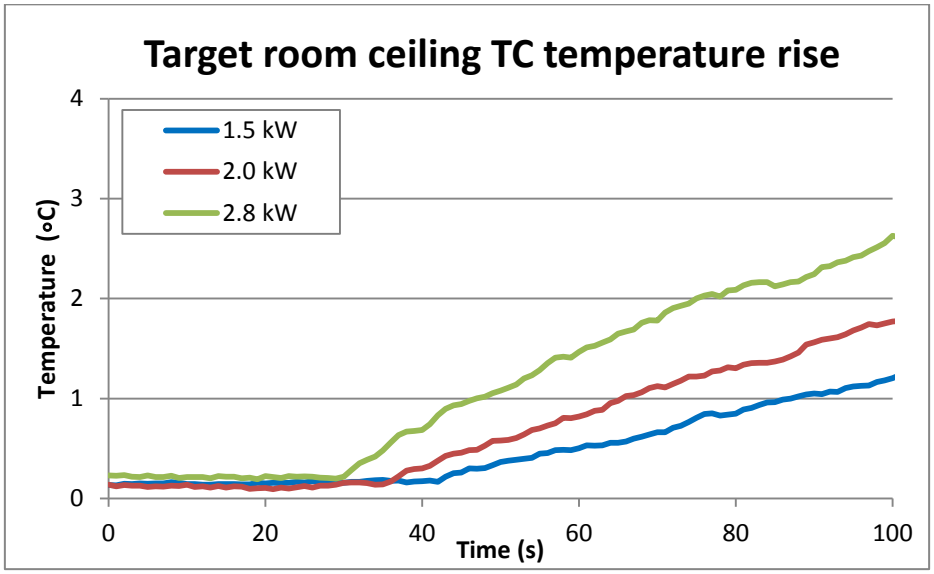

Fig 6.7 Temperature rise of target room ceiling thermocouple measurement

Fig 6.6(c) shows that, in general, in the case with higher HRR, the smoke layer descends faster in all three rooms. But, for the non-constant HRR case, the smoke layer height rises after HRR is increased from 1.5 kW to 2.8 kW. This can be explained by comparing the temperature profiles at different times. Fig 6.8 illustrates the temperature profile in the target room at 150, 200 and 250 seconds after ignition. Originally, the temperature profile at 150 seconds, as shown by the

blue contour, is a smooth curve using 1.5 kW HRR. When the HRR changes to 2.8 kW at 180 seconds, hotter gases start entering the room at around 200 seconds and change the temperature profile, which creates a steep temperature rise above 0.25 meters height, as shown by the green contour. This change also results in the rise of the smoke layer height at 200 seconds. As the hotter smoke generated by the 2.8 kW fire keeps entering the room, the lower layer air is heated, as shown by the purple contour, and the smoke layer height starts descending. Finally, the temperature profile changed back to its original smooth shape only when measured at temperatures higher than those measured at 150 seconds.

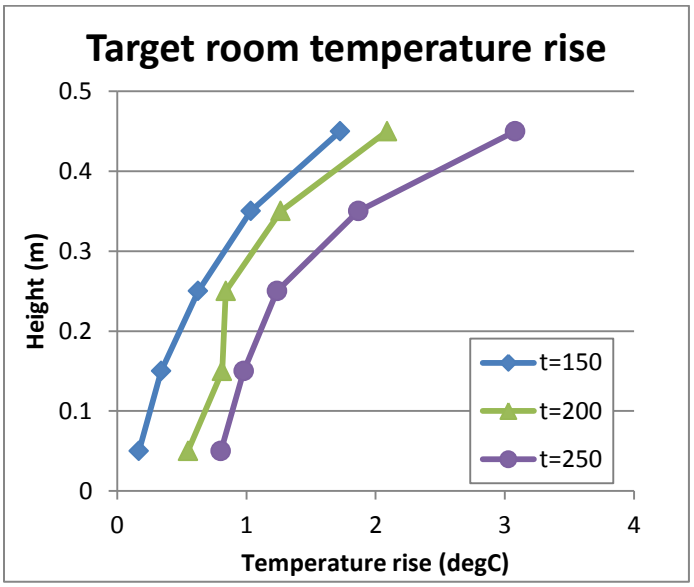

Fig 6.8 Target room temperature profiles at different time (HRR = 2.0 kW)

6.4.2 Case–B - change of opening

In addition to fire source HRR, the location and size of compartment openings also affect smoke transport, especially when the openings are near the fire source. These openings not only provide paths for smoke spread but also bring in additional air, which nurtures fire development. In closed compartments, or ones with very small openings, the fire becomes ventilation-controlled and limited by the quantity of oxygen available. In this experiment, the fire source always has a

sufficient oxygen supply, so the opening only affects the transport of hot gases.

Table 6.2 shows three experimental setups with different door locations, as illustrated in Fig 6.1. The results of average smoke temperature rise are shown in Fig 6.9. Because the fire room is well-ventilated, the locations of the openings have very little effect on the fire room smoke temperature. For corridor smoke temperature, represented by the red contour in Fig 6.9(b), Case 1 shows the highest temperature rise of all three cases. This is because Door 1 is located at the end of the corridor that is furthest from the fire room, and the hot gases that flow out of this opening have the lowest temperature. In other words, the total energy loss through the opening is relatively lower for Case 1. Overall, the results indicate that the door position has only a minor effect on the smoke temperature and smoke layer height. This may be due to the fact that the fire source is a Bunsen burner, and the flow rate change is relatively small comparing to the air supplied by the fire room floor opening.

Table 6.2 Door position for three case setups

	Door 1	Door 2	Door 3
Case 1	Open	Closed	Closed
Case 2	Closed	Open	Closed
Case 3	Open	Closed	Open at t = 180 s

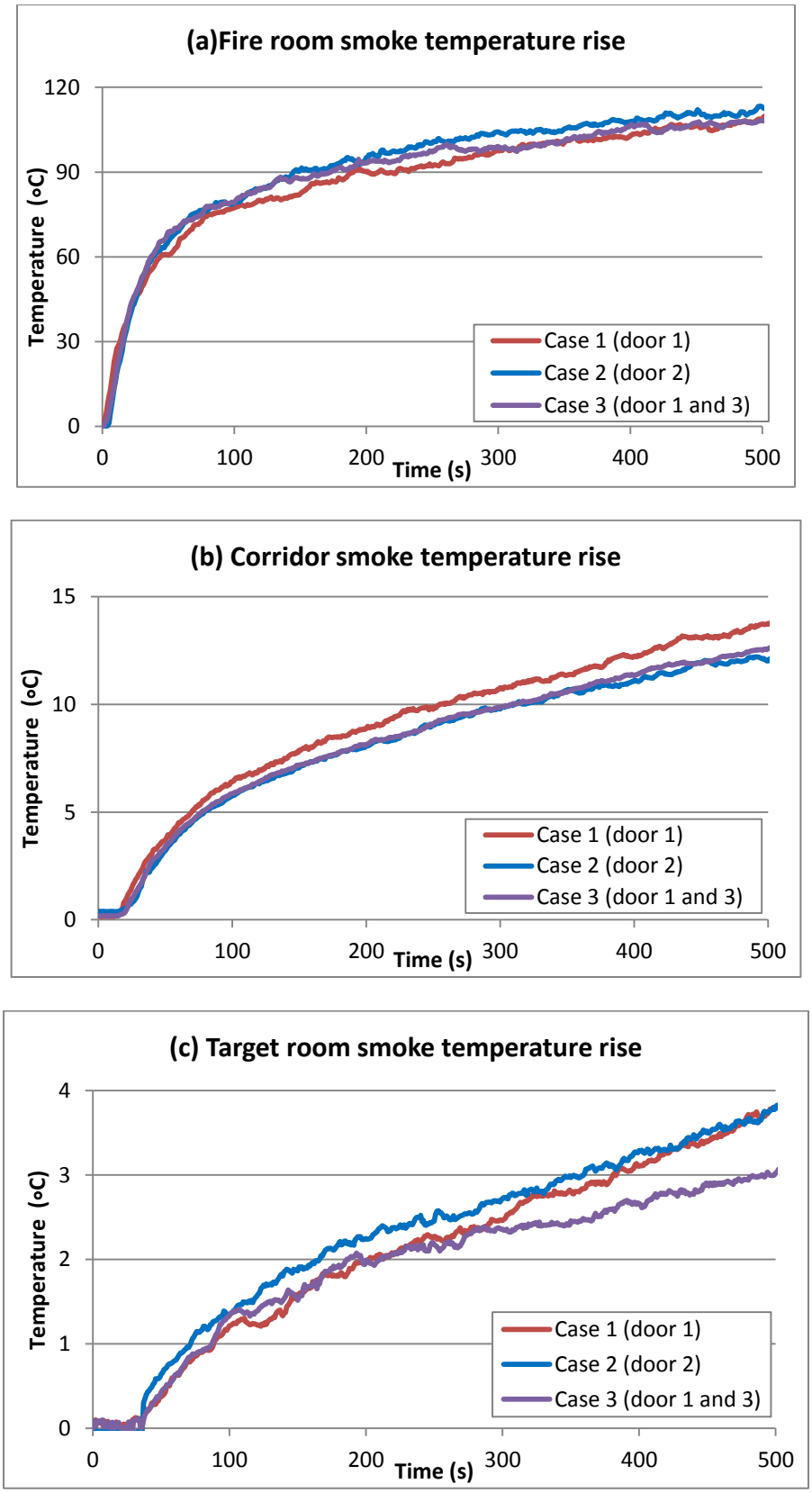

Fig 6.9 Comparisons of smoke temperature rise in three rooms for different door setups

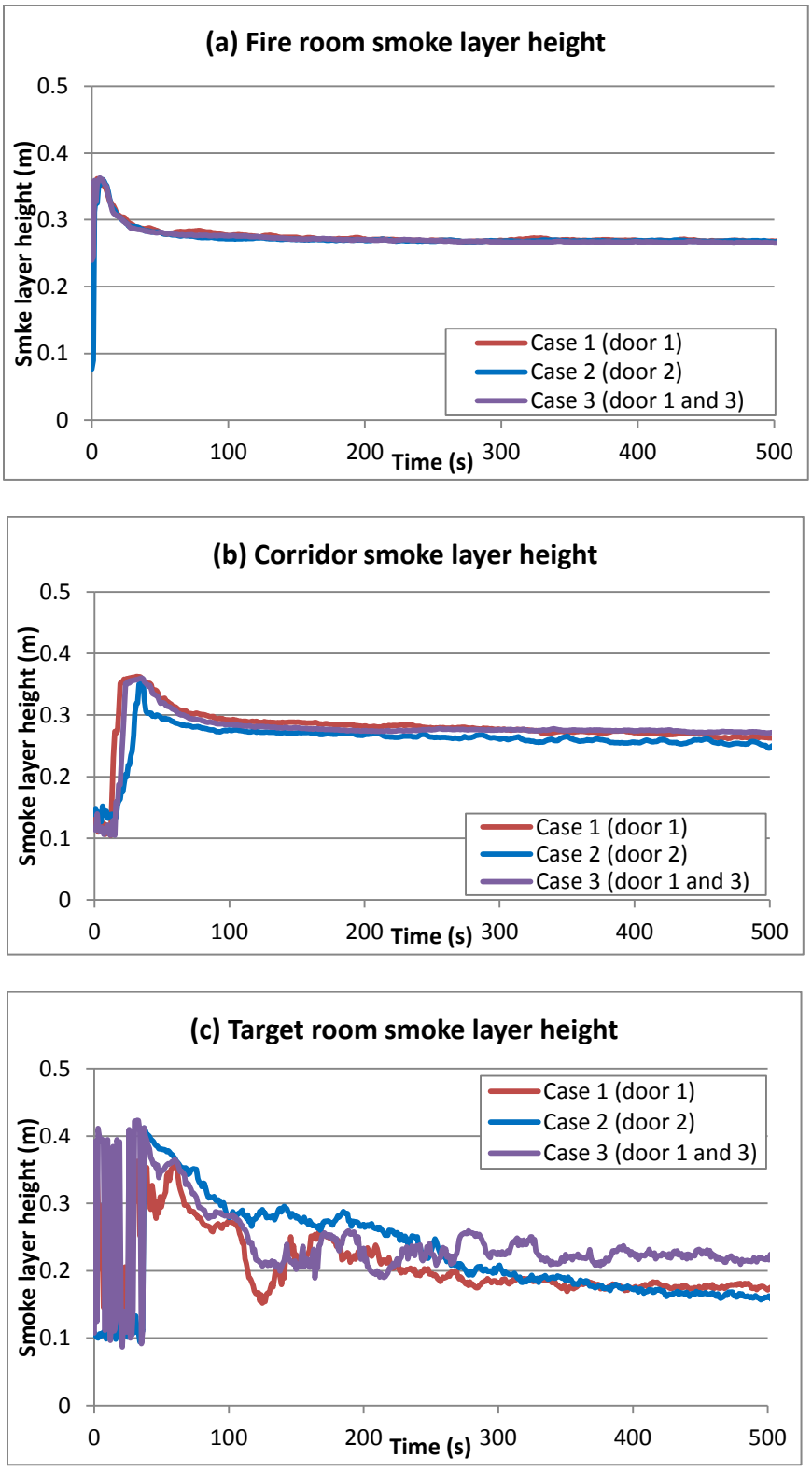

Fig 6.10 Comparisons of smoke layer height in three rooms for different door setups

References

Babrauskas, Vytenis, and Richard D. Peacock. "Heat release rate: the single most important variable in fire hazard." *Fire safety journal* 18, no. 3 (1992): 255-272.

Peacock, Richard D., Sanford Davis, and Billy T. Lee. *An experimental data set for the accuracy assessment of room fire models*. Center for Fire Research, 1988.

Peacock, R. D., and P. A. Reneke. "Verification and Validation of Selected Fire Models for Nuclear Power Plant Applications, Volume 5: Consolidated Fire Growth and Smoke Transport Model (CFAST)." *NUREG-1824, US Nuclear Regulatory Commission, Washington, DC* (2007).

Johansson, Nils. "Numerical experiments and compartment fires." *Fire Science Reviews* 3, no. 1 (2014): 1-12.

Babrauskas, Vytenis. "The generation of CO in bench-scale fire tests and the prediction for real-scale fires." *Fire and Materials* 19, no. 5 (1995): 205-213.

Babrauskas, Vytenis. "Sandwich panel performance in full-scale and bench-scale fire tests." *Fire and materials* 21, no. 2 (1997): 53-65.

Moodie, K., and S. F. Jagger. "The King's Cross fire: results and analysis from the scale model tests." *Fire Safety Journal* 18, no. 1 (1992): 83-103.

Jolly, Shashank, and Kl Saito. "Scale modeling of fires with emphasis on room flashover phenomenon." *Fire safety journal* 18, no. 2 (1992): 139-182.

Makhviladze, G. M., A. V. Shamshin, S. E. Yakush, and A. P. Zykov. "Experimental and numerical study of transient compartment fires. "*Combustion, Explosion and Shock Waves* 42, no. 6 (2006): 723-730.

Chapter 7 Forecasting Smoke Transport in Real-Time

The models presented in Chapters 5 and 6 focus on a posteriori estimation of model states and important parameters. In this chapter, the model is designed to be calibrated with a bench-scale fire experiment and to predict smoke transport using real-time measurements.

7.1 Potential problems and important EnKF model parameters

The performance of an EnKF model heavily depends on several important model parameters to determine simulation and observation error covariance and to further estimate the approximated true states of the system. These parameters also directly affect simulation accuracy and speed. In addition, when applied to a forecasting simulation of building environment, the determination of these parameters can be very different from that of other types of systems. This section discusses the potential problems that can arise when these EnKF model parameters are not properly defined, as well as possible solutions for overcoming these problems.

7.1.1 Localization and spurious correlation

In general, the physical states of two different locations that are near each another are usually highly correlated. In contrast, there is very little correlation between the physical states of two locations that are physically far away from each other; thus, such correlations are considered spurious. In other words, potential problems may arise when all observations are equally applied to an EnKF analysis. For a compartment fire scenario as presented in this chapter, the correlations between the observations and model states should take into account the flow rate between the rooms. To well illustrate the problems for the reader's convenience, we start again with the basic equations of EnKF.

$$\mathrm{X}^{a} = X^{f} + \mathrm{K}(y - H\overline{X^{f}}) \tag{7.1}$$

$$K = \frac{P^f H^T}{H P^f H^T + R} \tag{7.2}$$

If the spurious correlations are not considered when observing Eq. (7.1) and Eq. (7.2), the measurement innovation (difference between measurement and forecasted measurement) $y - H\overline{X^f}$ becomes equally important to any model state regardless of the distance between them because $HP^f H^T + R$ is constant for one specific measurement. This may cause a model state to be updated with an irrelevant observation even when the noise is much greater than the correlation (Hamill et al. 2001). To account for this issue, various measures, which are so-called "localization methods", are proposed based on modifying forecasted error covariance P^f and observation error covariance R in Eq. (7.2). For example, for the grid points that are far away from the observation location, the correlation becomes weaker where P^f should approach zero. This can also be interpreted that when K is approaching zero in Eq. (7.2), the optimal model states, X^a, in Eq. (7.1) are solely dependent on the forecasted states, X^f. Another method for achieving a similar effect is to increase the measurement error covariance, R. By increasing R when the distance is greater, the uncertainty of the measurement becomes higher, and the signal becomes relatively lower. Thus, when R increases, K approaches zero, which yields similar results to localizing P^f.

In order to formulate localization methods, Houtekamer and Mitchell (2001) introduced a distant-dependent reduction of background (simulation) error covariance method for an EnKF. The simulation error covariances are localized by applying a Schur-product based on a distant-dependent function where the Schur-product, ρ, for covariance localization is determined by:

$$\rho = -\frac{1}{4}d^5 + \frac{1}{2}d^4 + \frac{5}{8}d^3 - \frac{5}{3}d^2 + 1 \ \ for \ \ 0 \le d \le 1 \tag{7.3}$$

$$\rho = \frac{1}{12}d^5 - \frac{1}{2}d^4 + \frac{5}{8}d^3 + \frac{5}{3}d^2 - 5\mathrm{d} + 4 - \frac{2}{3}\cdot\frac{1}{d} \; for \;\; 1 \le d \le 2 \tag{7.4}$$

$$\rho = 0 \;\; for \;\; 2 \le d \tag{7.5}$$

$$\mathrm{d} = \frac{|z|}{c} \tag{7.6}$$

where z is the physical distance between model grid points or the distance between the observed location and a grid point, and c is the distance to scale the correlations between two nodes. The correlation is assumed to be 1.0 when the distance is below c and gradually reduced to 0 when the distance is increased to $2c$. For the smoke transport forecasting model presented in this chapter, c is determined by the average travel distance of hot smoke gases during a time period between two measurements. For example, the average velocity at the fire room door is 0.4 m/s (will be discussed in Section 7.1.3) with a 10-second sensor resolution. By applying Eq. (7.3) to Eq. (7.6), the localization factor from the fire room to the corridor is about 0.15. For a system with n model nodes and m observations, ρ is an n by m matrix, which is the same as the dimension of K. Therefore, the Kalman gain can be improved by the Schur-product where

$$\mathrm{K}_e = \frac{(\rho \circ P^f)H^T}{H(\rho \circ P^f)H^T + R} \tag{7.7}$$

Fig 7.1 shows a comparison of the smoke layer height prediction in the target room using two different EnKF models. All input parameters are identical except that one case uses improved Kalman gain by applying the localization method as shown by Eq. (7.7), while the other uses unimproved Kalman gain. As shown by the dotted orange line, the observation is given from $\mathrm{t} = 10$ to $\mathrm{t} = 100$ seconds to update model states. Although local measurements are also given, the results still show high deviations between the EnKF outputs and the measurements. This is because the EnKF over-predicts the error covariance between the predicted target room smoke layer height and the measurements from rooms far away. These correlations are supposed to be

weakly correlated due to their long distances but are mistaken as highly correlated in this case. These spurious correlations update target room smoke layer height inaccurately. Since the posteriori estimations of the target room smoke layer height are not successful in this case, the predicted smoke layer height from $t = 100$ to $t = 500$ seconds, as shown by the solid-orange line, is also very different from the experiment results and even worse than direct simulation using the zone model. By applying the aforementioned localization methods, as shown by the purple contour, the model reasonably performs posteriori estimation and also predicts the smoke layer height from t = 100 seconds and t = 500 seconds with noticeable accuracy.

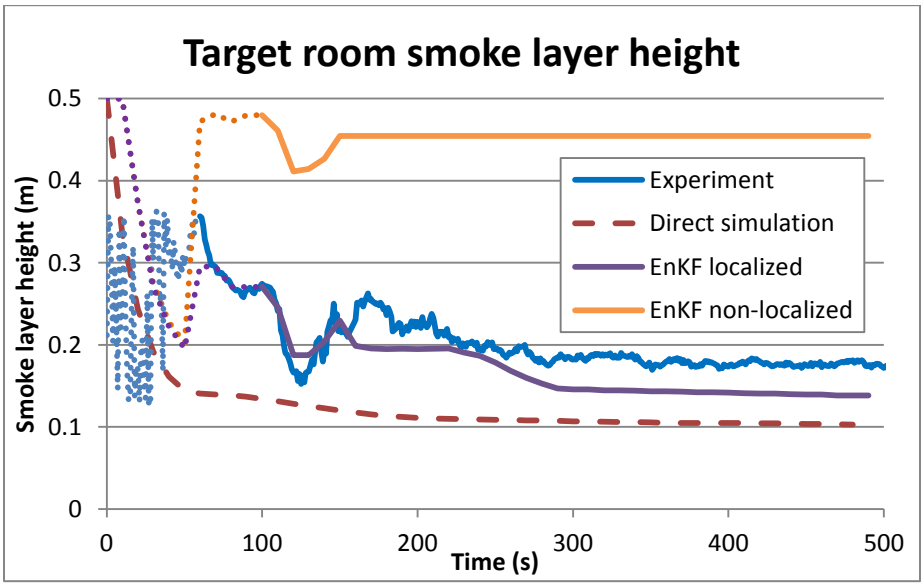

Fig 7.1 Comparison of EnKF results using localized and non-localized Kalman gain

7.1.2 Filter divergence

As mentioned in the previous section, the accuracy of an EnKF model is based on the estimation of simulation and observation covariances using a limited number of ensemble members. When the EnKF parameters are not appropriately defined, the model may have difficulty determining analysis states (approximate true states), which causes filer divergence. A very commonly found problem that causes filter divergence is when the perturbation range of the ensemble members

does not cover the true state of the system. As illustrated by Fig 7.2, when the true state acts like one of the ensemble members, the sampling strategy is considered good because the error of the model parameter can be determined and used to improve the model. However, when the true state is not included in the ensemble perturbation range, the model may have difficulty determining a proper value since all ensemble members are incorrect.

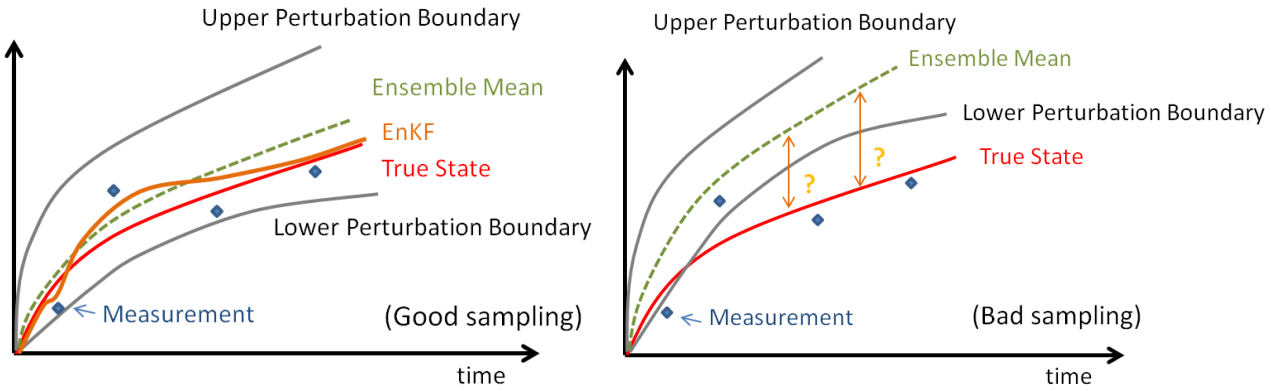

Fig 7.2 Illustrations of ensemble sampling strategies

There are several possible solutions for ensuring the ensemble perturbations covering the true state. The first method is to increase the number of ensemble members to enlarge the perturbation range. Since the perturbation of initial parameters is normally distributed, increasing the number of ensemble members will likely widen the upper and lower perturbation boundaries. However, this method is considered computationally intensive and inefficient when applied to a high dimensional system (when the number of model states, n, is much greater than the number of ensemble members, q).

The second method is to perturb the initial states of the simulation model to increase the range of ensemble member outputs. This method only works for cases with a high accuracy simulation model. For the simulation models with lower accuracy and higher systematic errors (higher bias), filter divergence will still occur when the simulation progresses over time and all ensemble members are going in the wrong direction, as shown in Fig 7.2. In this case, it is suggested to

apply the third method by adding a zero-mean white noise to the simulation model at every analysis cycle to provide more spread to the ensemble members. This method is especially suitable for mass transport problems when the model nodes are far away from the source location. This is due to the model states are nearly identical for all ensemble members at these far-away nodes in the early stage of simulation. The major drawback of this method is that more ensemble members are required to compensate for the additional white noises in order obtain accurate simulation error covariance. As a result, the additional numerical operations required to process ensemble members in EnKF analysis cycles directly affect computational time and are especially critical for systems that are designed to perform forecasting in real time. Therefore, the forth method can be applied to avoid filter divergence is setting up a threshold or a switch to start EnKF analysis. For example, in the case of a compartment fire, this can be a certain degree of increase in temperature rise detected from near-ceiling thermocouples. For instance, at the early stage of the fire, when there are no hot gases entering the rooms located far away from the fire source, the measurements taken from those sensors located in faraway rooms are still at the same initial ambient temperature. Thus, it is not necessary to process Kalman gain and update the model states. By setting up a threshold, the EnKF model not only avoids filter divergence but also bypasses unnecessary numerical operations.

In order to select an appropriate method for overcoming filter divergence problems, it is suggested that one use current available measurements to do a posteriori estimation and evaluate the discrepancies between the direct simulation results and the measurements. Based on general estimations of errors for each parameter, the parameters to be perturbed can be selected, and the magnitude of the perturbation can also be generally determined.

7.1.3 Determination of measurement uncertainties R

Measurement uncertainties are expected errors of the measurements obtained from the apparatus, so the uncertainties are either from the device itself or the interpretation of an indirect measurement. The measurements that are used in the EnKF analysis in this chapter are obtained from the experiment presented in Chapter 6. The thermocouples and data logger are calibrated before each set of experiments and are, therefore, considered highly accurate. In addition, the measurements obtained from repeating bench-scale experiments in the previous chapter show very minor deviations and are thus considered precise. By excluding the possible errors from the experiment apparatus, the uncertainties of the measurements are mostly dependent on zonal deviations. Because the smoke temperature and smoke layer height of a given room are calculated from the measurements of one thermocouple tree where the zonal deviations are excluded, they can be considered as indirect measurements. In general, the hot gases inside a room can deviate significantly depending on the location, especially in the early stage of fire. As illustrated by Fig 7.3, the zonal deviation of the gas temperature near the ceiling can be up to 20 °C in this case. In order to determine the uncertainties, an FDS model is employed, using the bench-scale experiment setups as inputs, and R is approximated by the FDS outputs. For example, the smoke layer height uncertainties in the fire room are 10% of the room height, and the temperature uncertainties are 10% of the average smoke temperature rise in the early stage (i.e., first 30 seconds); then, both decrease to 5% when the hot gas layer is well-developed. The measurement uncertainties of the corridor are assumed to be 20% in the early stage and 10% later on due to its larger size and higher zonal deviation. These uncertainties are considered independent, so the error covariances among different locations are assumed to be zero.

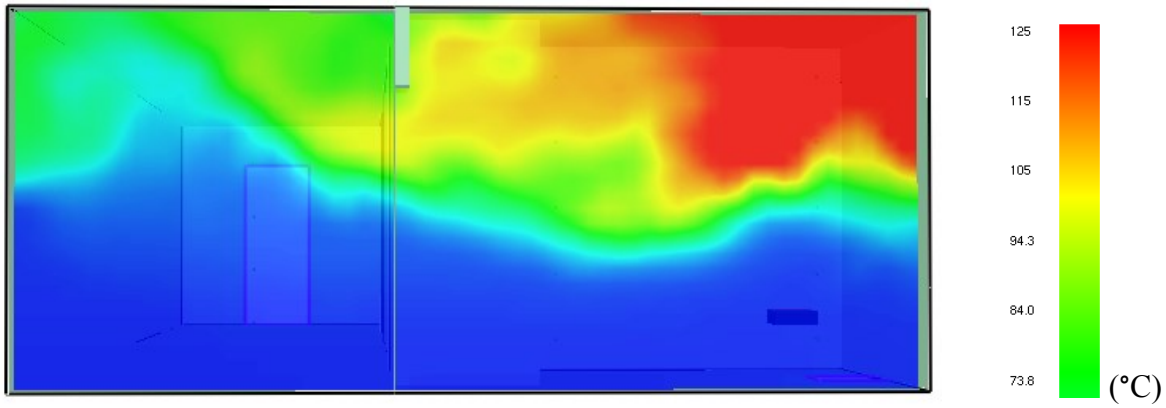

Fig 7.3 Zonal temperature distribution of the fire room from FDS results

7.1.4 Ensemble perturbation strategies

The major advantage of using EnKF to forecast building environment is that the important model parameters can be adjusted when measurements are available. By using more accurate model parameters, the predicted physical conditions can maintain at a desired accuracy in a longer time window. Therefore, in order to have an efficient EnKF model, it is important to select the parameters to be perturbed and design the magnitude of perturbation.

The most important parameter for a zone model simulation is HRR of the fire source. Since the flow rate of the fire plume is also based on a sub model using HRR as input, HRR directly affects both energy and mass conservation equation which makes it the most important parameter that determines model accuracy. Another parameter that determines the accuracy of the zone model is the door flow rate. As mentioned in Chapters 5 and 6, the main reason that a zone model fails to predict smoke transport to rooms distant from the fire source is the accumulating errors of the door flow rates. Therefore, it is suggested to add a new parameter to adjust flow rate at the corridor door. Detailed discussions are included in Chapter 5 so it is not presented here to avoid repetition.

In previous chapter, the inspection of the smoke layer height is based on injecting artificial

smoke and projecting laser sheets to visualize the hot gases layer. The visualized smoke layer height is close to the results interpreted from temperature measurements and also FDS simulation results. In this chapter, a detailed analysis of flow field is required to determine the uncertainties of the zone model flow rates. An initial test of using artificial smoke as seeder in a particle image velocimetry (PIV) system is conducted. The result shows that the lower layer does not have sufficient seeders for flow field visualization due to the buoyancy of the hot gases as show in Fig 7.4. In this case, the injected seeder is replaced by aluminum oxide powder (Al_2O_3). Although the particles of aluminum oxide powder are with small size (10 μm or smaller), the images obtained from PIV system are showing promising results where the particles are distributed all over the compartment as shown in Fig 7.5.

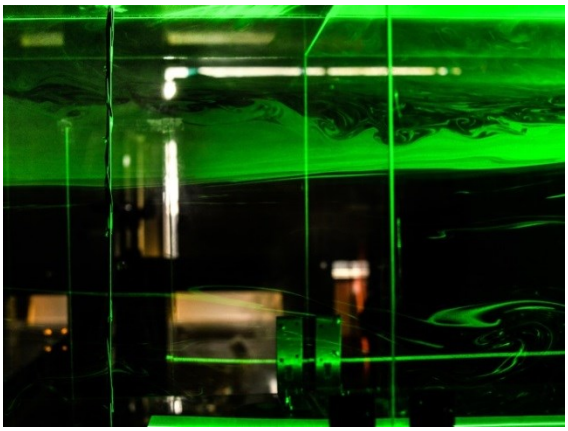

Fig 7.4 Flow field visualization using artificial smoke

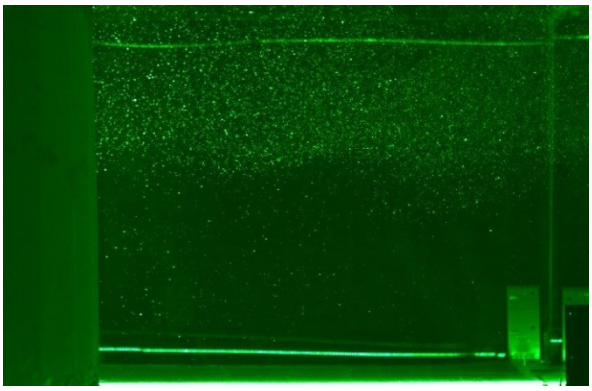

Fig 7.5 Flow field visualization using aluminum oxide powder (Al_2O_3)

From the experience gained from Chapter 5, the uncertainties of mass flow rate through doors should be included in the ensemble perturbation. Therefore, the PIV tests are conducted at the center line of the fire room door to estimate the average mass flow rate. As shown in Fig 7.6, the flow direction changes rapidly due to the turbulence near the door. In addition, the results are showing high deviations when repeating the same test setups. In order to obtain an average flow velocity, it can be achieved by either recording images from multiple planes altogether or repeating the test and photographing different planes. However, the small door size does not allow the prior method because the laser sheets are too close to each other so the particle images can be noisy. The latter method is also not reliable since the unstable flow direction. Therefore, the PIV tests are conducted near the center of the corridor where the flow pattern is more stable and can be easily analyzed. Following are the general experiment setups of the PIV system.

(a) Seeding

The seeding particles are based on ceramic material Al_2O_3 which are injected near the burner and the corridor section. The advantage of using Al_2O_3 over artificial smoke is its endurance to high gas temperature such as the heat generated by the propane burner. The diameter of the particle is less than 10 μm and the density is around $4g/cm^3$. The seeding process is based on global seeding method (Melling 1997) because the hot gas flow rate from the fire room to the corridor is relatively high and the corridor can be well-seeded in the early stage of fire. In order to inject the particles in a more stable flow rate, the seeders and air are pre-mixed in a special seeding chamber (30 cm x 30 cm x 30 cm, 3mm-thick acrylic) before entering the experiment compartments. The angle of the injection is adjusted to avoid interferences to the burner and the corridor flow field.

(b) Laser

The projected laser for particle visualization is based on a Nd:YAG laser machine (Newwave solo) which can perform 15-200 mJ output at 532 nm. The laser is projected through a cylindral lens attached in front of the laser beam while the projected laser is converted to a sheet to illuminate the plane of interest for particle visualization. The frequency of the laser pulses is adjusted by the software Flowmanager© according to the rate of images are captured by the digital camera.

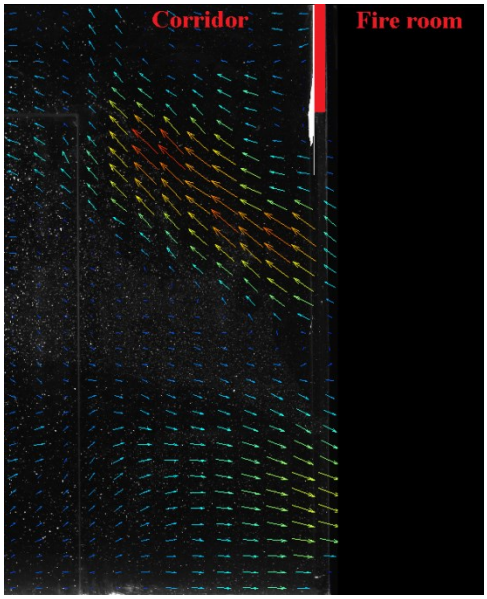

Fig 7.6 Flow velocity field at fire room door from PIV results

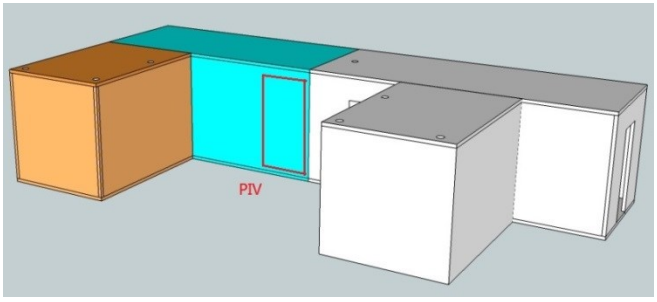

Fig 7.7 Location for images taken for PIV analysis

(c) Camera

The images of illuminated particles are captured by a fast speed CCD digital camera using Nikkor 35mm F2 lens. The calibration are also based on Flowmanager© including the adjustment of lens focus and length scale of the image to pixels.

(d) Image process

The images taken from the camera are divided into multiple integration areas (32 by 32 or 64 by 64) where the size of each integration area should be greater than 1/4 of the particle travel distance during an image capturing time interval. The resulting images are first processed by cross-correlations and average filtering. Finally, the detailed statistics of all vectors of the flow field can be generated.

Fig 7.8 shows a comparison between the flow fields of FDS and of PIV. The length of the vectors illustrates the flow velocity at different location. Both flow fields are separated into two zones where the upper part is a hot gas zone with its flow direction to the right and the lower part is a cold air zone with its flow direction to the left. Two zones are separated by the red lines where the air velocity is assumed zero. It can be observed that FDS outputs have a smaller hot gas zone but the velocity is relatively higher. By multiplying the cross-section areas for both cases, the volume flow rates are very close for both cases. Thus, the flow rates in the experiment may be approximated by the FDS results including the door flow rate. Finally, the uncertainties of the zone model flow rate are approximated by comparing zone model and FDS results.

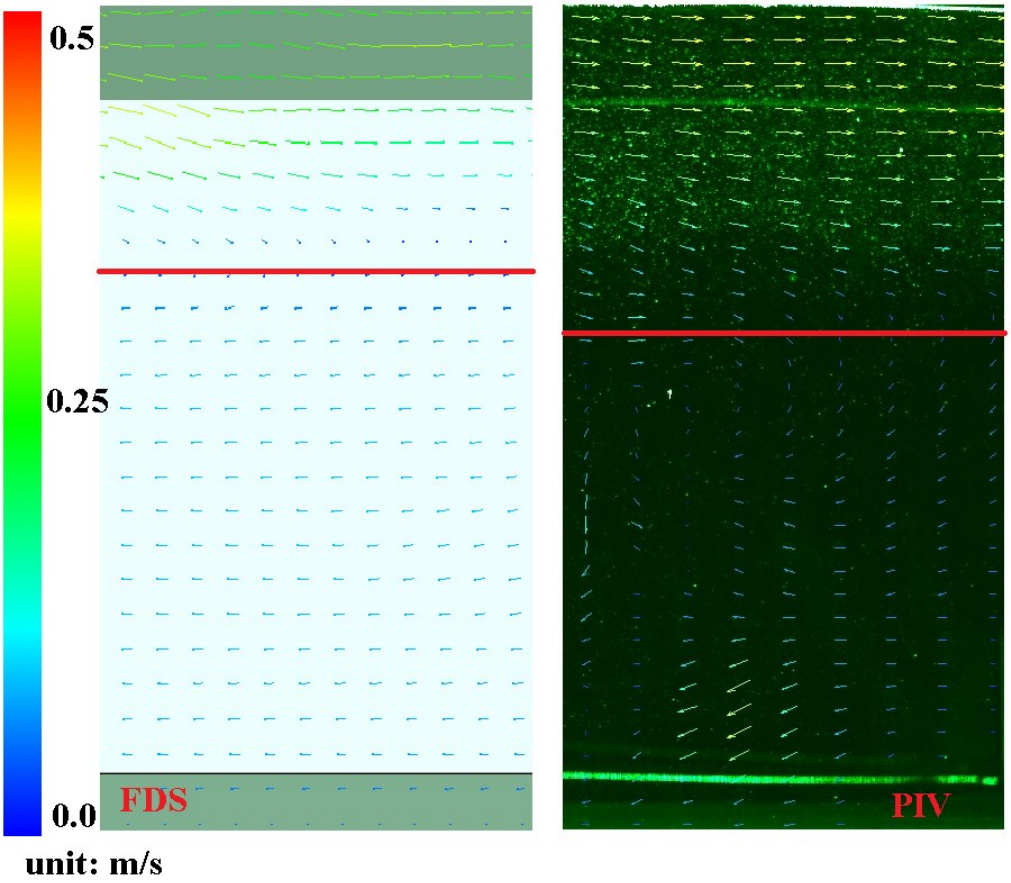

Fig 7.8 Comparisons of flow velocity field at t = 20 seconds

The perturbations of HRR and mass flow rate through corridor opening are based on the Gaussian distribution where the expected value and standard deviations are prescribed in the EnKF model. Fig 7.10 shows an example of HRR perturbation using the Gaussian distribution where 68% of the ensemble members are expected to be within the range of $Q_f \pm \sigma$ where Q_f is 2.0 kW and σ is 0.75 kW. Similar method is also applied to the perturbation of mass flow rate through the corridor opening where σ is 0.01 kg/s which is approximated by the comparisons of zone model and FDS results. This is due to the flow field at the door is relatively more noisy in PIV outputs so the reference flow rates are based on FDS results.

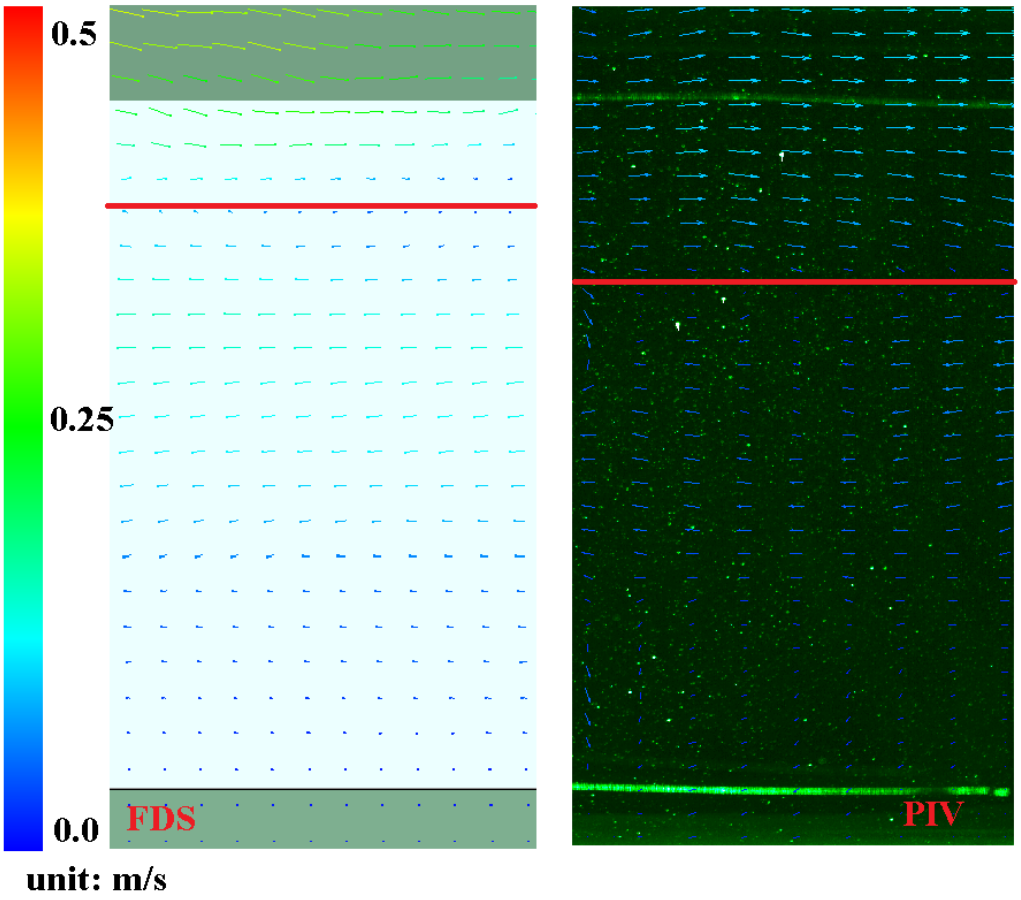

Fig 7.9 Comparisons of flow velocity field at t = 70 seconds

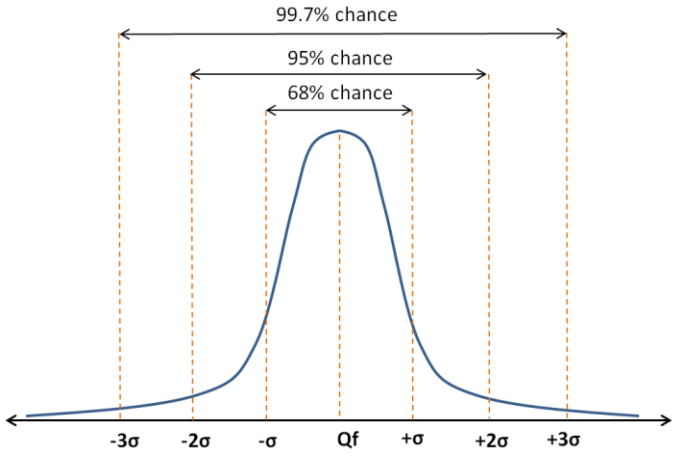

Fig 7.10 Probability distribution of HRR perturbation based on the Gaussian distribution

7.1.5 Number of ensemble members

To achieve real-time prediction, the time for processing one EnKF analysis cycle should be shorter than the time period between two available measurements. In general, more than 80% of the computational time of EnKF numerical operations relates to processing ensemble members. Therefore, the number of ensemble members is the most important parameter in balancing the model accuracy and simulation speed.

Fig 7.11 shows the comparisons of forecasting errors using different numbers of ensemble members when the measurements are provided for the first 100 seconds with 10-second time intervals. The blue contour with triangle (200-second forecast) means the model predicts the smoke transport for 200 seconds after the measurements stop being provided. The y-axis (RMSE %) is the average root mean square error (RMSE) of the forecasted smoke temperature divided by the average smoke temperature.

The values presented in the figure are the average of seven simulations, while the cases with the highest and lowest RMSE are excluded. It can be observed that the RMSE % decreases drastically when the number of ensemble members increases from 5 to 20 for both, 200-second and 400-second, cases. After that, the results show no significant improvement in the predictability of smoke temperature. Similar results can be found in Fig 7.11(b) for the forecasted error of the smoke layer height from q = 5 to q = 20. But, the RMSE % keeps decreasing when q increases from 20 to 40, which indicates that the model with 40 ensemble members performs better at predicting smoke layer height in this specific case.

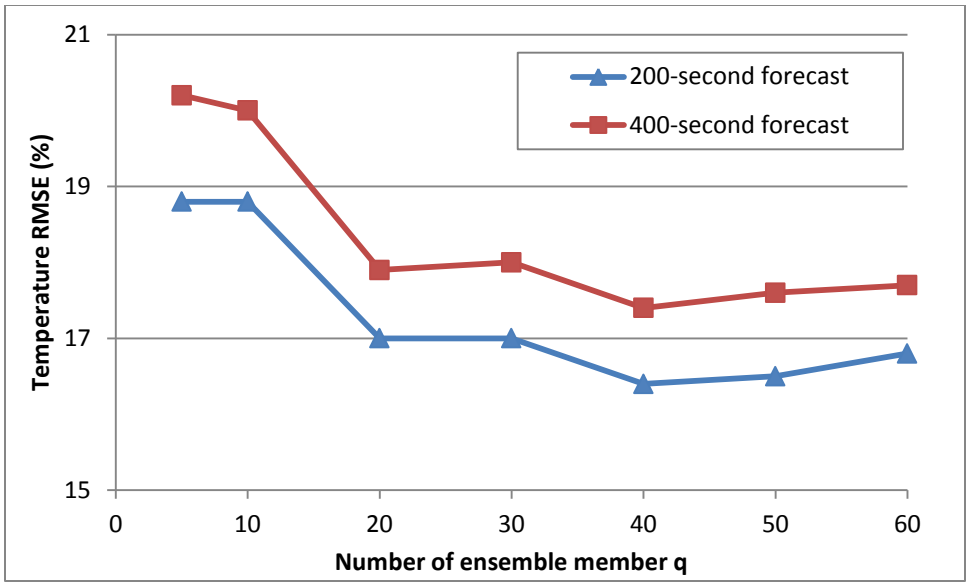

Fig 7.11(a) Comparisons of temperature forecasting error using different numbers of q

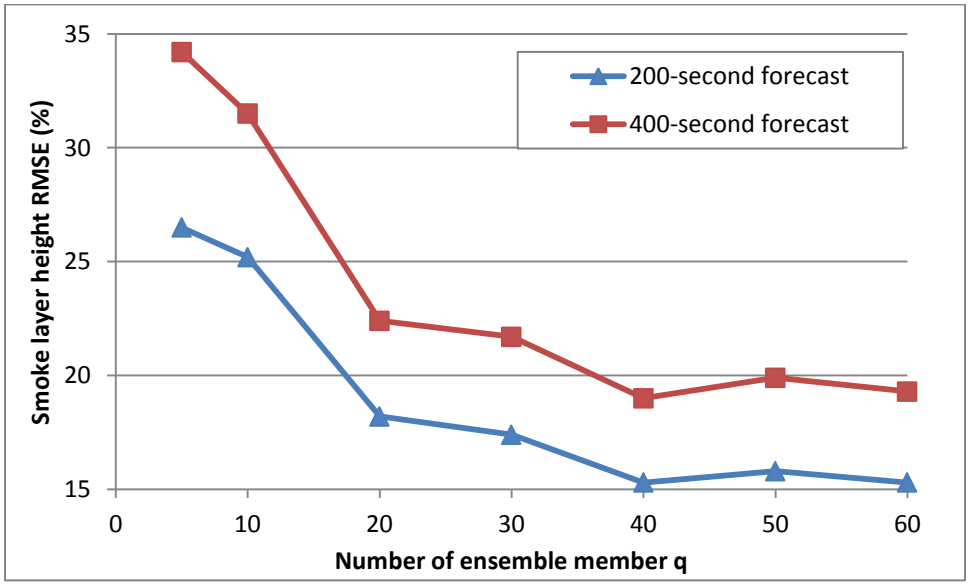

Fig 7.11(b) Comparisons of smoke layer height forecasting error using different numbers of q

*RMSE% is defined as RMSE divided by the mean

To process 100-second available measurements and forecast smoke transport for 400 seconds, this model requires about seven seconds of computational time, which is less than the measurement time interval of 10 seconds. Therefore, 40 ensemble members can be considered an optimal number for balancing forecast accuracy and CPU time, while achieving the goal of real-

time forecasting.

Compared to the model presented in Chapter 5, this model requires a lesser number of ensemble members to achieve desirable predictability in forecasting smoke transport. This is because previous models are based on existing tools – CFAST 6.3 and OpenDA 1.1, making it more difficult to implement localization methods. The spread of ensemble member outputs is based on adding white noises; thus, more ensemble members are required to achieve similar predictability.

7.2 Forecasting smoke transport in a compartment fire

This section includes two different types of forecasting. The first type is forecasting a compartment fire with constant HRR, and the second type is with non-constant HRR. The model parameters are tested with a set of 2 kW HRR experiment results that show noticeable predictability. After that, the model is directly applied to forecast other cases with different observation data using exactly the same model parameters.

7.2.1 Forecasting smoke transport with constant HRR source

Case A – 1.5 kW fire

The first case is based on a 1.5 kW fire, in which observations are given every 10 seconds. In order to test the predictability of the EnKF model, three different tests are conducted, wherein the measurements are provided for the first 50, 100 and 150 seconds respectively. As shown in Fig 7.12, the red dashed lines are the results of direct simulation using a zone model and the blue solid lines are the experiment results. It can be observed that the zone model over-predicts smoke temperature in all three rooms, especially in the early stage of a fire. This may be because the lower layer is considered adiabatic in the model assumption, so the total energy entering the upper layer is over-estimated, resulting in high temperatures. This effect is especially noticeable

in the early stage of the fire since the lower layer volume is much greater than the upper layer. After applying the EnKF model, the posteriori estimations of the smoke temperature and smoke layer height (represented by dotted lines) are adjusted based on available measurements in the EnKF analysis. At the same time, the perturbed model parameters (i.e., HRR and door flow rate) are also estimated and used to forecast smoke transport. For example, the solid green line in Fig 7.12(f) shows the forecasted smoke layer height in the target room. When the measurements stop being provided, at t = 50 seconds, measurements from the fire room and the corridor are used, and the forecasted smoke layer height shows minor improvement since the local measurements in the target room are still noisy. In addition, the updated HRR and flow rate estimations help improve forecasting simulation results when measurements are not available. Following the same procedures when measurements are provided up to t = 100 seconds, as indicated by the purple dotted line, the posteriori estimation shows significant improvement when local measurements are available. After t = 100 seconds, when the measurements become unavailable, the forecasted smoke layer height still maintains reasonable accuracy, and finally, at t = 150 seconds, when more measurements are available, the model accurately predicts the smoke layer height in a longer time window because the model parameters have been corrected.

When comparing the forecasted smoke temperature and smoke layer height in different rooms, the results in the corridor show greater discrepancy between the forecasted states and the measurements. This is because the volume of the corridor is much greater than that of the other two rooms; thus, a higher measurement error as discussed in Section 7.13, is assigned to R to account for zonal deviation. When measurement uncertainties of the corridor are taken into account, the predicted smoke layer height and smoke temperature are still within a reasonable range as defined by R.

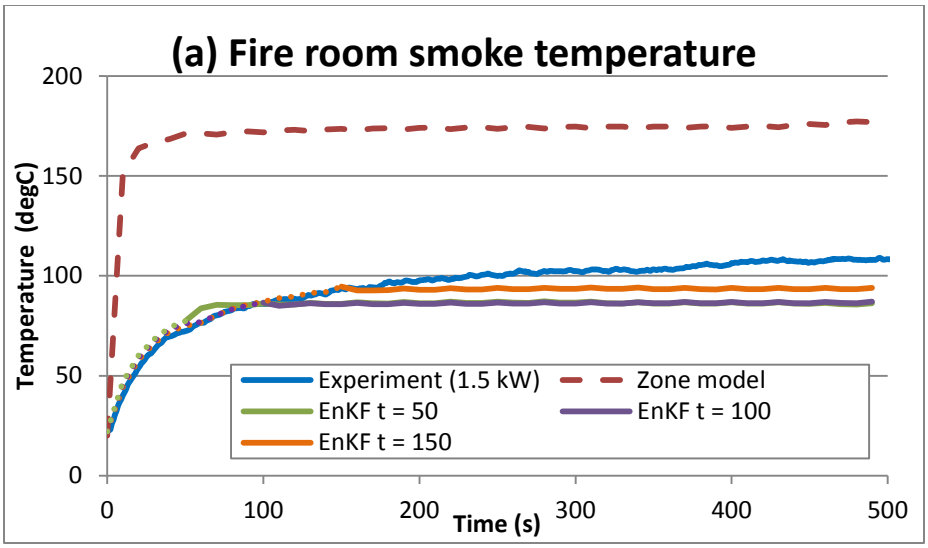
(a) Fire room smoke temperature
Temperature (degC)
Time (s)
Experiment (1.5 kW)
Zone model
EnKF t = 50
EnKF t = 100
EnKF t = 150

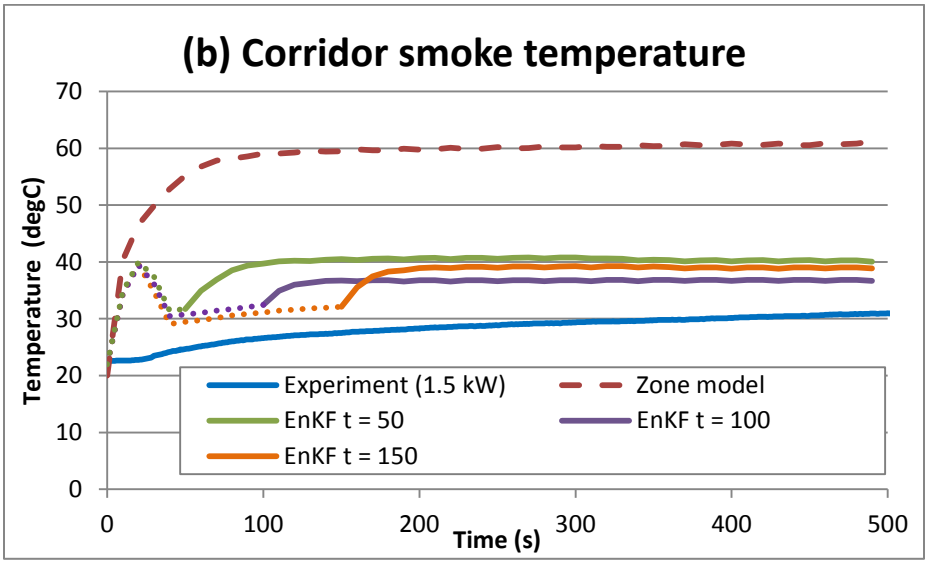
(b) Corridor smoke temperature
Temperature (degC)
Time (s)
Experiment (1.5 kW)
Zone model
EnKF t = 50
EnKF t = 100
EnKF t = 150

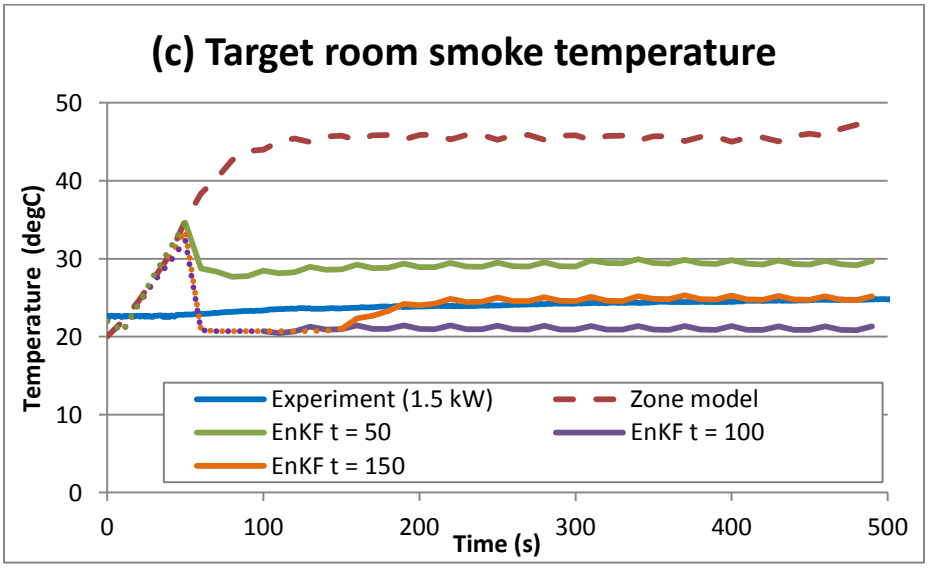
(c) Target room smoke temperature
Temperature (degC)
Time (s)
Experiment (1.5 kW)
Zone model
EnKF t = 50
EnKF t = 100
EnKF t = 150

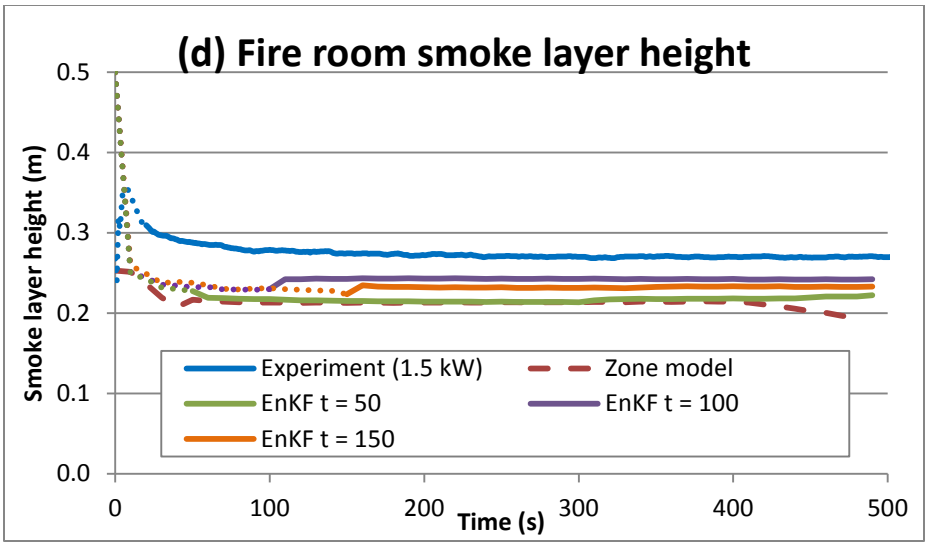

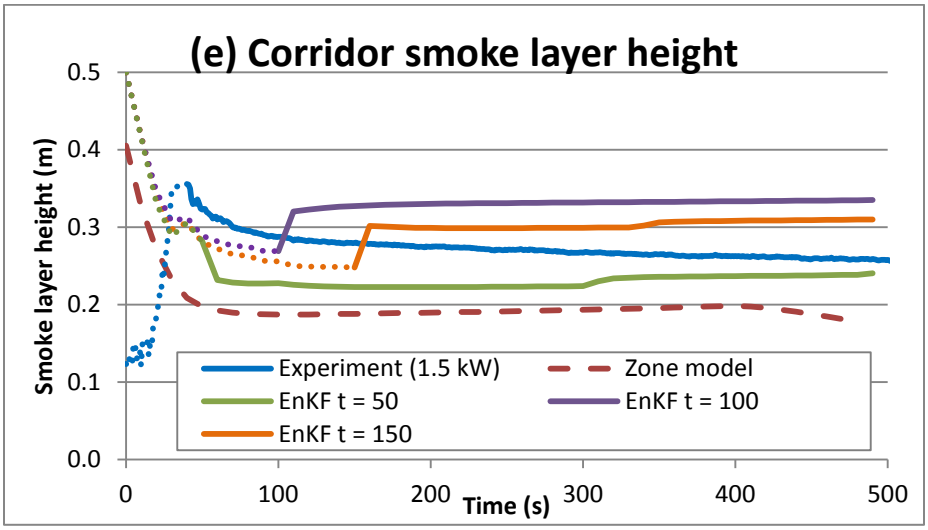

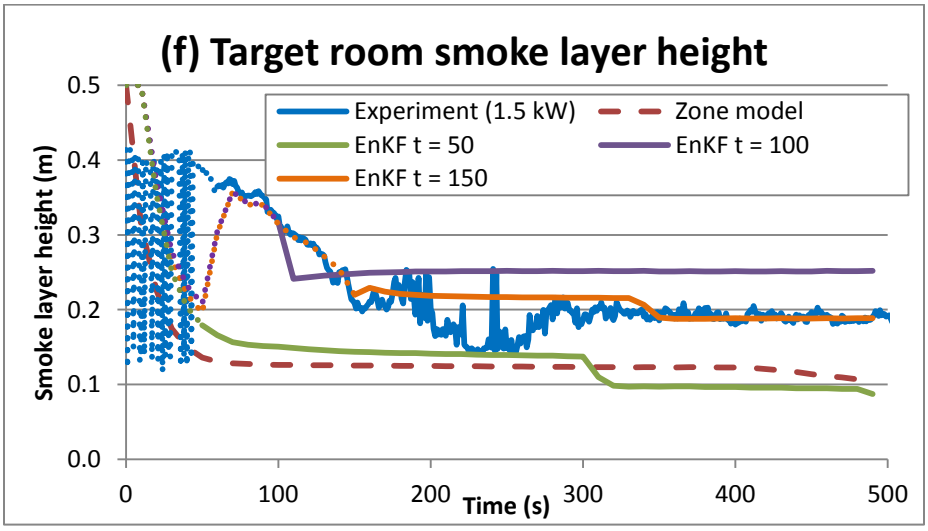

Fig 7.12 (a) to (f) Predictability of the EnKF model during a 1.5 kW fire

Case B – 2.78 kW fire

The second case is based on another set of measurements obtained from a 2.78 kW fire test. As discussed in Chapter 6, the temperature rise in each room is significantly higher than that of a 1.5 kW fire case. Although the model inputs are exactly the same as the previous model, the EnKF can still update model parameters and perform reasonable predictions. As simulation progresses and more measurements become available, the results show more accurate predictions since the model parameters and model states are updated as shown in Fig 7.13.

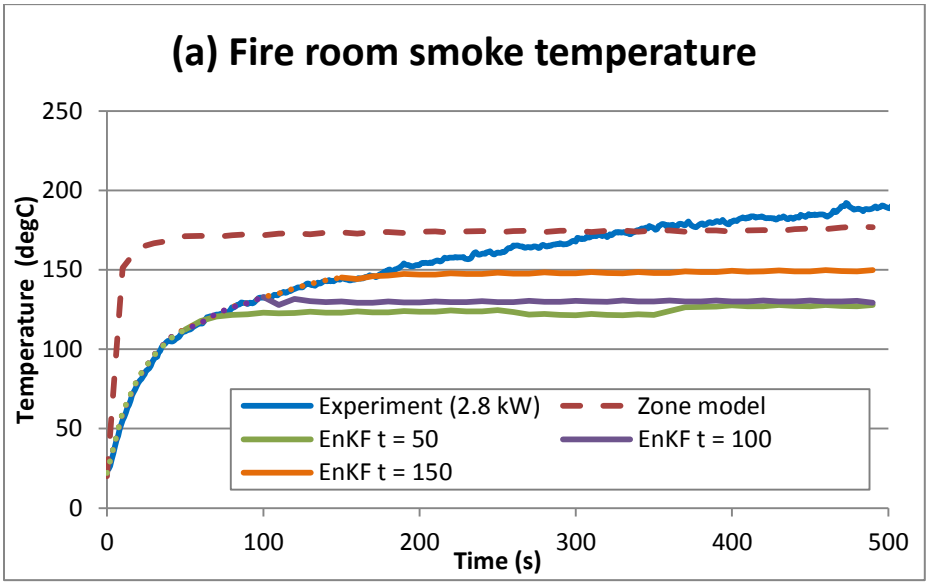

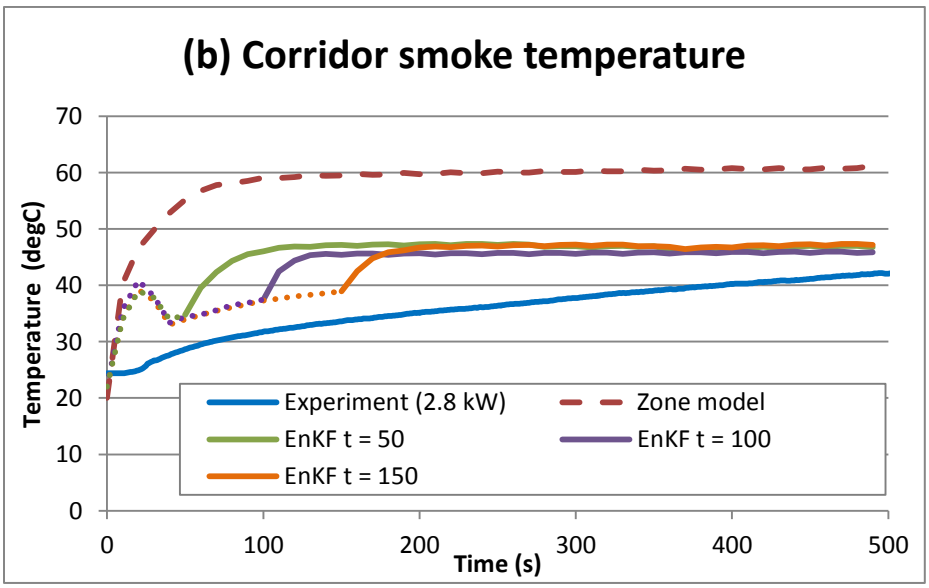

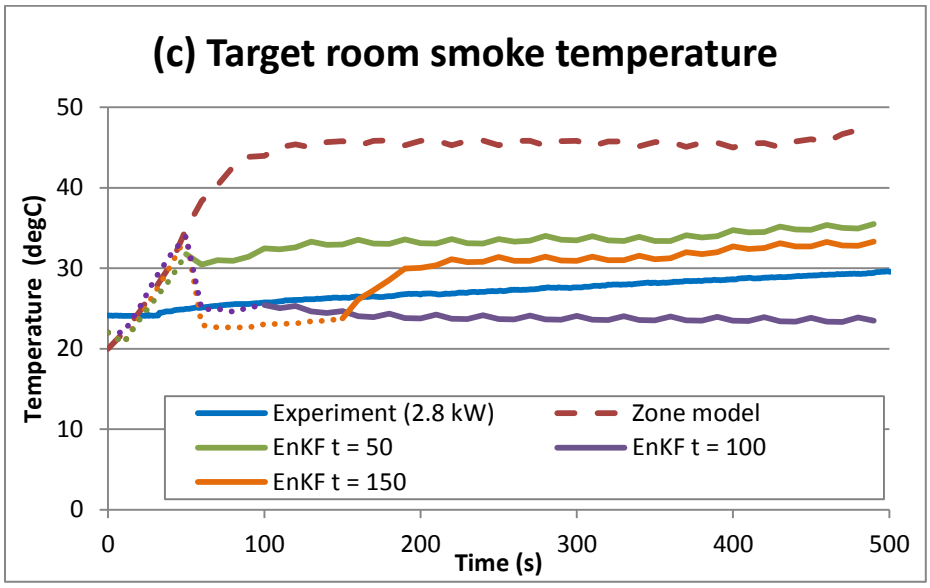
(c) Target room smoke temperature
Temperature (degC)
50
40
30
20
10
0
0
100
200
300
400
500
Time (s)
Experiment (2.8 kW)
Zone model
EnKF t = 50
EnKF t = 100
EnKF t = 150

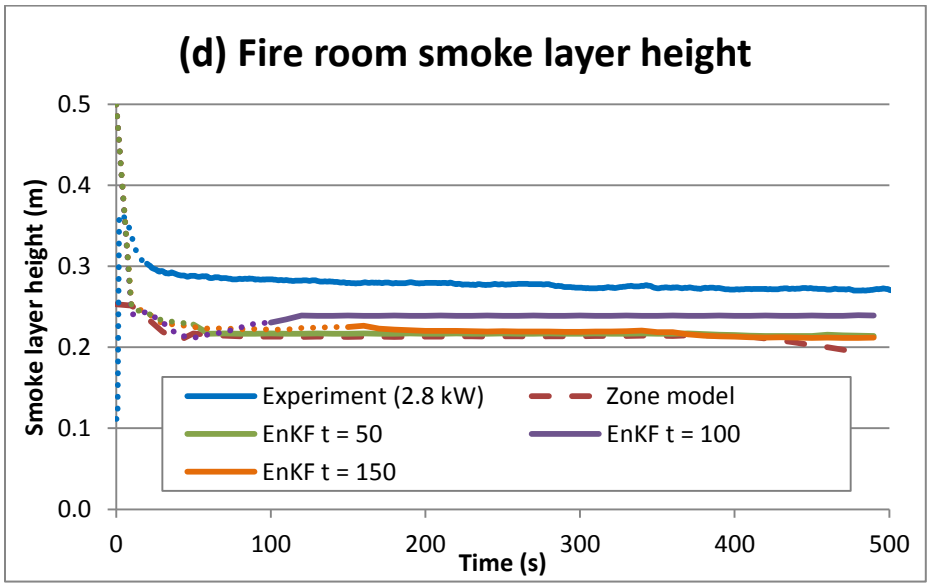
(d) Fire room smoke layer height
Smoke layer height (m)
0.5
0.4
0.3
0.2
0.1
0.0
0
100
200
300
400
500
Time (s)
Experiment (2.8 kW)
Zone model
EnKF t = 50
EnKF t = 100
EnKF t = 150

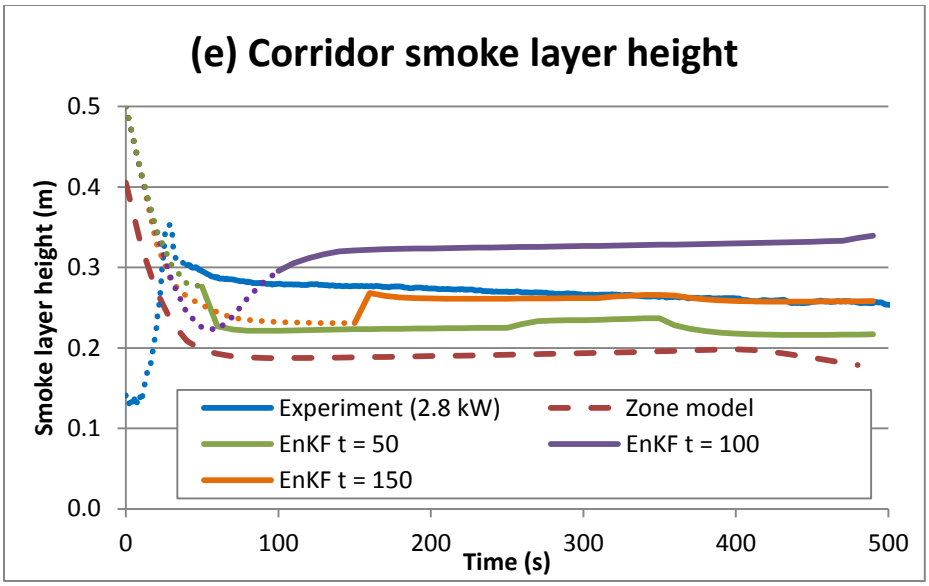

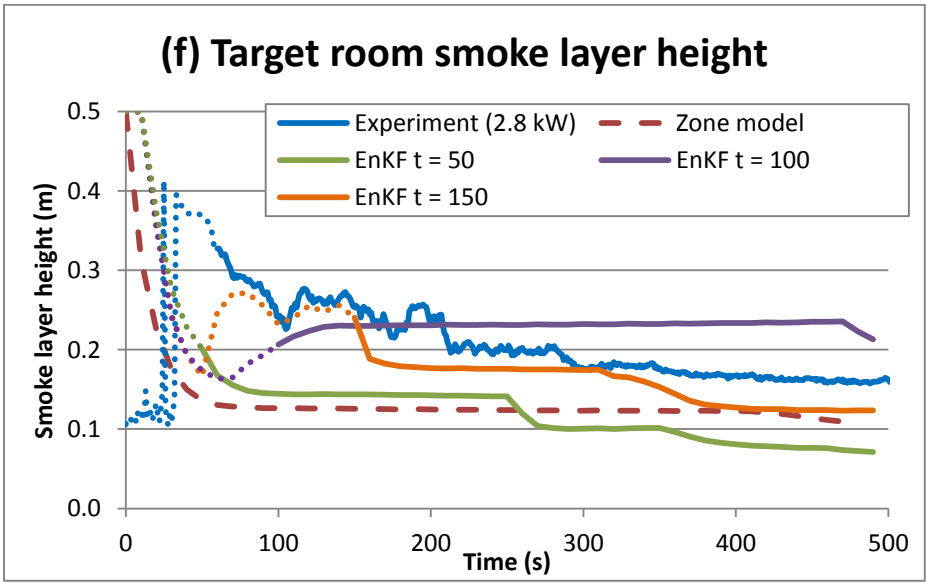

Fig 7.13 (a) to (f) Predictability of the EnKF model during a 2.78 kW fire

7.2.2 Forecasting smoke transport with non-constant HRR

The model presented in the previous section verifies the predictability of constant HRR cases and shows promising results. In this section, the scope is extended to forecasting non-constant HRR cases. All EnKF model parameters are the same as in previous cases, except for the HRR perturbation method. In the previous section, the perturbation of HRR gives each ensemble member only one HRR value for all time steps because the measurements are based on a

constant fire. But, for a transient HRR case presented in this section, the HRR is perturbed at each time step in order to account for HRR change.

For the experiment setups, the initial HRR is 1.5 kW and changes to 2.78 kW at t = 180 seconds. As illustrated by the solid-blue line in Fig 7.14(a), the smoke temperature measurements in the fire room drastically change at around t = 190 seconds due to the change of HRR. Similar effects can be found in the corridor and the target room, as presented by Fig 7.14(b) and (c), with a certain time delay as discussed in previous chapters. At t = 150, the smoke temperature forecasted by the EnKF, as illustrated by the solid purple line, is still based on the measurements obtained from 1.5 kW HRR, so the forecasted smoke temperature does not show significant change at t = 190 seconds. At t = 200 seconds, the measurements of the 2.78 kW fire become available and the parameters are adjusted accordingly in the EnKF analysis. As shown by the solid green line, the predicted smoke temperature drastically increases when using updated parameters, including HRR and flow rates, as forecasted by the model. Even though the measurements are not provided after t = 200 seconds in this case, the model can still noticeably perform predictions. Finally, at t = 250 seconds, when more measurements become available, the model further shows improved predictability compared to previous cases. Similar results can be found in other rooms for smoke temperature and smoke layer height prediction.

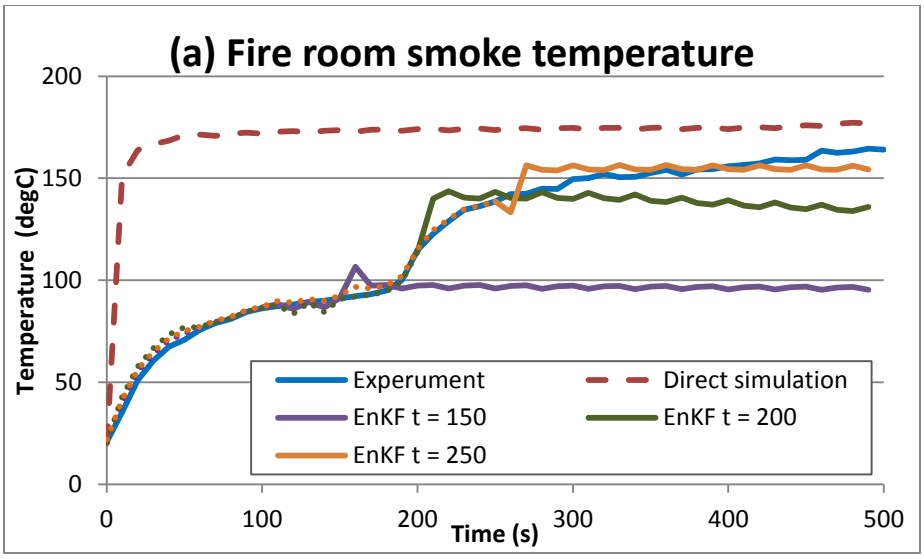
(a) Fire room smoke temperature
Temperature (degC)
Time (s)
Experument
Direct simulation
EnKF t = 150
EnKF t = 200
EnKF t = 250

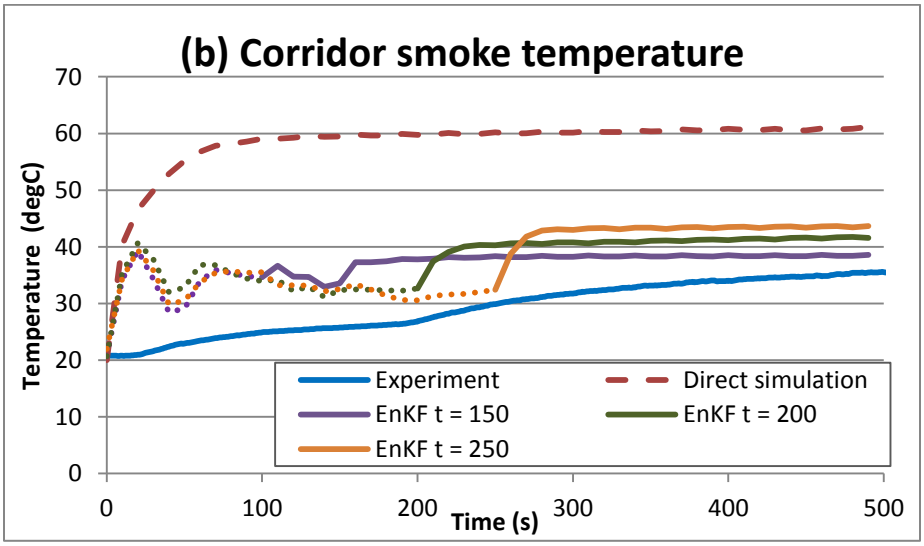
(b) Corridor smoke temperature
Temperature (degC)
Time (s)
Experiment
Direct simulation
EnKF t = 150
EnKF t = 200
EnKF t = 250

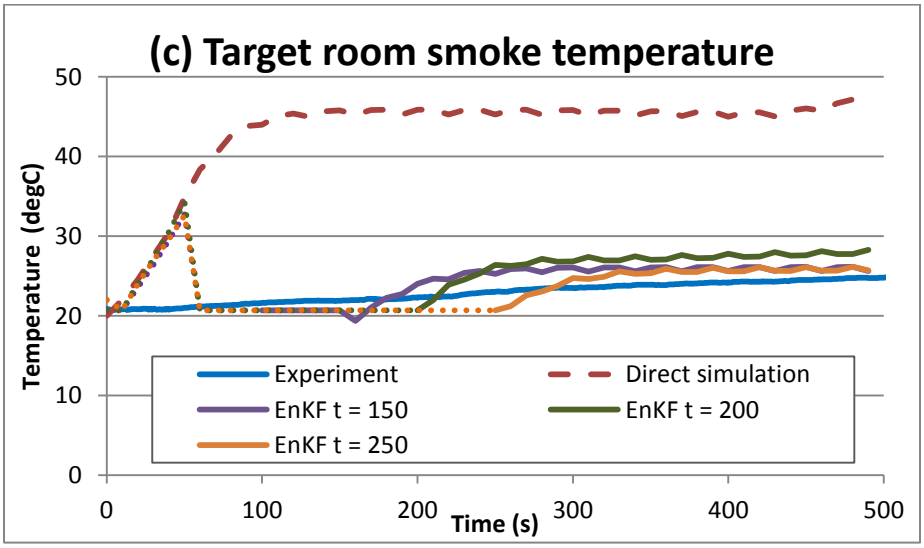
(c) Target room smoke temperature
Temperature (degC)
Time (s)
Experiment
Direct simulation
EnKF t = 150
EnKF t = 200
EnKF t = 250

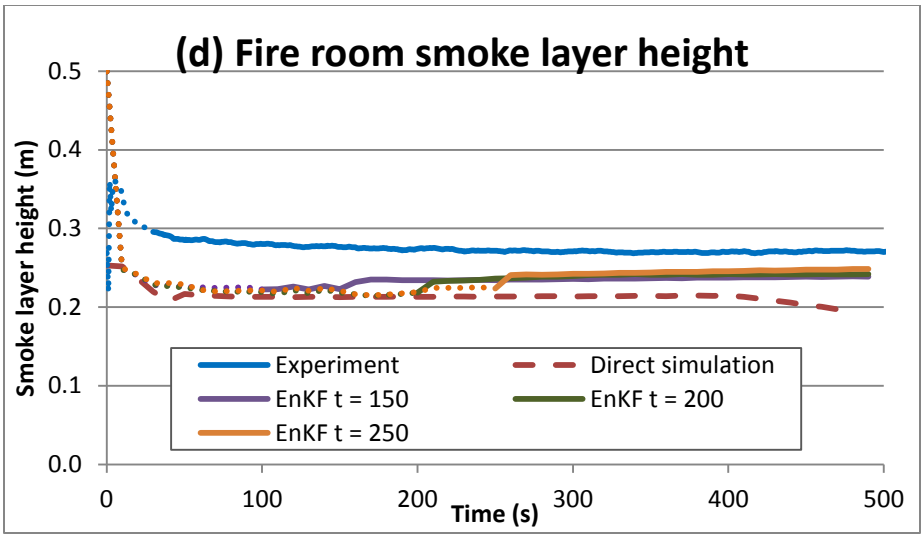

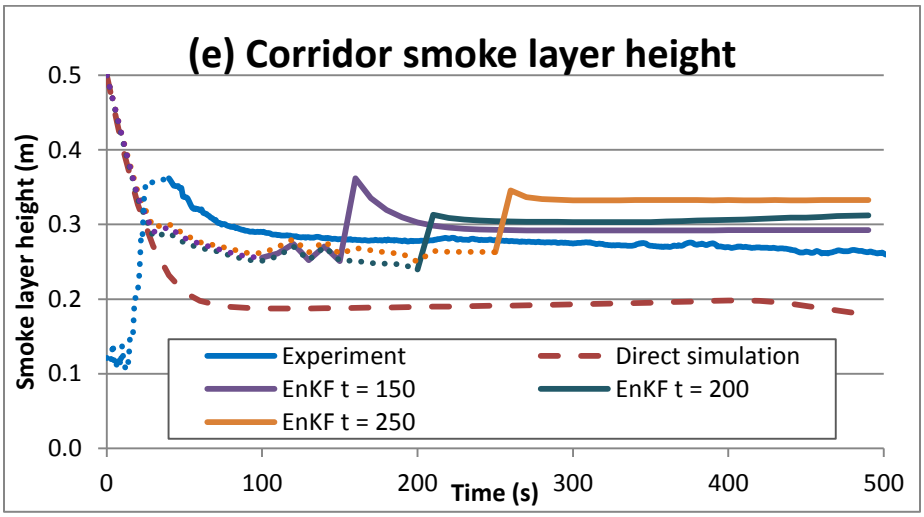

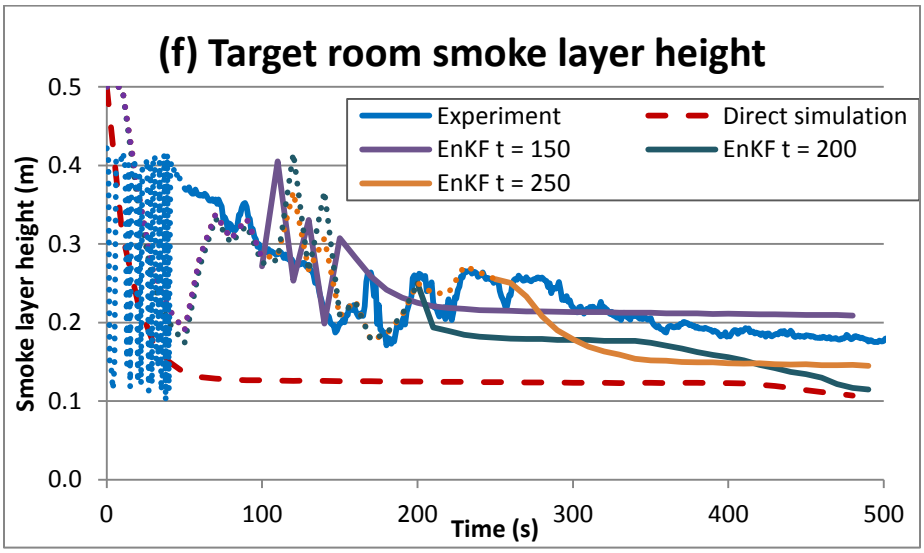

Fig 7.14 (a) to (f) Predictability of the EnKF model during a non-constant fire

References

Hamill, Thomas M., Jeffrey S. Whitaker, and Chris Snyder. "Distance-dependent filtering of background error covariance estimates in an ensemble Kalman filter." *Monthly Weather Review* 129, no. 11 (2001): 2776-2790.

Melling, A. "Tracer particles and seeding for particle image velocimetry."*Measurement Science and Technology* 8, no. 12 (1997): 1406.

Chapter 8 Conclusions and Future Work

8.1 Conclusions

This thesis outlined a general approach to forecasting building indoor environment by using ensemble-based data assimilation algorithms. The results indicate that the proposed method can improve predictability of a simple model by calibrating sensor measurements. Unlike other methods that directly use measurement data as model inputs, the resulting models of this thesis are able to statistically update model parameters to maintain the forecasting accuracy for longer durations.

The models presented in this thesis provide noticeably accurate predictions and require low computational resources compared to other conventional methods. The following is a list of major findings and contributions from this thesis regarding using EnKF for indoor environment forecasting:

▪This thesis research is among the very first studies of using numerical weather prediction models and data assimilation techniques, specifically EnKF, for forecasting simulations of indoor contaminant transport and building fire smoke spread. It is also one of the first times to achieve a real-time forecasting of fire smoke spread in a scaled building model under a controlled laboratory environment.

▪One of the most important parameters affecting the EnKF model's performance is the number of ensemble members. Unfortunately, there is still no theoretical principle for determining an optimal number of ensemble members; it is usually determined by empirical methods such as trial and error.

▪For the EnKF analysis, all sensor measurements are not necessarily provided at the same time

step. When the processing time of the simulation model is significantly shorter than the observation time step, it is suggested that the system be arranged to obtain data in a sequential order from each sensor rather than obtaining all measurements concurrently from all sensors.

▪When the method is applied to existing simulation models, filter divergence can be a potential problem because the perturbation range is sometimes limited by the convergence criteria of the simulation model. This can be mitigated by adding white noise to the simulation results to increase the spread of ensemble members. In addition, modification of the simulation model is sometimes necessary to enable perturbation of certain model parameters.

▪To achieve real-time forecasting, using localization methods to avoid spurious correlation, instead of adding white noise, is suggested. This is because additional ensemble members must compensate for the additional noises.

▪The EnKF is more flexible at applying different localization methods when certain model parameters and model states are not highly correlated.

▪The convergence criteria of an implicit simulation model should be considered with the model parameter perturbation range. When applying an explicit simulation model, the convergence problem can be avoided, which means more freedom in parameter perturbation.

▪The range of parameter perturbation can be reasonably estimated using available measurements. When the measurements are not directly obtainable, it can rely on other simulation tools with higher accuracy (i.e., a CFD model).

▪The determination of measurement uncertainties should account for the assumptions of the simulation model. For example, when a parameter is an average value of a physical condition, the error of using one measurement to represent the mean should also be considered a measurement uncertainty.

▪For noisy observations, such as the measurements obtained from the early stages of a compartment fire, the EnKF analysis results are expected to deviate significantly from the measurements. However, if the spread of ensemble perturbation is also very large, this may cause the analysis results to fit too closely with the measurements, resulting in an imbalanced analysis, which is considered suboptimal (Houtekamer and Mitchell 2005). To avoid this problem, the observation uncertainty should also be increased.

8.2 Future works

8.2.1 Ensemble based DA algorithms for higher dimensional systems

In this thesis, the simulation models are all based on low dimensional systems wherein the number of ensemble members is much greater than that of model nodes. Therefore, the number of ensemble members is usually determined after the whole model structure has been outlined. However, for a higher dimensional system, adding one ensemble member can significantly increase the computational cost. Thus, the order in which the EnKF parameters are determined becomes much more important in higher dimensional systems. For example, increasing the range of parameter perturbation is necessary to avoid filter divergence but demands a higher number of ensemble members, so the determination of optimal model parameters may require the testing of different combinations of multiple parameters instead of optimizing one at each time.

8.2.2 Localization by modifying observation covariance

The localization method presented in this thesis is based on modifying simulation error covariance. Chapter 7 introduces another method involving the modification of observation error covariance. In general, localizing observations are considered more balanced than localizing simulations, but they are also less accurate. The determination of the length scale is also different

(Greybush 2009). The major advantage of localizing observations is it can be applied to the local transform ensemble Kalman filter (LETKF), while simulation localization cannot be implemented. This may enable a comparison between EnKF and LETKF since the same localization method is applied.

8.2.3 Other ensemble based DA algorithms

According to the literature reviews, each ensemble-based DA algorithm has its own advantages, but there are very few ensemble-based DA studies related to building environment. In addition, finding an ensemble-based DA method (and its corresponding model properties) that performs better than other methods at solving a specific type of problem is still very challenging. The study can only be conducted by direct comparisons of detailed models using different methods, where each model is optimized independently, rather than using similar setups.

The following are some general suggestions for the selection of ensemble-based DA algorithms to solve building environment problems:

▪DEnKF–It is more suitable for a system with noisy measurements but that uses a more accurate simulation model. In this case, the magnitude of model state corrections in the analysis cycle can be very small in order to avoid the filter divergence problem.

▪EnSRF–One of the most important characteristics of EnSRF is the non-uniqueness that different ensembles can have the same covariance. This feature can be exploited to evaluate model performance such as the computational and numerical properties of the filter (Tippett et al. 2002).

▪LETKF–For high dimensional systems with a low number of ensemble members, LETKF requires a relatively large effective range for the localized box. This may significantly reduce the efficiency of the system, so it is suggested for use with systems that have more measurements

available.

▪EnKF– The ensemble Kalman filter uses perturbed observation to maintain a reasonable range of ensemble spread in order to avoid filter divergence. The EnKF is relatively more stable compared to other methods but is sometimes considered suboptimal due to the additional observation noises. However, when applied to high dimensional systems, its stability becomes significant due to the lower number of ensemble members required.

8.2.4 Full-scale fire experiment

Although the results presented in Chapter 7 are showing the capability of EnKF in real-time forecasting of compartment fire, the measurements are based on a scaled experiment under well-controlled conditions in a laboratory. The temperature rise in the target room is relatively small which makes it not easy to verify the model predictability. Therefore, a full scale fire experiment is required to further study the effect of changing ventilation conditions as well as widen the range of HRR change.

8.2.5 Reconstruction of a fire scene using available information

Reconstructions of fire scenes are generally performed in insurance and crime investigations. By using information collected from the fire scene, such as a laboratory analysis report of on-site fabric samples, investigators may be able to delineate the entire accident scene.

As several studies suggest (Shen 2008 and Chi 2011), these fire scene investigations can benefit from computer simulations. CFD or zonal computer simulation models can help in the reconstruction of a fire scene by establishing possible scenarios and identifying the most likely case. However, the process can be very time consuming, as CFD simulations may take hours or even days to process the results for one simple model. In such cases, ensemble-based DA algorithms can first statistically outline the scene using simple zone models. Then, after

important parameters such as ignition source and HRR profile are determined, the information can be applied to a CFD model to produce a more detailed fire scene reconstruction.

References

Greybush, Steven, Eugenia Kalnay, Takemasa Miyoshi, K. Ide, and B. Hunt. "EnKF localization techniques and balance." In *WMO 5th International Symposium on Data Assimilation. Melbourne, Australia*, pp. 6-9. 2009.

Shen, Tzu-Sheng, Yu-Hsiang Huang, and Shen-Wen Chien. "Using fire dynamic simulation (FDS) to reconstruct an arson fire scene." *Building and environment*43, no. 6 (2008): 1036-1045.

Chi, Jen-Hao, Sheng-Hung Wu, and Chi-Min Shu. "Using fire dynamics simulator to reconstruct a hydroelectric power plant fire accident." *Journal of forensic sciences* 56, no. 6 (2011): 1639-1644.

Appendix

Appendix Door Flow Rate Model

```
private static double[] doorflowRate(double doorH, double doorA, double roomHa,
double roomHc, double Hda, double Hdc, double Pa, double Pc, double rhoa, double
rhoc){
	double mac = 0.0;
	double mca = 0.0;
	double mbd = 0.0;
	double mdb = 0.0;
	double g = 9.8;
	double rhoair = 1.20416;
	double cvent = 0.6;
	if (Hda>doorH){ //destination smoke layer height is always higher
	//smoke layer height (Hda) is above door soffit
	double dP1 = (Pa-Pc) - (rhoc-rhoa)*g*(roomHa-Hdc) - (rhoair-rhoa)*g*(Hdc-Hda);

	if (dP1 == 0){
		mbd = 0.0;
		mdb = 0.0;
		}else{
		mbd=Math.max(0.0,Math.abs(dP1)/dP1*flowRate(dP1,dP1,doorA,rhoa,cvent));
		mdb=Math.max(0.0, -Math.abs(dP1)/dP1*flowRate(dP1,dP1,doorA,rhoa,cvent));
			}
		}else if (Hdc>doorH){
// if smoke gets in destination room (Hda is below door soffit)
			// case 1, Hdc is above door soffit
	double dP1 = (Pa-Pc) - (rhoc-rhoa)*g*(roomHa-Hdc) - (rhoair-rhoa)*g*(Hdc-
doorH); //deltaP at door soffit
	double dP2 = (Pa-Pc) - (rhoc-rhoa)*g*(roomHc-Hdc) - (rhoair-rhoa)*g*(Hdc-Hda);
//deltaP at smoke layer Hda
	if (dP1>0){ // Normal Case
		if (dP2>0){ //Case B - 1 (No neutral layer)
		double Au = doorA/doorH*(doorH-Hda);
		double Ad = doorA/doorH*Hda;
		mac = flowRate(dP1,dP2,Au,rhoa,cvent);
		mbd = flowRate(dP2,dP2,Ad,rhoair,cvent);
				}else{ //Case C - 1 (Neutral layer exists)
		double Hna = Hdc-((Pa-Pc)-(roomHc-Hdc)*g*(rhoc-rhoa))/(rhoair-rhoa)/g;
		double Au = doorA/doorH*(doorH-Hna);
		double Ad1 = doorA/doorH*(Hna-Hda);
		double Ad2 = doorA/doorH*Hda;
		mac = flowRate(dP1,0,Au,rhoa,cvent);
		double mdb1 = flowRate(0,dP2,Ad1,rhoair,cvent);
		double mdb2 = flowRate(dP2,dP2,Ad2,rhoair,cvent);
		mdb = mdb1+mdb2;
				}
			} else { // Rare Case, dP1<0, back flow
		double Au = doorA/doorH*(doorH-Hda);
		double Ad = doorA/doorH*Hda;
		double mdb1 = flowRate(dP1,dP2,Au,rhoair,cvent);
		double mdb2 = flowRate(dP2,dP2,Ad,rhoair,cvent);
		mdb = mdb1 + mdb2;
			}
```

```
                }else {
            // 2nd case, Hdc is below door soffit
      if (Hda<Hdc){ // Normally
            double dP1 = (Pa-Pc) - (rhoc-rhoa)*g*(roomHa-doorH); //at door soffit
            double dP2 = (Pa-Pc) - (rhoc-rhoa)*g*(roomHa-Hdc); //at Hdc
            double dP3 = (Pa-Pc) - (rhoc-rhoa)*g*(roomHa-Hdc) - (rhoair-
rhoa)*g*(Hdc-Hda);//at Hda
      if (dP1>0){ // Normal Case

      if (dP2>0){
            if (dP3>0){// Case B - 2 (No neutral layer)
            double Au1 = doorA/doorH*(doorH-Hdc);
            double Au2 = doorA/doorH*(Hdc-Hda);
            double Ad = doorA/doorH*Hda;
            double mac1 = flowRate(dP1,dP2,Au1,rhoa,cvent);
            double mac2 = flowRate(dP2,dP3,Au2,rhoa,cvent);
            mac = mac1 + mac2;
            mbd = flowRate(dP3,dP3,Ad,rhoair,cvent);
            } else {//Case C - 2 (Neutral layer is between Hda and Hdc)
            double Hna = Hdc-((Pa-Pc)-(roomHc-Hdc)*g*(rhoc-rhoa))/(rhoair-rhoa)/g;
            double Au1 = doorA/doorH*(doorH-Hdc);
            double Au2 = doorA/doorH*(Hdc-Hna);
            double Ad1 = doorA/doorH*(Hna-Hda);
            double Ad2 = doorA/doorH*Hda;
            double mac1 = flowRate(dP1,dP2,Au1,rhoa,cvent);
            double mac2 = flowRate(dP2,0,Au2,rhoa,cvent);
            double mdb1 = flowRate(0,dP3,Ad1,rhoair,cvent);
            double mdb2 = flowRate(dP3,dP3,Ad2,rhoair,cvent);
                  mac = mac1 + mac2;
                  mdb = mdb1 + mdb2;
                              }
            }else{ // dP2 < 0, Case C - 3 (Neutral layer is between door soffit and
Hdc)
            double Hna = Hdc-((Pa-Pc)-(roomHc-Hdc)*g*(rhoc-rhoa))/(rhoair-rhoa)/g;
            double Au = doorA/doorH*(doorH-Hna);
            double Ad1 = doorA/doorH*(Hna-Hdc);
            double Ad2 = doorA/doorH*(Hdc-Hda);
            double Ad3 = doorA/doorH*Hda;
            mac = flowRate(dP1,0,Au,rhoa,cvent);
            mca = flowRate(0,dP2,Ad1,rhoc,cvent);
            double mdb1 = flowRate(dP2,dP3,Ad2,rhoair,cvent);
            double mdb2 = flowRate(dP3,dP3,Ad3,rhoair,cvent);
            mdb = mdb1 + mdb2;
                        }
                  }else{ // Rare Case, dP1<0, back flow
            double Au1 = doorA/doorH*(doorH-Hdc);
            double Au2 = doorA/doorH*(Hdc-Hda);
            double Ad = doorA/doorH*Hda;
            mca = flowRate(dP1,dP2,Au1,rhoa,cvent);
            double mdb1 = flowRate(dP2,dP3,Au2,rhoa,cvent);
            double mdb2 = flowRate(dP3,dP3,Ad,rhoair,cvent);
            mdb = mdb1 + mdb2;
                  }
                  }else { // For far away room, long simulation
```

```
            double dP1 = (Pa-Pc) - (rhoc-rhoa)*g*(roomHa-doorH); //at door soffit
            double dP2 = (Pa-Pc) - (rhoc-rhoa)*g*(roomHa-Hda); //at Hda
            double dP3 = (Pa-Pc) - (rhoc-rhoa)*g*(roomHa-Hda) - (rhoc-
rhoair)*g*(Hda-Hdc);//at Hdc
      if (dP1>0){ // Normal Case

            if (dP2>0){
            if (dP3>0){// Case B - 2 (No neutral layer)
            double Au = doorA/doorH*(doorH-Hda);
            double Ad1 = doorA/doorH*(Hda-Hdc);
            double Ad2 = doorA/doorH*Hdc;
            double mbd1 = flowRate(dP2,dP3,Ad1,rhoair,cvent);
            double mbd2 = flowRate(dP3,dP3,Ad2,rhoair,cvent);
            mac = flowRate(dP1,dP2,Au,rhoa,cvent);
            mbd = mbd1+mbd2;
                  } else {//Case C - 2 (Neutral layer is between Hda and Hdc)
           double Hna = Hda - (Pa-Pc)/(rhoc-rhoair)/g+(rhoc-rhoa)/(rhoc-rhoair)*Hda;
           double Au1 = doorA/doorH*(doorH-Hda);
            double Au2 = doorA/doorH*(Hda-Hna);
            double Ad1 = doorA/doorH*(Hna-Hdc);
            double Ad2 = doorA/doorH*Hdc;
            double mac1 = flowRate(dP1,dP2,Au1,rhoa,cvent);
            double mac2 = flowRate(dP2,0,Au2,rhoair,cvent);
            double mdb1 = flowRate(0,dP3,Ad1,rhoc,cvent);
            double mdb2 = flowRate(dP3,dP3,Ad2,rhoair,cvent);
            mac = mac1+mac2;
            mdb = mdb1+mdb2;
                  }
            }else{ // dP2 < 0, Case C - 3 (Neutral layer is between door soffit and
Hdc)
            double Hna = roomHa - (Pa - Pc)/g/(rhoc - rhoa);
            double Au = doorA/doorH*(doorH-Hna);
            double Ad1 = doorA/doorH*(Hna-Hda);
            double Ad2 = doorA/doorH*(Hda-Hdc);
            double Ad3 = doorA/doorH*Hdc;
            mac = flowRate(dP1,0,Au,rhoa,cvent);
            double mdb1 = flowRate(0,dP2,Ad1,rhoc,cvent);
            double mdb2 = flowRate(dP2,dP3,Ad2,rhoair,cvent);
            double mdb3 = flowRate(dP3,dP3,Ad3,rhoair,cvent);
            mdb = mdb1 + mdb2 +mdb3;
                  }
            }else{ // Rare Case, dP1<0, back flow
            double Au1 = doorA/doorH*(doorH-Hda);
            double Au2 = doorA/doorH*(Hda-Hdc);
            double Ad = doorA/doorH*Hdc;
            double mca1 = flowRate(dP1,dP2,Au1,rhoc,cvent);
            double mca2 = flowRate(dP2,dP3,Au2,rhoc,cvent);
            mca = mca1 + mca2;
            mdb = flowRate(dP3,dP3,Ad,rhoair,cvent);
                        }
            }
            }
```